UNIVERSITÉ DE LIÈGE
Faculté des Sciences Appliquées

Unsteady aerodynamic modeling methodology based on Dynamic Mode Interpolation (DMI) for transonic flutter calculations

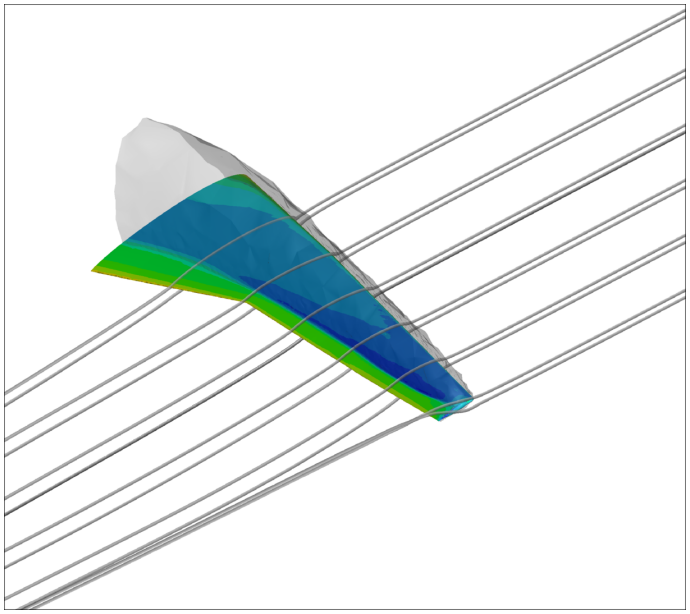

Thèse réalisée en vue de l'obtention du titre
de Docteur en Sciences Appliquées par

Hüseyin GÜNER

Année académique 2019-2020

Résumé

Les avions de transport modernes volent généralement dans le régime d'écoulement transsonique. Ce régime est caractérisé par des phénomènes d'écoulement complexes tels que les ondes de choc en mouvement, les interactions choc-couche limite et les écoulements séparés. Ces non-linéarités aérodynamiques peuvent avoir un impact significatif sur la prédiction de l'instabilité aéroélastique du flottement, qui est d'une grande importance pour la sécurité et les performances des avions.

Cette thèse présente une nouvelle méthodologie de modélisation aérodynamique instationnaire pour prédire le flottement transsonique de configurations 2D et 3D telles que les ailes d'avion. L'idée principale de cette méthodologie est d'obtenir la réponse de l'écoulement aux déformations périodiques de faible amplitude d'une structure sur un intervalle de fréquences par l'interpolation de quelques modes d'écoulement dominants. Ces modes d'écoulement peuvent être obtenus par une décomposition en mode dynamique (*dynamic mode decomposition*) de simulations Euler ou RANS instationnaires à différentes fréquences d'oscillation ou par des simulations d'équilibre harmonique (*harmonic balance*). La méthodologie peut ensuite être utilisée pour obtenir une matrice de force aérodynamique généralisée dans le domaine fréquentiel, et une analyse de stabilité aéroélastique peut être effectuée en utilisant des techniques d'analyse de flottement standard de l'industrie telles que la méthode *p-k*.

La méthodologie est démontrée sur des configurations aéroélastiques transsoniques de référence 2D et 3D. Elle met en évidence que les aspects non-linéaires des écoulements transsoniques sont importants pour l'étude de la stabilité aéroélastique des ailes d'avion. La méthodologie est appliquée avec succès pour calculer le flottement transsonique d'une aile d'avion de ligne réaliste et ses performances sont comparées aux méthodes industrielles standard. La méthodologie est plus précise que les méthodes panneaux principalement utilisées dans l'industrie aérospatiale conduisant à des conceptions d'ailes plus sûres tout en étant plus rapide que les simulations d'interaction fluide-structure de haute fidélité, offrant ainsi une technique prometteuse pour résoudre les problèmes d'aéroélasticité dynamique.

Abstract

Modern transport aircraft generally fly in the transonic flow regime. This regime is characterized by complex flow phenomena such as moving shock waves, shock-boundary layer interactions and separated flows. These aerodynamic nonlinearities can significantly impact the prediction of the flutter aeroelastic instability, which is of great importance for aircraft safety and performance.

This thesis presents a novel unsteady aerodynamic modeling methodology for predicting the transonic flutter of 2D and 3D configurations such as aircraft wings. The main idea of this methodology is to obtain the flow response to small amplitude periodic deformations of a structure over a range of frequencies through the interpolation of few dominant flow modes. These flow modes can be obtained by dynamic mode decomposition (DMD) of unsteady Euler or RANS simulations at different oscillation frequencies or by harmonic balance (HB) simulations. This methodology based on dynamic mode interpolation (DMI) can then be used to obtain a generalized aerodynamic force matrix in the frequency domain, and aeroelastic stability analysis can be performed using industry-standard flutter analysis techniques such as the *p-k* method.

The methodology is demonstrated for 2D and 3D benchmark transonic aeroelastic configurations. It highlights that the nonlinear aspects of transonic flows are important for studying the aeroelastic stability of aircraft wings. The methodology is successfully applied to calculate the transonic flutter of a realistic airliner wing and its performance is compared to standard industrial methods. The methodology is more accurate than the panel methods primarily used in the aerospace industry leading to safer wing designs while being faster than the higher fidelity fluid-structure interaction (FSI) simulations, offering thus a promising technique for solving dynamic aeroelasticity problems.

Acknowledgments

This thesis owes so much to so many people. It is not possible to name them all here one by one, but I wish to thank all those who have encouraged and helped me during the last few years.

I would first like to thank my thesis advisor, Vincent Terrapon, and my co-advisor, Grigorios Dimitriadis, for giving me the opportunity to do a Ph.D. in the fields of aerodynamics and aeroelasticity. I am deeply grateful to them for their trust, assistance and valuable advice. I also want to thank the other members of my jury, Johannes Dillinger, Dorian Jones, Thomas Andrianne, Vincent Denoël and Koen Hillewaert, for the time they spent to read and evaluate this thesis.

I gratefully acknowledge the aerospace company Embraer S.A. for supporting this research. It has been a great pleasure for me to work in collaboration with Pedro Cabral, Alex Prado, Gustavo Silva, Henrique Santos and Hugo Stefanio de Almeida from Embraer's aeroelastic tailoring team. Hugo also contributed to some of the results presented in Chapter 5. I especially want to thank Pedro, who made possible an enriching stay at Embraer in 2018.

I do not forget my colleagues and friends at the University of Liège, Adrien Crovato (with whom I traveled a lot), David Thomas, Amandine Guissart, Sébastien Niessen, Samir Sid, Arnaud Budo and many others who accompanied and supported me. I here wish to express my gratitude to all of them.

To my family, thank you for being there and giving me so much. You have offered me energy and hope through your presence and have enabled me to go forward. I love you, from the bottom of my heart.

Contents

List of Figures

Chapter 1

Introduction

1.1 Context and motivation

The central theme of this thesis is the improvement of unsteady aerodynamic modeling approaches for analyzing the aeroelastic stability of aircraft wings in the transonic flow regime.

Why is it important to perform aeroelastic stability analysis?

As illustrated by Collar's diagram shown in Figure 1.1, dynamic aeroelasticity is the study of the interaction of inertial, elastic and aerodynamic forces acting on flexible structures such as aircraft, wind turbines, turbomachinery blades, racing cars and bridges [1–4]. Although the methodology developed in this work can be applied to many of these applications, the thesis will focus on aircraft wings. The interaction between the forces depicted in Figure 1.1 can cause several dangerous phenomena such as divergence, flutter and limit cycle oscillations (LCOs), which can potentially lead to structural failure.

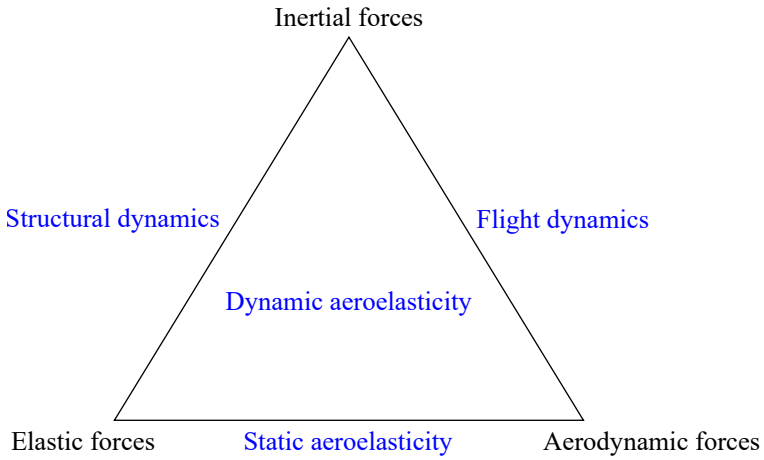

Figure 1.1: The aeroelastic triangle of forces. (Adapted from Bisplinghoff et al. [1].)

Divergence is a static aeroelastic phenomenon that involves the interaction of structural and steady aerodynamic forces and occurs when the aerodynamic loads exceed the structural restoring forces.

Flutter is a self-excited dynamic instability resulting from an unfavorable coupling between inertial, elastic and aerodynamic forces. The flight condition at which this type of instability first occurs is called the flutter point. At the flutter point, a small amplitude perturbation of the structure yields a self-sustained oscillatory response with a small constant amplitude in time as illustrated by the black line in Figure 1.2. The energy dissipated by the structure is equal to the energy extracted from the flow. The amplitude of the oscillations grows exponentially in time beyond the flutter point. The system can also reach finite amplitude oscillations known as limit cycle oscillations in the presence of stabilizing aerodynamic or structural nonlinearities.

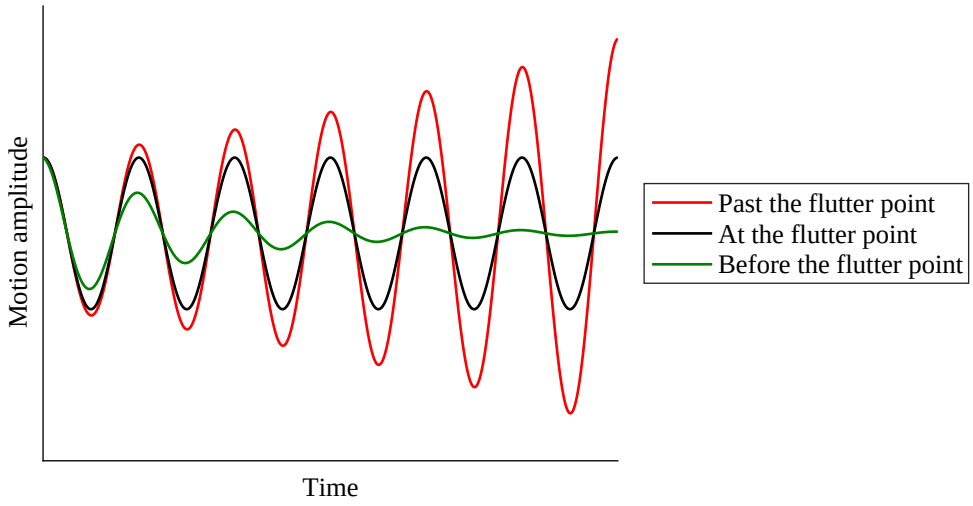

Figure 1.2: Response of an aeroelastic system around a flutter point.

During the design process, it is important to ensure that flutter does not occur within the flight envelope of the aircraft because this aeroelastic instability may result in loss of control and structural damage. In addition, performing an accurate flutter analysis at an early stage in the design of a future aircraft reduces the risk of detecting flutter at the aircraft certification stage, which would require costly modifications of the design.

Moreover, in the ongoing effort to build more efficient aircraft, minimizing structural weight and maximizing aerodynamic efficiency generally lead to the design of flexible and highly-loaded composite wings. Aeroelastic stability analysis thus plays an increasingly important role in preliminary aircraft design. This thesis mainly focuses on the flutter phenomenon in transonic flow.

Why is it important to consider the transonic flow regime?

The transonic flow regime is of great importance for aircraft design. Most modern transport aircraft such as those shown in Figure 1.3 experience transonic flow effects as they generally cruise at free-stream Mach numbers of the order of 0.85 [5]. Moreover, some high-performance military aircraft must also be designed to fly at high subsonic speeds near Mach 1 during specific phases of their mission.

(a) Airbus A330-800 (b) Boeing 777X (c) Embraer E190-E2

Figure 1.3: Three examples of modern civil transport aircraft. (Images from the official Airbus, Boeing and Embraer websites.)

What are the challenges of aerodynamic modeling in transonic flow regime?

The Mach number M, defined as the ratio of the flow velocity to the speed of sound, is a useful parameter to describe different aerodynamic flow regimes as shown in Figure 1.4 [5–8]:

- In the subsonic flow regime illustrated in Figure 1.4a, the Mach number is less than 1 everywhere in the flow. For slender bodies, the free-stream Mach number M_∞ is generally below 0.7 to 0.8. The streamlines are smooth (no discontinuity in slope). Disturbances in the flow propagate both downstream and upstream and are felt everywhere in the flow field.

- The transonic flow regime is characterized by the simultaneous coexistence of both subsonic ($M < 1$) and supersonic ($M > 1$) flow regions near the body, as shown in Figure 1.4b. If the free-stream Mach number is subsonic but close to 1, the flow can become locally supersonic in some regions of the flowfield as it is accelerated around the airfoil. The free-stream Mach number at which a local sonic point ($M = 1$) first appears in the flowfield is called the critical Mach number, which is typically in the range of 0.7 to 0.8 for aircraft wings. The free-stream flow being subsonic, the locally supersonic flow is decelerated below the speed of sound

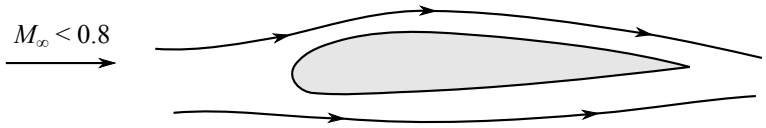

(a) Subsonic flow

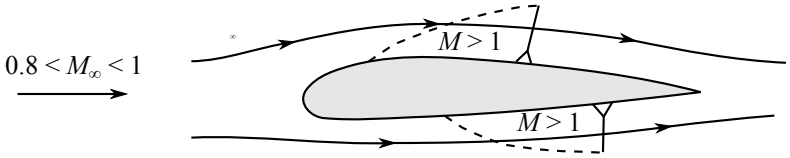

(b) Transonic flow with $M_\infty < 1$

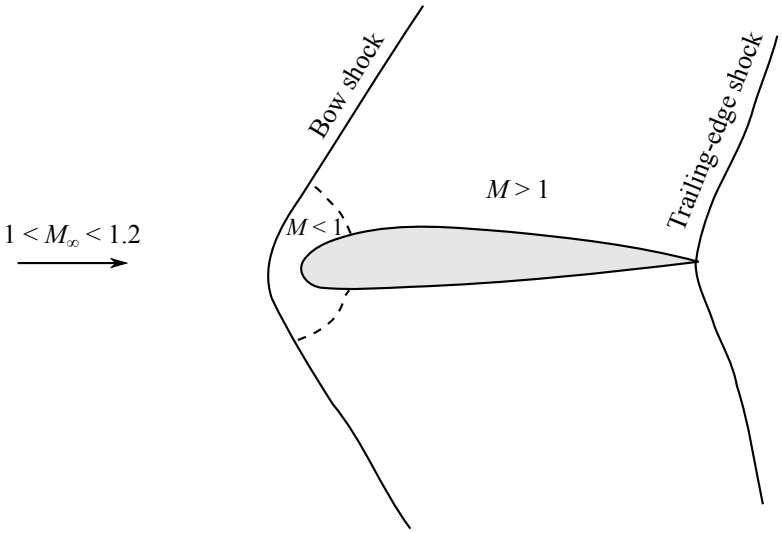

(c) Transonic flow with $M_\infty > 1$

Figure 1.4: Different flow regimes defined by the Mach number. (Adapted from Anderson [5].)

through a shock wave that lies on the body and causes an abrupt change in pressure, temperature and density.

The shock waves lying on the wing surface can perturb the viscous boundary layer as the pressure increases abruptly across a shock wave. This high adverse pressure gradient causes the boundary layer to separate from the wing surface behind the shock wave resulting in high profile drag.

The positions of the shock waves depend on the flow conditions and the geometry of the wing. In addition, the local supersonic flow regions grow or shrink in response to the motion of the wing, which can occur close to a flutter point. In this case, the shock waves move along the surface of the wing and their strength also varies over time as illustrated in Figure 1.5. The supersonic flow regions and therefore the shock waves may even vanish during part of the oscillation cycle. As the free-stream Mach number increases, the supersonic flow regions become larger. The shock waves become stronger and move towards the trailing edge.

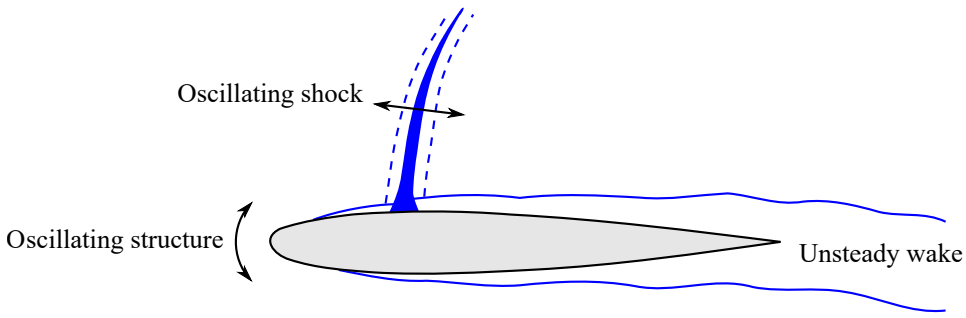

Figure 1.5: Illustration of the moving shock and the flow separation emanating from the shock foot in the case of an oscillating airfoil. (Adapted from Giannelis *et al.* [9]).

- At a free-stream Mach number slightly above unity, a bow shock wave appears ahead of the body as shown in Figure 1.4c. The flow is locally subsonic behind this shock wave. The subsonic flow then expands into a supersonic flow. The flow around the body is mostly supersonic. Two weak shock waves are formed at the trailing edge. The shock-induced boundary layer separation is limited in this case.

These nonlinear phenomena occurring in the transonic flow regime can play an important role in the aeroelastic stability of an aircraft wing [6, 10, 11].

What are the challenges associated with the numerical computation of transonic flutter?

The reliable and efficient calculation of unsteady aerodynamic forces and moments due to structural deformations is one of the main challenges of flutter prediction in the transonic flow regime. Linear panel methods such as the doublet-lattice method (DLM) [12, 13] are predominantly used in aircraft design and allow for a fast and accurate calculation of the flutter boundary of wings in the subsonic flow regime. However, transonic flows are inherently nonlinear and linearized aerodynamic theories cannot model mixed subsonic-supersonic flows including moving shock waves and viscous effects. Corrections of these aerodynamic results for transonic effects based on higher fidelity Computational Fluid Dynamics (CFD) methods [14–16] or wind tunnel measurements are generally used. Nevertheless, the nonlinear dynamics of transonic shocks are not always properly captured [17]. More details on the linear and more advanced aerodynamic models are given in Chapter 2.

Time-accurate fluid-structure interaction (FSI) simulations relying on a higher fidelity CFD model of the flow coupled to a finite element model of the structure can be used to compute the time response of an aeroelastic system to an initial perturbation for a given flight condition. Such simulations make it possible to analyze the aeroelastic stability under transonic conditions, but are computationally expensive for preliminary aircraft design. Moreover, the coupling of commercial CFD and finite element codes is challenging. On the other hand, wind tunnel experiments for flutter calculations in the transonic regime are not used in preliminary aircraft design due to high operational costs.

1.2 Objectives

The overall objective of this research is to develop a novel unsteady aerodynamic modeling methodology that can be applied to aeroelastic stability analysis of aircraft wings subjected to essentially attached flows in the transonic flow regime. The methodology must be more accurate than the approaches currently used in the aerospace industry for preliminary design in transonic conditions and its computational cost must be sufficiently low to allow applications to numerous flight cases.

The range of validity and numerical cost of the methodology are benchmarked against different levels of fidelity using 2D and 3D configurations. In addition, the methodology is applied to the aeroelastic stability analysis of a realistic airliner wing made of composite materials.

1.3 Overview of the thesis

This thesis is organized as follows. Chapter 2 provides an overview of the most useful levels of fidelity used for modeling unsteady transonic flows in aeroelastic applications. This chapter also motivates the choice of the aerodynamic level of fidelity used within the proposed methodology.

Chapter 3 focuses on aerodynamics. It assesses the performance of Euler and RANS simulations in predicting unsteady transonic flows resulting from small amplitude oscillations of a structure. This chapter then presents two approaches to obtain dynamic flow modes, which are useful for describing the dynamics of the flow response. Studying the properties of these dynamic modes results in a new unsteady aerodynamic modeling methodology based on dynamic mode interpolation, which has been presented in several publications by Güner *et al.* [18–20].

Chapter 4 explains how the proposed aerodynamic modeling can be used for aeroelastic stability analysis. The entire methodology is validated using 2D and 3D benchmark transonic aeroelastic configurations. This chapter also investigates the effect of transonic flow nonlinearities (moving shock waves and shock-boundary layer interaction) on the flutter boundary.

In Chapter 5, the developed methodology is applied to an Embraer benchmark wing. This chapter highlights the advantages of the methodology by comparing it to methods currently used in the aerospace industry.

In Chapter 6, the main conclusions of the thesis are summarized and some ideas for future work are presented.

Chapter 2

Review of unsteady transonic aerodynamic models in aeroelasticity

This chapter presents an overview of the most useful unsteady aerodynamic modeling levels of fidelity used for aeroelastic stability calculations in the transonic flow regime. The chapter highlights the challenges of computing unsteady transonic flows, presents all simplifications introduced by the different governing flow equations and explains their advantages and deficiencies. The motivations behind the choice of the aerodynamic level of fidelity used in this thesis to compute unsteady transonic flows are explained. The chapter ends with a discussion of the differences between the proposed methodology and the main existing reduced-order models (ROMs) in the field of aeroelasticity.

2.1 Levels of fidelity

This thesis focuses on the modeling of essentially attached flows where any possible separated flow region would be small in extent and would not have a significant impact on the global flow dynamics and unsteady aerodynamic loads acting on the wing. In practice, the transonic flow around transport aircraft wings is essentially attached close to cruise conditions. This chapter does not present all the existing unsteady aerodynamic modeling methods but only those that are the most useful for aeroelastic applications. An overview of the governing flow equations and the approximations involved are presented in Figure 2.1. The RANS and Euler approaches are introduced first. Chapter 3 will provide more information on these governing flow equations and the associated boundary conditions used in this thesis.

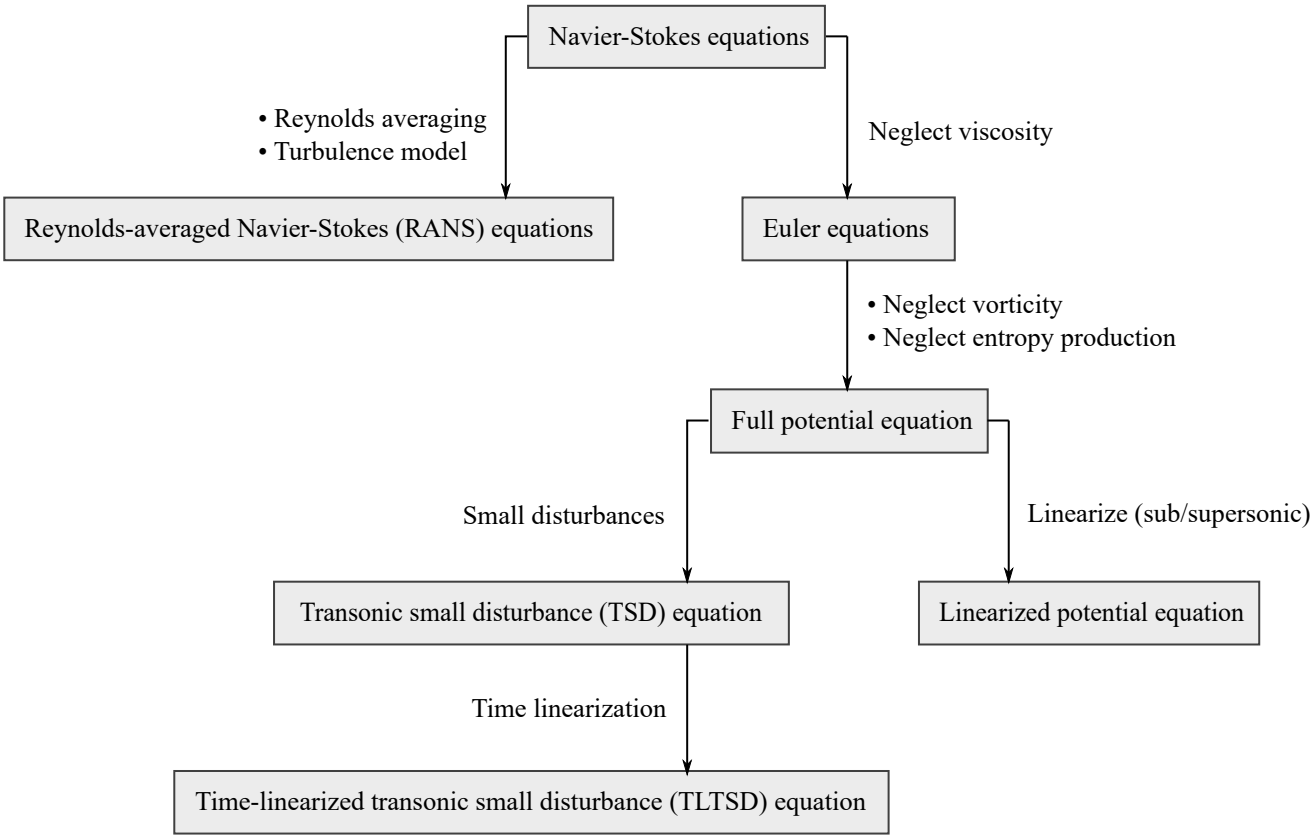

Figure 2.1: Overview of the levels of fidelity used for modeling unsteady transonic flows in aeroelastic applications. (Adapted from Bendiksen [6].)

2.2 Navier-Stokes equations

The most general description of a compressible viscous flow is given by the Navier-Stokes equations, which correspond to the conservation of mass, momentum and energy [14]:

$$\frac{\partial}{\partial t}\begin{bmatrix}\rho\\ \rho\mathbf{u}\\ \rho E\end{bmatrix}+\nabla\cdot\begin{bmatrix}\rho\mathbf{u}\\ \rho\mathbf{u}\otimes\mathbf{u}+p\mathbf{I}-\boldsymbol{\tau}\\ \rho\mathbf{u}E+p\mathbf{u}-\boldsymbol{\tau}\cdot\mathbf{u}-\kappa\nabla T\end{bmatrix}=\mathbf{Q}, \tag{2.1}$$

where $\nabla(\cdot)$ defines the gradient operator, $\nabla\cdot(\cdot)$ is the divergence operator, $\otimes$ is the vector outer product, t is the physical time, ρ is the fluid density, $\mathbf{u}$ is the flow velocity vector, E is the total energy per unit mass, p is the static pressure, $\boldsymbol{\tau}$ is the viscous stress tensor, κ is the thermal conductivity, T is the temperature, and $\mathbf{Q}$ is a generic source term. Current computational resources do not make it possible to directly solve the Navier-Stokes equations for viscous turbulent flows encountered in many industrial CFD applications such as external flows around aircraft or internal flows in turbomachines. Such practical applications have turbulent solutions, which involve small scales and therefore require very fine computational grids.

2.3 RANS equations

A common approximation used to model viscous turbulent flows consists in averaging the Navier-Stokes equations in time to remove the influence of turbulent fluctuations while still capturing unsteady phenomena, which have a larger time scale than that of turbulence. As shown in Figure 2.1, this averaging procedure leads to the Reynolds-averaged (or Favre-averaged) Navier-Stokes (RANS) equations as described in the following.

A Reynolds decomposition of a flow variable A is first defined as

$$A=\bar{A}+A', \tag{2.2}$$

where $\bar{A}$ is the time average of the flow variable A over a time interval T:

$$\bar{A}(\mathbf{x},t)=\frac{1}{T}\int_{t}^{t+T}A(\mathbf{x},\tau)d\tau, \tag{2.3}$$

and A' is the fluctuating part such that $\overline{A'}=0$. For compressible flows, a density-weighted average, also known as the Favre average, is introduced to remove all products of density fluctuations with other fluctuating quantities in the averaging procedure of the Navier-

Stokes equations:

$$\tilde{A} = \frac{\overline{\rho A}}{\bar{\rho}}. \tag{2.4}$$

The flow variable A can then be written as

$$A = \tilde{A} + A'', \tag{2.5}$$

with $\overline{\rho A''} = 0$.

Introducing a Reynolds decomposition of ρ and p, and a Favre average decomposition of $\mathbf{u}$, E and T into the Navier-Stokes equations followed by an averaging of the equations themselves results in the RANS equations [14]. For example, the continuity and momentum equations for the averaged flow quantities are given by

$$\frac{\partial \bar{\rho}}{\partial t} + \nabla \cdot (\bar{\rho}\tilde{\mathbf{u}}) = 0, \tag{2.6}$$

$$\frac{\partial \bar{\rho}\tilde{\mathbf{u}}}{\partial t} + \nabla \cdot (\bar{\rho}\tilde{\mathbf{u}} \otimes \tilde{\mathbf{u}} + \bar{p}\mathbf{I} - \bar{\boldsymbol{\tau}} + \overline{\rho \mathbf{u}'' \otimes \mathbf{u}''}) = 0. \tag{2.7}$$

Because of the Reynolds stress tensor $-\overline{\rho \mathbf{u}'' \otimes \mathbf{u}''}$ appearing in Equation (2.7), the RANS equations are unclosed and must be complemented by a turbulence model, which introduces some approximations in the solutions as discussed in Chapter 3. Note that the energy equation for the averaged flow quantities (not shown here) also has unclosed terms. Chapter 3 presents a more detailed description of these governing equations with the associated boundary conditions and equations of state used in this thesis.

The RANS equations provide a solution for averaged flow quantities in the context of turbulent flows and can capture viscous effects such as the thickening of the boundary layer, shock-boundary layer interaction and moderate flow separation.

2.4 Euler equations

The Euler equations correspond to the continuity, momentum and energy equations for inviscid flows. These equations are obtained by neglecting the viscous stresses and the heat conduction term in the Navier-Stokes equations:

$$\frac{\partial}{\partial t}\begin{bmatrix} \rho \\ \rho \mathbf{u} \\ \rho E \end{bmatrix} + \nabla \cdot \begin{bmatrix} \rho \mathbf{u} \\ \rho \mathbf{u} \otimes \mathbf{u} + p\mathbf{I} \\ \rho \mathbf{u} E + p\mathbf{u} \end{bmatrix} = \mathbf{Q}. \tag{2.8}$$

The advantage of the Euler equations is that the strength, location and dynamics of shock waves are accurately modeled because the entropy production at shocks is properly captured over time. However, this approach does not account for viscous flow effects, especially the interaction of the shock wave with the boundary layer occurring in transonic flows and the resulting flow separation. The Euler equations can be expected to provide reliable flow solutions for many transonic flutter calculations involving smooth flows where viscous effects such as the separation of the boundary layer are not dominant. This type of flow occurs for transonic aircraft wings flying near cruise conditions.

2.5 Potential flow formulations

As shown in Figure 2.1, all potential flow formulations assume irrotational flow in all locations of the flow field:

$$\nabla \times \mathbf{u} = \mathbf{0}, \tag{2.9}$$

where $\nabla \times (\cdot)$ represents the curl operator and $\mathbf{u} = [u, v, w]^\mathsf{T} \in \mathbb{R}^3$ is the velocity vector field in a Cartesian coordinate system. The irrotational flow assumption makes it possible to define a velocity potential function ϕ given by

$$\nabla \phi = \mathbf{u}. \tag{2.10}$$

The partial derivatives of the velocity potential function thus give the velocity components of the flow:

$$\frac{\partial \phi}{\partial x} = \phi_x = u, \tag{2.11}$$

$$\frac{\partial \phi}{\partial y} = \phi_y = v, \tag{2.12}$$

$$\frac{\partial \phi}{\partial z} = \phi_z = w, \tag{2.13}$$

where for example the subscript x indicates a differentiation with respect to the spatial coordinate x.

The velocity potential function can represent both incompressible and compressible flows that are steady or unsteady, but it is restricted to flows without viscous effects due to the irrotational flow assumption. Nevertheless, the boundary layer equations can be solved in conjunction with a potential flow formulation to account for viscous boundary layers in attached flows [21, 22].

2.5.1 Full potential equation

The unsteady full potential equation expressed in differential form is obtained from the mass continuity equation including the definition of the velocity potential function given in Equation (2.10):

$$\frac{\partial \rho}{\partial t} + \nabla \cdot \rho \nabla \phi = 0. \tag{2.14}$$

An expression for the fluid density in terms of the velocity potential and the free-stream flow properties is necessary to represent a closed-form description of the flow field. This relation is derived using the inviscid momentum conservation assuming an irrotational and isentropic flow of a perfect gas, the definition of the speed of sound and the standard density-pressure relation for an isentropic flow:

$$\rho = \rho_\infty \left[1 + \frac{\gamma - 1}{2a_\infty^2} \left(U_\infty^2 - 2\phi_t - \phi_x^2 - \phi_y^2 - \phi_z^2 \right) \right]^{\frac{1}{\gamma - 1}}, \tag{2.15}$$

where ρ_∞ is the free-stream fluid density, a_∞ is the free-stream speed of sound, γ is the ratio of specific heats and the subscript t indicates a differentiation with respect to the physical time.

For the simulation of external flows over an aircraft wing, boundary conditions are required for the free stream, the symmetry plane where the wing root is attached and the aerodynamic surface in order to complete the full potential equation formulation. The free-stream boundary condition consists in imposing a free-stream velocity potential distribution, which is usually a uniform flow. A flow tangency condition is imposed on the symmetry plane and on the moving fluid-structure boundary for inviscid flows.

For aerodynamic applications, the full potential equation computes an irrotational velocity vector field that is not able to predict the aerodynamic lift as stated by the Kutta-Joukowski theorem [5]. A Kutta condition which forces the pressure on the upper and lower surfaces to match at the wing's trailing edge can be imposed to solve this problem. The Kutta condition means that the flow must leave a sharp trailing edge smoothly without discontinuities in the flow pressure or velocity as illustrated in Figure 2.2.

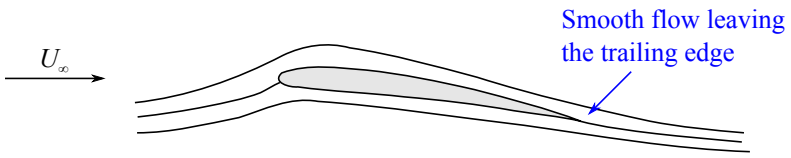

Figure 2.2: Kutta condition at the trailing edge. (Adapted from Bendiksen [6].)

The full potential equation given in Equation (2.14) is written in conservative form as all variables are inside the outer differentiation. The unsteady nonconservative full potential equation can be obtained from the conservative form by expanding the derivatives using the chain rule and by computing the density derivatives using the density expression given in Equation (2.15), the definition of the speed of sound and the standard density-pressure relation for an isentropic flow:

$$(a^2-u^2)\phi_{xx}+(a^2-v^2)\phi_{yy}+(a^2-w^2)\phi_{zz}-2uv\phi_{xy}-2uw\phi_{xz}-2vw\phi_{yz} \\ =\phi_{tt}+2u\phi_{xt}+2v\phi_{yt}+2w\phi_{zt}. \quad (2.16)$$

The full potential equation is a nonlinear partial differential equation without analytical solutions. All numerical methods for solving this equation require volume discretization.

The nonlinear full potential equation allows flow modeling about arbitrary shapes provided that viscous effects such as flow separation are not important. This approach is thus adequate to analyze the effects of airfoil thickness and camber on the aerodynamic loads at a lower computational cost than the higher fidelity Euler equations. However, the full potential flow model neglects entropy production at the shock waves. Therefore, the properties of the predicted shock waves are not always accurate. The full potential equation generally provides satisfactory results for transonic flows with weak shock waves since the entropy produced by these shocks is small. This condition means that the maximum shock Mach number does not exceed approximately 1.3. However, the local Mach number can reach values of the order of 1.5 and higher in most transonic flutter applications related to aircraft wings and control surfaces. In this case, the shock waves predicted by the full potential approach are typically too strong and too close to the trailing edge. These errors in the shock strength and position can significantly influence the flutter instability predictions [6].

2.5.2 Transonic small disturbance equation

The transonic small disturbance (TSD) equation is a simplification of the full potential equation for transonic flows under the assumption of small perturbations. Considering that the body is causing only small perturbations in the flow, small-disturbance velocities $\mathbf{u}'$ can be defined such that

$$\mathbf{u} = \mathbf{u}_\infty + \mathbf{u}', \tag{2.17}$$

where $\mathbf{u}$ is the local velocity vector, $\mathbf{u}_\infty$ is the free-stream velocity vector and $|\mathbf{u}'| \ll |\mathbf{u}_\infty|$. A small-disturbance velocity potential φ can also be defined as

$$\phi = \phi_\infty + \varphi, \tag{2.18}$$

$$\nabla\varphi = \mathbf{u}', \tag{2.19}$$

where ϕ_∞ is the constant potential due to the free stream. Assuming that the free-stream flow is aligned with the x-axis, the small-disturbance velocity components are given by

$$\varphi_x = u - u_\infty = u', \tag{2.20}$$

$$\varphi_y = v', \tag{2.21}$$

$$\varphi_z = w'. \tag{2.22}$$

The transonic small-disturbance (TSD) potential equation is derived by substituting the small-disturbance velocity components into the full potential equation given in Equation (2.16) and neglecting the small terms:

$$\left[1 - M_\infty^2 - M_\infty^2(\gamma+1)\frac{\varphi_x}{u_\infty}\right]\varphi_{xx} + \varphi_{yy} + \varphi_{zz} = \frac{1}{a_\infty^2}\left(\varphi_{tt} + 2u_\infty\varphi_{xt}\right), \tag{2.23}$$

where M_∞ is the free-stream Mach number. Note that the first term cannot be considered small because $1 - M_\infty^2 \approx M_\infty^2(\gamma+1)\varphi_x/u_\infty$ for transonic flows near $M_\infty = 1$. The TSD potential equation is nonlinear because of the $\varphi_x\varphi_{xx}$ term, which is required to capture shock waves. It must thus be solved numerically through space and time discretizations. Moreover, the computational grid surrounding the body must be sufficiently fine to capture the shock waves.

All small-disturbance velocity components are set to zero for the free-stream boundary condition. In small-disturbance theory, the flow tangency boundary condition for a thin airfoil or wing is imposed at a mean surface instead of the actual solid surface, neglecting

thereby the thickness:

$$\phi_z = \frac{\partial g}{\partial t} + u_\infty \frac{\partial g}{\partial x} \quad \text{on } z = 0, 0 \leq x \leq c, \tag{2.24}$$

where x is aligned with the free-stream flow, y is in the spanwise direction, z is in the vertical direction and g defines the shape of the wing without thickness, which is calculated from the camber and the instantaneous local angle of attack. This boundary condition facilitates the generation of volume grids as the grids do not have to fit the 3D geometry of the wing. The drawback of the small-disturbance flow-tangency boundary condition appears at the leading edge of the airfoil where the slope of the surface becomes infinite and the boundary condition cannot be accurately implemented. As a result, the solution at the leading edge stagnation point is not properly computed.

The TSD potential equation is valid for subsonic, transonic and supersonic flows that are assumed inviscid, isentropic, irrotational under the assumption of small disturbances with respect to the free stream. The small-disturbance assumption limits the range of application to thin airfoils or wings subjected to small elastic deformations at small angles of attack. The TSD equation also suffers from the disadvantages of the full potential equation mentioned in the previous section.

2.5.3 Time-linearized transonic small disturbance equation

All the time derivative terms in the TSD equation (2.23) are linear and a time linearization can be assumed. The perturbation potential φ is then represented as a superposition of a steady perturbation potential $\bar{\varphi}(x,y,z)$ and an unsteady perturbation potential $\varphi'(x,y,z,t)$ due to small amplitude motion:

$$\varphi = \bar{\varphi}(x,y,z) + \varphi'(x,y,z,t). \tag{2.25}$$

Substituting this expression into Equation (2.23), neglecting the small terms by assuming that the magnitude of the unsteady perturbation potential is much smaller than that of the steady perturbation potential and separating the steady and unsteady terms, one obtains

$$\left[1 - M_\infty^2 - M_\infty^2(\gamma+1)\frac{\bar{\varphi}_x}{u_\infty}\right]\bar{\varphi}_{xx} + \bar{\varphi}_{yy} + \bar{\varphi}_{zz} = 0, \tag{2.26}$$

$$(1-M_\infty^2)\varphi'_{xx} + \varphi'_{yy} + \varphi'_{zz} - \frac{1}{a_\infty^2}\left(\varphi'_{tt} - 2u_\infty\varphi'_{xt}\right) = (\gamma+1)\frac{M_\infty^2}{u_\infty}\frac{\partial}{\partial x}(\bar{\varphi}_x\varphi'_x). \tag{2.27}$$

Equation (2.26) is the steady TSD equation. It is nonlinear and can be solved numerically using a discrete spatial grid. Equation (2.27) corresponds to the time-linearized transonic small disturbance (TLTSD) equation [23–25]. It models the unsteady flow due to small de-

formations as a linear unsteady small perturbation around a nonlinear steady background flow. The steady background flow in the TLTSD equation can be obtained using a higher fidelity steady Euler or RANS model instead of solving the steady TSD equation given in Equation (2.26), so as to include steady shock waves and possibly viscous boundary layers.

The ZAERO software package [23, 26] features a field-panel method to solve the TLTSD equation. It treats the right-hand-side term of Equation (2.27) as a volume source term σ_v given by

$$\sigma_v = (\gamma+1)\frac{M_\infty^2}{u_\infty}\bar{\varphi}_x\varphi'_x, \tag{2.28}$$

$$\frac{\partial\sigma_v}{\partial x} = (\gamma+1)\frac{M_\infty^2}{u_\infty}\frac{\partial}{\partial x}(\bar{\varphi}_x\varphi'_x). \tag{2.29}$$

The source term σ_v is evaluated using finite differences on a volume around the lifting surface. This volume must include the entire supersonic region but does not have to extend far from the wing. The rest of the equation is solved by applying a singularity distribution on the lifting surface, in the same way as a three-dimensional panel method.

The TLTSD approach has a lower computational cost compared to the unsteady Euler and RANS approaches. The shortcoming of this method is that it precludes large unsteady disturbances. An accurate prediction of the nonlinear shock dynamics over a range of frequencies is not ensured since the steady background flow contains only information on the steady shocks and the unsteadiness of the flow is calculated by a linear panel method. In addition, the boundary layer cannot feature significant unsteadiness.

2.5.4 Linearized potential equation

The unsteady linear potential equation is obtained by neglecting the nonlinear term of the TSD equation given in Equation (2.23) or the source term in Equation (2.27):

$$(1-M_\infty^2)\varphi_{xx}+\varphi_{yy}+\varphi_{zz} = \frac{1}{a_\infty^2}(\varphi_{tt}+2u_\infty\varphi_{xt}). \tag{2.30}$$

The current industry practice to solve this linearized potential equation is to use numerical unsteady panel methods such as the doublet lattice method (DLM) [12, 27]. The lifting surface is divided into panels and the lift distribution is computed using potential flow elements such as doublets or vortices acting over each panel. Such approaches calculate aerodynamic influence coefficients (AIC) that describe the aerodynamic effect that each panel has on the others.

Equation (2.30) is linear and further limits the flow physics that can be represented. Numerical methods based on the linear potential equation are limited to purely subsonic

or supersonic flows because the linearization of the full potential equation removes the essential mathematical term necessary to predict the occurrence of shock waves appearing in the transonic flow regime. Based on the theory of partial differential equations [14], nonlinear governing flow equations are necessary to describe the physics of transonic flows since the type of nonlinear equations can change from elliptic in the subsonic flow regions to hyperbolic in the supersonic flow regions. Nonlinear equations are required to properly capture the spatial extent and time variation of the subsonic and supersonic flow regions and therefore the moving shock waves.

The three-dimensional panel methods for solving the linearized potential equation are computationally efficient but do not capture the shock waves and are therefore not adequate for transonic flows. Several techniques exist to correct the unsteady linear aerodynamic models using experimental measurements or nonlinear CFD data in order to take into account some aerodynamic nonlinearities and better calculate the aerodynamic loads for transonic flutter calculations.

Palacios et al. [28] and Silva [29] provide a complete overview of such correction techniques that can be applied to aeroelastic stability analysis of aircraft wings. These techniques are classified into four major groups: force-matching methods [30–32], pressure-matching methods [33–35], semi-empirical methods [36–38] and methods for correcting the aerodynamic influence coefficient matrix [39–41]. These combined procedures are less expensive than the direct use of higher-fidelity CFD methods to solve transonic aeroelastic problems. However, the existing transonic correction methods can only provide approximate pressure and force corrections because most of these corrections rely on steady-state reference data. The modified unsteady pressure distributions often fail to capture the proper unsteady transonic effects and provide inconsistent aeroelastic stability boundaries [17].

2.5.5 Limitations of the potential flow approaches

In the aerospace industry, three-dimensional unsteady panel methods, such as the doublet lattice method (DLM), are the primary aerodynamic tool for aeroelastic stability analysis of aircraft wings during the preliminary design. However, these approaches are based on the linearized potential equation and are therefore limited to the analysis of inviscid and irrotational flows over thin airfoils at small angles of attack in the subsonic flow regime (i.e., the free-stream Mach number is not close to 1, typically below 0.7). Chapter 5 evaluates the performance of the linearized potential equation in modeling unsteady transonic flows.

Other numerical methods for the preliminary design are based on the TSD and TLTSD models. However, these approaches are restricted to small perturbations and therefore to thin airfoils at small angles of attack. These assumptions introduce important limitations

for the description of unsteady transonic flows in the context of aircraft aerodynamics and aeroelastic stability problems (e.g., flutter and divergence). Chapter 5 illustrates the impact of these hypotheses on the unsteady pressure distributions and the aeroelastic behavior of a 3D wing flying in the transonic flow regime.

The full potential equation allows modeling the flow around airfoils of any shape at any angle of attack. Nevertheless, this level of fidelity is not used in this thesis because it assumes that the flow is isentropic and, therefore, the predicted shock waves are not always accurate.

2.6 Linear frequency domain method

Finally, it is worth mentioning another approach that can be used to approximate the flow response to a small periodic motion of the structure. If the oscillations of the structure have a small amplitude, the linear frequency domain (LFD) method can also be used to approximate the flow response at a reduced computational cost compared to time-accurate simulations. The LFD method calculates a harmonic solution of the linearized flow problem [75–77]. Although the LFD method is not directly used in this thesis, this method is described below for the sake of completeness.

The semi-discretized form of the governing flow equations (e.g., Euler or RANS) obtained after spatial discretization can be written concisely as

$$\frac{d\mathbf{U}}{dt} + \mathbf{R}(\mathbf{U}, \mathbf{x}, \dot{\mathbf{x}}) = 0, \tag{2.31}$$

where $\mathbf{R}$ is the residual term resulting from the spatial discretization, $\mathbf{U}$ represents the conservative variables, $\mathbf{x}$ and $\dot{\mathbf{x}}$ correspond respectively to the mesh point positions and velocities, which are known in the case of a forced motion of the structure. If this motion has a small amplitude, the unsteady terms $\mathbf{U}$ and $\mathbf{x}$ can be written as a superposition of a steady mean state and a small time-varying perturbation:

$$\mathbf{U}(t) = \bar{\mathbf{U}} + \tilde{\mathbf{U}}(t), \qquad |\tilde{\mathbf{U}}| \ll |\bar{\mathbf{U}}|, \tag{2.32}$$

$$\mathbf{x}(t) = \bar{\mathbf{x}} + \tilde{\mathbf{x}}(t), \qquad |\tilde{\mathbf{x}}| \ll |\bar{\mathbf{x}}|. \tag{2.33}$$

where $\bar{\mathbf{U}}$ satisfies the steady problem without structural motion. Substituting Equations (2.32) and (2.33) into Equation (2.31) and linearizing about the steady mean state give the following equation for the perturbations:

$$\frac{d\tilde{\mathbf{U}}}{dt} + \left.\frac{\partial \mathbf{R}}{\partial \mathbf{U}}\right|_{\bar{\mathbf{U}},\bar{\mathbf{x}}} \tilde{\mathbf{U}} + \left.\frac{\partial \mathbf{R}}{\partial \mathbf{x}}\right|_{\bar{\mathbf{U}},\bar{\mathbf{x}}} \tilde{\mathbf{x}} + \left.\frac{\partial \mathbf{R}}{\partial \dot{\mathbf{x}}}\right|_{\bar{\mathbf{U}},\bar{\mathbf{x}}} \dot{\tilde{\mathbf{x}}} = 0. \tag{2.34}$$

Assuming a periodic structural motion and a resulting harmonic flow response, the perturbation terms $\tilde{\mathbf{U}}$ and $\tilde{\mathbf{x}}$ can be expressed as follows:

$$\mathbf{U}(t) = \bar{\mathbf{U}} + \tilde{\mathbf{U}}(t) = \bar{\mathbf{U}} + \Re(\hat{\mathbf{U}}\mathrm{e}^{i\omega t}), \tag{2.35}$$

$$\mathbf{x}(t) = \bar{\mathbf{x}} + \tilde{\mathbf{x}}(t) = \bar{\mathbf{x}} + \Re(\hat{\mathbf{x}}\mathrm{e}^{i\omega t}), \tag{2.36}$$

where the amplitudes $\hat{\mathbf{U}}$ and $\hat{\mathbf{x}}$ are complex. Substituting Equations (2.35) and (2.36) into Equation (2.34) results in

$$i\omega\hat{\mathbf{U}} + \left.\frac{\partial \mathbf{R}}{\partial \mathbf{U}}\right|_{\bar{\mathbf{U}},\bar{\mathbf{x}}} \hat{\mathbf{U}} = -\left.\frac{\partial \mathbf{R}}{\partial \mathbf{x}}\right|_{\bar{\mathbf{U}},\bar{\mathbf{x}}} \hat{\mathbf{x}} - i\omega \left.\frac{\partial \mathbf{R}}{\partial \dot{\mathbf{x}}}\right|_{\bar{\mathbf{U}},\bar{\mathbf{x}}} \hat{\mathbf{x}}. \tag{2.37}$$

This equation can be expressed as a linear system of equations:

$$\mathbf{A}\mathbf{x} = \mathbf{b}, \tag{2.38}$$

$$\begin{bmatrix} \left.\frac{\partial \mathbf{R}}{\partial \mathbf{U}}\right|_{\bar{\mathbf{U}},\bar{\mathbf{x}}} & -\omega\mathbf{I} \\ \omega\mathbf{I} & \left.\frac{\partial \mathbf{R}}{\partial \mathbf{U}}\right|_{\bar{\mathbf{U}},\bar{\mathbf{x}}} \end{bmatrix} \begin{bmatrix} \Re(\hat{\mathbf{U}}) \\ \Im(\hat{\mathbf{U}}) \end{bmatrix} = \begin{bmatrix} -\left.\frac{\partial \mathbf{R}}{\partial \mathbf{x}}\right|_{\bar{\mathbf{U}},\bar{\mathbf{x}}} \Re(\hat{\mathbf{x}}) + \omega \left.\frac{\partial \mathbf{R}}{\partial \dot{\mathbf{x}}}\right|_{\bar{\mathbf{U}},\bar{\mathbf{x}}} \Im(\hat{\mathbf{x}}) \\ -\left.\frac{\partial \mathbf{R}}{\partial \mathbf{x}}\right|_{\bar{\mathbf{U}},\bar{\mathbf{x}}} \Im(\hat{\mathbf{x}}) - \omega \left.\frac{\partial \mathbf{R}}{\partial \dot{\mathbf{x}}}\right|_{\bar{\mathbf{U}},\bar{\mathbf{x}}} \Re(\hat{\mathbf{x}}) \end{bmatrix}. \tag{2.39}$$

For example, the DLR TAU code use the following steps for the linear frequency domain method:

- The mean flow solution $\bar{\mathbf{U}}$ is obtained by a steady-state simulation at the mean position of the structure $\bar{\mathbf{x}}$.
- The terms $\left.\frac{\partial \mathbf{R}}{\partial \mathbf{x}}\right|_{\bar{\mathbf{U}},\bar{\mathbf{x}}}$ and $\left.\frac{\partial \mathbf{R}}{\partial \dot{\mathbf{x}}}\right|_{\bar{\mathbf{U}},\bar{\mathbf{x}}}$ appearing in the linear system of equations (2.39) are computed using central finite differences knowing the mean solutions $\bar{\mathbf{U}}$ and $\bar{\mathbf{x}}$ and the prescribed periodic deformation of the grid.
- The Jacobian $\left.\frac{\partial \mathbf{R}}{\partial \mathbf{U}}\right|_{\bar{\mathbf{U}},\bar{\mathbf{x}}}$ is obtained by a discrete adjoint method available in the TAU solver [78].
- The linear system of equations (2.39) is solved to obtain the term $\hat{\mathbf{U}}$. The LFD method is therefore more accurate than the TLTSD approximation, which calculates the unsteadiness of the flow by a lower fidelity linear panel method.

The LFD method is a good candidate for flutter calculation because the first three steps above are time consuming, but then the last step can be repeated for many different frequencies. This makes the method very efficient. However, some inaccuracies can be expected, especially in highly nonlinear transonic flows, because the steady solution differs from the time-averaged unsteady solution. This is illustrated for instance in Chapter 5 for a 3D wing.

2.7 Discussion

The Euler and RANS equations allow a more accurate calculation of the unsteady transonic flow around airfoils and wings compared to the potential flow models. Time-accurate Euler or RANS-based fluid-structure interaction (FSI) simulations can be used to compute the time response of a system to an initial perturbation for a given flight condition. However, the cost of such FSI simulations is much higher than potential flow-based approaches, which precludes their use for common aeroelastic calculations in the early design phase. In addition, the coupling of commercial CFD and finite element codes is challenging. The motivation for this work is therefore to develop a new methodology based on the higher-fidelity aerodynamic models such as Euler or RANS while limiting the computational cost. An important objective of this thesis is to compare the accuracy and computational cost of this new methodology with lower fidelity potential flow methods (see Chapter 5).

Another approach to reach higher fidelity at limited cost is to rely on reduced-order models (ROMs). Several ROMs of unsteady aerodynamic flows have been proposed (e.g., [42–46]). The main idea is to compute the eigenvalues and eigenmodes of a time or frequency-domain CFD model of unsteady flow. These eigenmodes are then used as basis vectors to construct a ROM with significantly fewer degrees of freedom than the original system, which considerably reduces the computational cost. The details of the formulation vary depending on the level of fidelity of the aerodynamic model, the technique used to determine the eigenvalues and eigenmodes and the construction of the ROM. Among these variants, the popular ROMs using basis vectors determined from proper orthogonal decomposition (POD) [47] of unsteady flow solutions for prescribed wing motion at different frequencies can accurately compute the unsteady flow over a range of frequencies. These ROMs can predict the aeroelastic behavior of transonic airfoils [48], wings [49–51] and aircraft models [45, 52, 53] with decent accuracy.

This thesis presents a conceptually novel unsteady aerodynamic modeling methodology, which has useful advantages over existing ROMs. In contrast to most ROMs, the methodology does not require the construction of a reduced-order approximation of the discretized governing equations. Additionally, the methodology does not assume anything about the origin of the input flow data, so that it can be used with any aerodynamic level of fidelity and any existing CFD code or even with experimental measurements. Furthermore, the methodology can be used directly with standard flutter analysis techniques such as the widely used *p-k* method [3, 54] to both find the flutter characteristics of a system and describe its subcritical behavior.

Chapter 3

Unsteady aerodynamic modeling based on dynamic mode interpolation

In a typical flutter analysis, a flight Mach number (and possibly a Reynolds number) is imposed and the velocity at which flutter appears is sought. Although feasible, the use of time-domain CFD-based fluid-structure interaction (FSI) simulations for flutter calculation is costly because the system response must be computed at many different free-stream velocities. A more efficient approach to obtain the flutter solution at a design flight Mach number consists in solving the equations of motion expressed in the frequency domain (e.g., *p-k* method, as detailed in the next chapter). However, this approach requires to express the aerodynamic loads associated with small periodic deformation of the structure as a function of the oscillation frequency.

Determining this dependency of the aerodynamic loads on the frequency is the motivation for the development of the new unsteady aerodynamic modeling approach based on dynamic mode interpolation (DMI). The main idea of the DMI methodology is to obtain the flow response to small amplitude periodic deformations of a structure over a range of frequencies through the interpolation of the most dominant flow dynamic modes extracted from a few unsteady simulations at reference frequencies. These simulations are carried out here by solving the Euler or RANS equations, but other approaches could also be used (e.g., the full potential equation).

This chapter presents an overview of the DMI methodology. The numerical methods that are employed in the methodology are then explained. First, the governing flow equations used in this thesis are described. Then, two equivalent approaches to obtain the flow dynamic modes of a periodic flow response are presented: the dynamic mode decomposition (DMD) of the unsteady flow and the harmonic balance (HB) method. The properties of these dynamic modes are studied using the transonic flow around a two-dimensional pitching airfoil.

3.1 Theoretical background

3.1.1 Overview of the DMI methodology

The goal of the methodology is to provide the flow response to small amplitude periodic motion of a structure as a function of the oscillation frequency for given flow conditions (free-stream Mach number M_∞ and Reynolds number Re).

- The first step consists in computing the flow around the oscillating structure at selected frequencies relying on a few high-fidelity unsteady CFD simulations, such as Euler or RANS simulations. This chapter assesses the accuracy of the Euler and RANS approaches for modeling such flows.

- The unsteady flow fields at the selected frequencies can then be processed using dynamic mode decomposition (DMD) to extract the most dominant dynamic modes of the flow response. As discussed below, these dynamic modes can also be directly obtained from harmonic balance (HB) simulations instead of applying DMD to unsteady simulations. The question is then to determine how many dynamic modes are required to capture the flow dynamics with sufficient accuracy, and what frequency should be imposed for the reference simulations. This chapter studies the relative contribution of the flow modes at a fixed forcing frequency to the flow dynamics. The influence of the forcing frequency on the flow mode shapes is analyzed.

- The third step consists in interpolating these dominant dynamic modes for any other frequency in order to estimate the flow response for a range of frequencies. The resulting frequency-domain aerodynamic forces can then be used for aeroelastic stability analysis. Each step of the methodology is described in more detail in the following sections.

Aerodynamic forces acting on a body can be predicted using a set of coupled nonlinear partial differential equations (PDEs) that govern the fluid dynamics around the body. In this work, a collection of open-source software tools written in C++ and Python, called SU2, is used for the analysis of PDEs on unstructured or structured meshes using state-of-the-art numerical methods [55–58]. The following section is dedicated to the description of the governing flow equations used within the DMI methodology and the corresponding boundary conditions. Only the RANS and Euler models are considered in this work. A brief overview of the numerical implementations is also presented.

3.1.2 Compressible unsteady Reynolds-averaged Navier-Stokes equations

The flow problem of interest is the external flow over an aerodynamic body such as a wing or a full aircraft configuration in arbitrary motion. Figure 3.1 represents an aerodynamic body of external surface S in a conforming flow domain $\Omega \subset \mathbb{R}^3$ delimited by a far-field boundary Γ_∞. The position of S, and thus Ω, can evolve over time, allowing the study of aerodynamic bodies moving in a fluid.

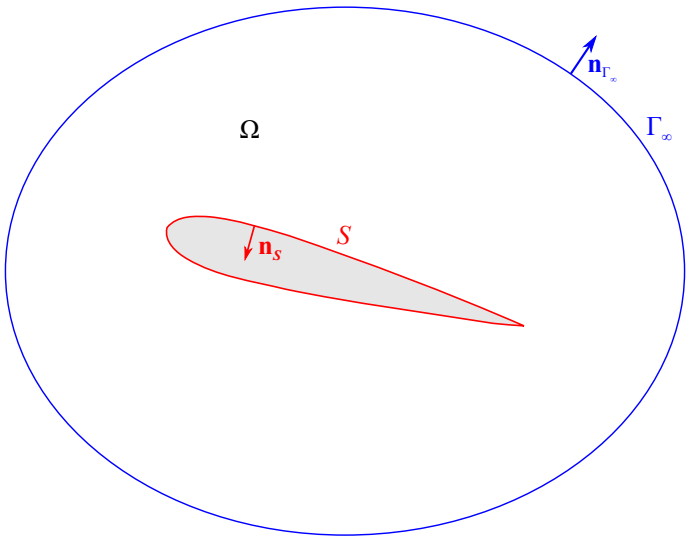

Figure 3.1: External flow over an aerodynamic body. Representation of the flow domain Ω, the far-field boundary Γ_∞, the solid wall boundary S and the corresponding boundary surface normals $\mathbf{n}_{\Gamma_\infty}$ and $\mathbf{n}_S$. (Adapted from Palacios et al. [55].)

The dynamic behavior of a compressible viscous flow around an aerodynamic body can be represented by the Navier-Stokes equations expressed in arbitrary Lagrangian-Eulerian (ALE) [59] differential form with the associated boundary conditions that are problem dependent [57]:

$$\begin{cases} \frac{\partial \mathbf{U}}{\partial t} + \nabla \cdot \mathbf{F}^c_{\text{ALE}} - \nabla \cdot \mathbf{F}^v = \mathbf{Q} & \text{in } \Omega, t > 0, \\ \mathbf{u} = \mathbf{u}_\Omega & \text{on } S, \\ \partial_n T = 0 & \text{on } S, \\ (\mathbf{W})_+ = \mathbf{W}_\infty & \text{on } \Gamma_\infty. \end{cases} \tag{3.1}$$

The ALE form of the governing equations for fluid dynamics allows the study of unsteady flow problems with surfaces in motion. The system of equations is explained in more detail in the following. Regarding the notation, $(\cdot)^\intercal$ is the transpose operation, $\partial_n(\cdot)$ is the

normal gradient operator at a surface point, i.e., $\mathbf{n}_S \cdot \nabla(\cdot)$, and $\mathbf{n}$ is the unit normal vector.

- The partial differential equations of the first line correspond to the conservation of mass, momentum and energy in the fluid. They are defined in a flow domain $\Omega \subset \mathbb{R}^3$. $\mathbf{U}$ is the vector of conservative variables at a point in Ω and at a given instance in time t:

$$\mathbf{U} = \begin{bmatrix} \rho \\ \rho \mathbf{u} \\ \rho E \end{bmatrix}, \tag{3.2}$$

where ρ is the fluid density, $\mathbf{u} = [u, v, w]^\intercal \in \mathbb{R}^3$ is the flow velocity vector in a Cartesian system of reference, and E is the total energy per unit mass. $\mathbf{U}$ has five components in 3D and four in 2D.

The convective and viscous fluxes are given by

$$\mathbf{F}^c_{\text{ALE}} = \begin{bmatrix} \rho(\mathbf{u} - \mathbf{u}_\Omega) \\ \rho \mathbf{u} \otimes (\mathbf{u} - \mathbf{u}_\Omega) + p\mathbf{I} \\ \rho E(\mathbf{u} - \mathbf{u}_\Omega) + p\mathbf{u} \end{bmatrix}, \tag{3.3}$$

$$\mathbf{F}^v = \begin{bmatrix} \cdot \\ \boldsymbol{\tau} \\ \boldsymbol{\tau} \cdot \mathbf{u} + \kappa_{\text{tot}} c_p \nabla T \end{bmatrix}, \tag{3.4}$$

where $\mathbf{u}_\Omega$ is the velocity of the domain in motion, which corresponds to the local mesh velocity after discretization. In the ALE formulation of the governing equations, the movement of the domain is included in the convective flux terms $\mathbf{F}^c_{\text{ALE}}$ and all boundary conditions take into account any movement of the boundaries. If the mesh is fixed, then $\mathbf{u}_\Omega = 0$ and the system of equations (3.1) reduces to an Eulerian formulation.

Assuming a perfect gas, the static pressure p is given by

$$p = (\gamma - 1)\rho \left[E - \frac{1}{2}(\mathbf{u} \cdot \mathbf{u}) \right], \tag{3.5}$$

where γ is the ratio of specific heats, which is equal to 1.4 for air. The temperature T is determined from the perfect gas law,

$$T = \frac{p}{\rho R}, \tag{3.6}$$

with the gas constant R. The specific heat at constant pressure c_p is

$$c_p = \frac{\gamma R}{\gamma - 1}. \tag{3.7}$$

For a Newtonian fluid, the viscous stress tensor τ is given by

$$\boldsymbol{\tau} = \mu_{\text{tot}} \left(\nabla \mathbf{u} + \nabla \mathbf{u}^{\mathsf{T}} - \frac{2}{3} \mathbf{I} (\nabla \cdot \mathbf{u}) \right). \tag{3.8}$$

Viscous turbulent flows can be modelled by the unsteady Reynolds-averaged Navier-Stokes[1] (RANS) equations using a turbulence model. The conservative quantities represent in this case averaged quantities. The standard turbulence models are based on the Boussinesq hypothesis [60], which represents the effect of unresolved turbulent fluctuations on the mean flow as an increased viscosity. The dynamic viscosity appearing in the momentum and energy equations of the Navier-Stokes equations is then replaced by a total viscosity μ_{tot} defined by

$$\mu_{\text{tot}} = \mu_{\text{dyn}} + \mu_{\text{tur}}. \tag{3.9}$$

The laminar dynamic viscosity μ_{dyn} expresses an intrinsic property of the fluid, while the turbulent eddy viscosity μ_{tur} comes from turbulence modeling. The dynamic viscosity is determined from Sutherland's law [61], and is thus a function of the temperature, i.e., $\mu_{\text{dyn}} = \mu_{\text{dyn}}(T)$. The turbulent viscosity is calculated by a suitable turbulence model such as the Spalart-Allmaras model described in the next section. Similarly, the effective thermal conductivity κ_{tot} is given by

$$\kappa_{\text{tot}} = \frac{\mu_{\text{dyn}}}{Pr_{\text{dyn}}} + \frac{\mu_{\text{tur}}}{Pr_{\text{tur}}}, \tag{3.10}$$

where Pr_{dyn} and Pr_{tur} are respectively the dynamic and turbulent Prandtl numbers, which are both assumed to be constant.

Finally, $\mathbf{Q}$ represents a generic source term.

- The second line of the system of equations (3.1) represents the no-slip boundary condition for viscous flows at a solid wall S in arbitrary motion.
- The third expression corresponds to the adiabatic condition at the solid wall S. The adiabatic condition is chosen here, but an isothermal condition could also be used.
- The last line of the system of equations (3.1) represents a far-field characteristic-based condition on the far-field boundary. The fluid state at the far-field boundary is

[1] Formally, the Favre average is used for compressible flows.

defined using the free-stream conditions depending on the characteristic variables $\mathbf{W}$ [14]. Incoming characteristics $(\mathbf{W})_+$ mean that the information originating at the boundary propagates into the interior of the domain. Physical boundary conditions (e.g., free-stream conditions, stagnation conditions, back pressure, etc.) are prescribed for any incoming characteristics.

Spalart-Allmaras turbulence model

The Spalart-Allmaras (S-A) model is a one-equation turbulence model for aerodynamic flows based on a transport equation for a single scalar variable called the effective turbulent viscosity $\tilde{\nu}$, derived from empiricism and dimensional analysis [62]. The model has been calibrated based on 2D mixing layers, wakes and flat-plate boundary layers. The Spalart-Allmaras turbulence model performs well in predicting boundary layers in pressure gradients, and is commonly used to compute external attached flows and mild flow separations encountered on aircraft wings. The SU2 code uses the standard Spalart-Allmaras one-equation model [62]. This most commonly used implementation of the Spalart-Allmaras model does not include rotation correction for vortex-dominated flows[2]. All turbulent flow simulations in this thesis rely on the standard S-A model but other models, such as the Menter SST turbulence model [63], could equally be considered.

The turbulent viscosity μ_{tur} is determined from the following relations that involve the flow state and the effective turbulent viscosity $\tilde{\nu}$:

$$\mu_{\text{tur}} = \rho \hat{\nu} f_{v1}, \tag{3.11}$$

$$f_{v1} = \frac{\chi^3}{\chi^3 + c_{v1}^3}, \tag{3.12}$$

$$\chi = \frac{\hat{\nu}}{\nu}, \tag{3.13}$$

$$\nu = \frac{\mu_{\text{dyn}}}{\rho}, \tag{3.14}$$

where ν is the kinematic viscosity. The following transport equation for the effective eddy viscosity $\hat{\nu}$ is solved together with the RANS equations:

$$\begin{cases} \frac{\partial \hat{\nu}}{\partial t} + \nabla \cdot \mathbf{F}^c_{\text{ALE}} - \nabla \cdot \mathbf{F}^v = \mathbf{Q} & \text{in } \Omega, t > 0, \\ \hat{\nu} = 0 & \text{on } S, \\ \hat{\nu} = \sigma_\infty \nu & \text{on } \Gamma_\infty. \end{cases} \tag{3.15}$$

[2]The rotation correction reduces the eddy viscosity in regions where the vorticity exceeds the strain rate (e.g, in the vortex core region where the pure rotation can suppress the turbulence).

The convective, viscous and source terms are calculated as follows:

$$\mathbf{F}^{c}_{\mathrm{ALE}} = (\mathbf{u} - \mathbf{u}_{\Omega})\hat{\nu}, \tag{3.16}$$

$$\mathbf{F}^{v} = -\frac{\nu + \hat{\nu}}{\sigma}\nabla\hat{\nu}, \tag{3.17}$$

$$\mathbf{Q} = c_{b1}\hat{S}\hat{\nu} - c_{w1}f_{w}\left(\frac{\hat{\nu}}{d_S}\right)^2 + \frac{c_{b2}}{\sigma}|\nabla\hat{\nu}|^2. \tag{3.18}$$

The production term $\hat{S}$ is

$$\hat{S} = |\boldsymbol{\omega}| + \frac{\hat{\nu}}{\kappa^2 d_S^2}f_{v2}, \tag{3.19}$$

where $\boldsymbol{\omega} = \nabla \times \mathbf{u}$ corresponds to the fluid vorticity, $|\boldsymbol{\omega}|$ is the vorticity magnitude, d_S is the distance to the closest wall, and the function f_{v2} is computed as

$$f_{v2} = 1 - \frac{\chi}{1 + \chi f_{v1}}. \tag{3.20}$$

The expression of the function f_w is

$$f_w = g\left(\frac{1 + c_{w3}^6}{g^6 + c_{w3}^6}\right)^{1/6}, \tag{3.21}$$

$$g = r + c_{w2}(r^6 - r), \tag{3.22}$$

$$r = \frac{\hat{\nu}}{\hat{S}\kappa^2 d_S^2}. \tag{3.23}$$

The constants are $\sigma = 2/3$, $c_{b1} = 0.1355$, $c_{b2} = 0.622$, $\kappa = 0.41$, $c_{w1} = c_{b1}/\kappa^2 + (1 + c_{b2})/\sigma$, $c_{w2} = 0.3$, $c_{w3} = 2$ and $c_{v1} = 7.1$.

The variable $\hat{\nu}$ is equal to zero at walls and is set to a fraction σ_∞ of the laminar viscosity at the far-field. The recommended value for σ_∞ at the free stream is between 3 and 5 for fully-turbulent behavior as stated in Spalart and Rumsey [64]. The Spalart-Allmaras turbulence model cannot predict the transition point. The boundary layer is therefore considered turbulent over the entire surface of the structure.

Numerical methods

In the CFD code SU2, the spatial discretization of the governing equations is achieved through the finite volume method (FVM) on a dual-grid using a vertex-based approach so that the nodes of the primal grid represent the centers of the control volumes [14]. The convective fluxes can be discretized using second-order centered schemes such as the

Jameson-Schmidt-Turkel (JST) scheme [65]. The spatial gradients of the flow variables can be computed by a weighted least-squares method at all grid nodes. These gradients are then averaged to obtain the gradients at the cell faces required to evaluate the viscous fluxes.

For unsteady flows, a dual time-stepping approach [66] is used for second-order accurate time integration where each physical time step is transformed into a steady problem for which steady-state acceleration techniques can be used.

3.1.3 Compressible unsteady Euler equations

Ignoring the viscous effects, the Navier-Stokes equations simplify to the Euler equations. The Euler modeling of a flow problem can be represented by the inviscid form of the governing flow equations expressed in ALE differential form with the corresponding boundary conditions:

$$\begin{cases} \frac{\partial \mathbf{U}}{\partial t} + \nabla \cdot \mathbf{F}^c_{\mathrm{ALE}} = \mathbf{Q} & \text{in } \Omega, t > 0, \\ (\mathbf{u} - \mathbf{u}_\Omega) \cdot \mathbf{n} = 0 & \text{on } S, \\ (\mathbf{W})_+ = \mathbf{W}_\infty & \text{on } \Gamma_\infty, \end{cases} \tag{3.24}$$

where

$$\mathbf{U} = \begin{bmatrix} \rho \\ \rho \mathbf{u} \\ \rho E \end{bmatrix}, \tag{3.25}$$

$$\mathbf{F}^c_{\mathrm{ALE}} = \begin{bmatrix} \rho(\mathbf{u} - \mathbf{u}_\Omega) \\ \rho \mathbf{u} \otimes (\mathbf{u} - \mathbf{u}_\Omega) + p\mathbf{I} \\ \rho E(\mathbf{u} - \mathbf{u}_\Omega) + p\mathbf{u} \end{bmatrix}, \tag{3.26}$$

$$\mathbf{Q} = \begin{bmatrix} q_\rho \\ \mathbf{q}_{\rho \mathbf{u}} \\ q_{\rho E} \end{bmatrix}. \tag{3.27}$$

Compared to the unsteady RANS approach described in Section 3.1.2, the viscous fluxes are omitted, the condition on temperature is not needed at walls, and the no-slip condition at a solid wall S is replaced by the flow tangency condition for inviscid flows, which means that the flow cannot penetrate the solid wall.

The methodology will be based on both RANS and Euler simulations. Once such solutions are obtained for a given frequency, the dominant dynamic modes are then extracted using DMD as explained in the following section.

3.1.4 Dynamic mode decomposition

Dynamic mode decomposition (DMD) is a modal decomposition technique capable of extracting information about the dynamical processes contained in a sequence of flow fields [67–69]. DMD is independent of the method used to generate the flow fields, and is thus exclusively data-based. The flow fields can be either generated by numerical simulations or measured experimentally (e.g., particle image velocimetry measurements). DMD can also be used to analyze subdomains of the entire computational domain.

The dynamic mode decomposition algorithm is applied to a sequence of N flow fields or snapshots represented by a snapshot matrix $\mathbf{V}_1^N$:

$$\mathbf{V}_1^N = \begin{bmatrix} \mathbf{v}_1 & \mathbf{v}_2 & \mathbf{v}_3 & \dots & \mathbf{v}_N \end{bmatrix}, \tag{3.28}$$

where $\mathbf{v}_n$ denotes a vector representing the nth flow field. In fluid mechanics, the number of data points is in most cases much larger than the number of snapshots. As a result, the row dimension of the matrix $\mathbf{V}_1^N$ is typically larger than the column dimension. Two consecutive snapshots $\mathbf{v}_n$ and $\mathbf{v}_{n+1}$ are assumed to be separated by a constant time step Δt that must be small enough so that the relevant dynamic processes present in the flow response can be extracted from the input data sequence. According to the Nyquist criterion, the sampling frequency must be at least twice the characteristic frequency of a process in order to identify this process. Schmid [67] recommends choosing a sampling frequency equal to about three times the Nyquist limit to obtain accurate results with DMD.

The application of the DMD procedure results in $N-1$ modes, each mode consisting of an amplitude α_i, a spatial mode shape $\boldsymbol{\phi}_i(x,y,z)$ and a time behavior given by the eigenvalue λ_i such that the evolution of the flow field can be expressed as

$$\mathbf{v}(t) = \sum_{i=0}^{N-2} \alpha_i \boldsymbol{\phi}_i \mathrm{e}^{\lambda_i t}. \tag{3.29}$$

The mode shape vector does not depend on time; all the time dependence is in the complex exponential term. The real and imaginary parts of the mode eigenvalue λ_i represent respectively the rate of decay/growth and the frequency associated with this dynamic mode. If the unsteady flow has reached a fully established periodic state, then the real part of λ_i (decay/growth) is zero. The modes that contribute most to the dynamics must then be identified among all $N-1$ modes. The DMD algorithm used in this thesis is described below.

A constant linear mapping $\mathbf{A}$ is assumed between two consecutive snapshots:

$$\mathbf{v}_{n+1} = \mathbf{A}\mathbf{v}_n, \qquad n \in \{1,2,3,\dots,N-1\}. \tag{3.30}$$

The sequence of snapshots can then be formulated as a Krylov sequence:

$$\mathbf{V}_1^N = \begin{bmatrix} \mathbf{v}_1 & \mathbf{A}\mathbf{v}_1 & \mathbf{A}^2\mathbf{v}_1 & \dots & \mathbf{A}^{N-1}\mathbf{v}_1 \end{bmatrix}. \tag{3.31}$$

The objective of DMD is to extract dynamic characteristics of the physical process described by the matrix $\mathbf{A}$, which is usually not known a priori and needs to be approximated from the sequence of snapshots.

If the sequence $\mathbf{V}_1^N$ includes a sufficiently large number of snapshots, the dominant features of the related physical process are captured by $\mathbf{V}_1^N$. Therefore, the snapshots may be assumed to become linearly dependent beyond a certain number. The last snapshot $\mathbf{v}_N$ is then written as a linear combination of the previous snapshots $\begin{bmatrix} \mathbf{v}_1 & \mathbf{v}_2 & \mathbf{v}_3 & \dots & \mathbf{v}_{N-1} \end{bmatrix}$:

$$\mathbf{v}_N = \mathbf{V}_1^{N-1}\mathbf{a} + \mathbf{r}, \tag{3.32}$$

where $\mathbf{a} = \begin{bmatrix} a_1 & a_2 & a_3 & \dots & a_{N-1} \end{bmatrix}^\intercal$ is the vector containing the coefficients of the linear combination and $\mathbf{r}$ is the residual vector. The following matrix relation can then be written [70]:

$$\mathbf{V}_2^N = \mathbf{A}\mathbf{V}_1^{N-1} = \mathbf{V}_1^{N-1}\mathbf{S} + \mathbf{r}\mathbf{e}_{N-1}^\intercal, \tag{3.33}$$

where $\mathbf{S}$ is a companion matrix given by

$$\mathbf{S} = \begin{bmatrix} 0 & & & & a_1 \\ 1 & 0 & & & a_2 \\ & \ddots & \ddots & & \vdots \\ & & 1 & 0 & a_{N-2} \\ & & & 1 & a_{N-1} \end{bmatrix}, \tag{3.34}$$

and $\mathbf{e}_{N-1}^\intercal = \begin{bmatrix} 0 & 0 & \dots & 1 \end{bmatrix} \in \mathbb{R}^{N-1}$. By construction, some of the eigenvalues of the matrix $\mathbf{A}$ are approximated by those of the companion matrix $\mathbf{S}$. The last column of $\mathbf{S}$ contains the components of $\mathbf{a}$, which are unknown. The vector $\mathbf{a}$ can be obtained by calculating the least-squares solution of Equation (3.32) using a QR decomposition of the sample sequence $\mathbf{V}_1^{N-1}$:

$$\mathbf{V}_1^{N-1} = \mathbf{Q}\mathbf{R}, \tag{3.35}$$

where $\mathbf{Q}$ is an unitary matrix (i.e., its conjugate transpose $\mathbf{Q}^H$ equals its matrix inverse $\mathbf{Q}^{-1}$) and $\mathbf{R}$ is an upper triangular matrix. The vector $\mathbf{a}$ is then given by

$$\mathbf{a} = \mathbf{R}^{-1}\mathbf{Q}^H\mathbf{v}_N. \tag{3.36}$$

However, in practice, the decomposition algorithm using the companion matrix $\mathbf{S}$ is ill-conditioned and often only the first two dominant dynamic modes of the physical process can be extracted, especially with noisy experimental data [67].

A more robust computation is obtained by using a full matrix $\tilde{\mathbf{S}}$ related to $\mathbf{S}$ by a similarity transformation. First, a singular value decomposition of $\mathbf{V}_1^{N-1}$ is evaluated:

$$\mathbf{V}_1^{N-1} = \mathbf{U}\boldsymbol{\Sigma}\mathbf{W}^H, \tag{3.37}$$

where $\mathbf{U}$ and $\mathbf{W}$ are unitary matrices, $\mathbf{W}^H$ is the conjugate transpose of $\mathbf{W}$, and $\boldsymbol{\Sigma}$ is a diagonal matrix whose elements are the singular values of $\mathbf{V}_1^{N-1}$. The matrix $\mathbf{U}$ contains the spatial structures of the proper orthogonal modes (PODs) for the snapshot matrix $\mathbf{V}_1^N$ [47, 67]. Then, substituting Equation (3.37) in Equation (3.33) gives

$$\mathbf{U}^H\mathbf{A}\mathbf{U} = \mathbf{U}^H\mathbf{V}_2^N\mathbf{W}\boldsymbol{\Sigma}^{-1} = \tilde{\mathbf{S}}. \tag{3.38}$$

The spatial structure of each DMD mode $\boldsymbol{\phi}_i$ is then obtained as

$$\boldsymbol{\phi}_i = \mathbf{U}\mathbf{y}_i, \tag{3.39}$$

where $\mathbf{y}_i$ is the ith eigenvector of $\tilde{\mathbf{S}}$:

$$\tilde{\mathbf{S}}\mathbf{y}_i = \mu_i\mathbf{y}_i. \tag{3.40}$$

The extracted DMD modes accurately describe the dynamical behavior contained in the data sequence. The snapshots can be estimated by a superposition of the r retained dynamic modes scaled by their complex scalar amplitude α_i [69]:

$$\mathbf{v}_n \approx \sum_{i=0}^{r-1} \alpha_i\boldsymbol{\phi}_i\mu_i^{n-1}, \qquad n \in \{1,2,3,\ldots,N-1\}. \tag{3.41}$$

This expression can be written in matrix form as

$$\underbrace{\begin{bmatrix}\mathbf{v}_1 & \mathbf{v}_2 & \ldots & \mathbf{v}_{N-1}\end{bmatrix}}_{\mathbf{V}_1^{N-1}} \approx \underbrace{\begin{bmatrix}\boldsymbol{\phi}_0 & \boldsymbol{\phi}_1 & \ldots & \boldsymbol{\phi}_{r-1}\end{bmatrix}}_{\boldsymbol{\Phi}} \underbrace{\begin{bmatrix}\alpha_0 & & & \\ & \alpha_1 & & \\ & & \ddots & \\ & & & \alpha_{r-1}\end{bmatrix}}_{\mathbf{D}_\alpha} \underbrace{\begin{bmatrix}1 & \mu_0 & \mu_0^2 & \ldots & \mu_0^{N-2} \\ 1 & \mu_1 & \mu_1^2 & \ldots & \mu_1^{N-2} \\ \vdots & \vdots & \vdots & \ddots & \vdots \\ 1 & \mu_{r-1} & \mu_{r-1}^2 & \ldots & \mu_{r-1}^{N-2}\end{bmatrix}}_{\mathbf{V}_\mu}. \tag{3.42}$$

The Vandermonde matrix $\mathbf{V}_\mu$ governs the temporal evolution of the dynamic modes. Different methods do exist to determine the vector of amplitudes $\boldsymbol{\alpha} = \begin{bmatrix}\alpha_0 & \alpha_1 & \ldots & \alpha_{r-1}\end{bmatrix}^\mathsf{T}$

[69, 71]. The approach followed in this thesis consists in finding the DMD amplitudes that minimize the Frobenius norm of $\mathbf{V}_1^{N-1} - \mathbf{\Phi}\mathbf{D}_\alpha\mathbf{V}_\mu$. As demonstrated by Jovanović et al. [69], the optimal amplitudes of the DMD modes that solve this optimization problem are given by

$$\boldsymbol{\alpha} = \left[\left(\mathbf{y}^H\mathbf{y}\right) \circ \overline{\left(\mathbf{V}_\mu\mathbf{V}_\mu^H\right)}\right]^{-1} \overline{\text{diag}\left(\mathbf{V}_\mu\mathbf{W}\mathbf{\Sigma}^H\mathbf{y}\right)}, \tag{3.43}$$

where the symbol $\circ$ denotes the element-wise multiplication operator, an overline is the complex conjugate operator, and the diag function returns the diagonal elements of a matrix.

The decay rates and frequencies of the individual modes are respectively the real and imaginary parts of $\lambda_i = \log(\mu_i)/\Delta t$. Introducing λ_i in Equation (3.41), one has

$$\mathbf{v}_n \approx \sum_{i=0}^{r-1} \alpha_i\boldsymbol{\phi}_i e^{\lambda_i(n-1)\Delta t}, \qquad n \in \{1,2,3,\ldots,N-1\}. \tag{3.44}$$

3.1.5 Harmonic balance method

When the unsteady dynamics of the problem is time-periodic, harmonic balance (HB) [43, 72–74] represents an interesting alternative to the above approach for obtaining the dominant dynamics modes. In particular, HB assumes that the time behavior of any conservative variable can be expressed as a sum of Fourier modes. HB simulations with only a few modes can thus provide the necessary key dynamic modes at a lower cost than applying DMD to full time-accurate simulations.

The implementation of the harmonic balance method in SU2 used in this thesis assumes that the cells of the mesh do not deform. The motion of the structure can be accounted for by displacing the entire mesh in a rigid-body-like motion following the motion of the structure. This implementation is well-adapted for studying 2D airfoils in *rigid body motion*, as described below, but cannot be used for *deforming* airfoils or wings.

The differential form of the unsteady compressible Navier-Stokes equations can be integrated over a control volume Ω_i surrounding node i using the finite volume method. The semi-discretized form obtained after spatial integration can be written concisely as

$$\frac{d}{dt}\int_{\Omega_i(t)} \mathbf{U}d\Omega + \mathbf{R}_i(\mathbf{U}) = 0, \tag{3.45}$$

where $\mathbf{R}_i(\mathbf{U})$ represents the terms resulting from the spatial discretization at each node. The fully-discrete finite volume form of the governing equations is obtained by discretiz-

ing the time derivative term:

$$|\Omega_i|\mathbf{D}_t\mathbf{U}_i + \mathbf{R}_i(\mathbf{U}) = 0, \tag{3.46}$$

where $|\Omega_i| = \int_{\Omega_i(t)} d\Omega$ is constant for mesh cells that do not deform in time and $\mathbf{D}_t$ is the derivative operator with respect to time.

For unsteady flows, the integration of the flow equations in time is performed using a dual time-stepping strategy [66]. The unsteady problem is transformed into a series of steady-state problems in pseudo-time τ at each physical time step that can be solved using steady-state acceleration techniques [72]:

$$|\Omega_i|\frac{\partial \mathbf{U}_i}{\partial \tau} + |\Omega_i|\mathbf{D}_t\mathbf{U}_i + \mathbf{R}_i(\mathbf{U}) = 0, \tag{3.47}$$

In time-accurate methods, the time derivative term $|\Omega_i|\mathbf{D}_t\mathbf{U}_i$ in Equation (3.47) is seen as a solution-dependent source term in a pseudo-time iteration, and it can be discretized using different explicit or implicit finite difference schemes. On the other hand, in the harmonic balance method implemented in SU2, this time derivative operator is replaced by a harmonic balance operator whose derivation is presented below.

The harmonic balance method solves the governing equations for a specified set of frequencies

$$\boldsymbol{\omega} = \begin{bmatrix} \omega_0 & \omega_1 & \omega_2 & \dots & \omega_K & \omega_{-K} & \dots & \omega_{-1} \end{bmatrix}^\mathsf{T}, \tag{3.48}$$

where $\omega_0 = 0$ rad/s, $\omega_{-k} = -\omega_k$ and K is the number of specified frequencies. In general, the harmonic balance method can be used with unsteady flow problems that include one or several fundamental frequencies, and so the discrete frequencies are not necessarily multiples of each other [3]. The time period T of the HB simulation is divided into $N = 2K + 1$ time instances. A Fourier representation of each conservative variable in time is written using the period and the set of frequencies:

$$\hat{\varphi}_k = \frac{1}{N}\sum_{n=0}^{N-1} \varphi_n \mathrm{e}^{-i\omega_k t_n}, \tag{3.49}$$

or in matrix form using the discrete Fourier transform (DTF) matrix $\mathbf{E}$:

$$\hat{\boldsymbol{\varphi}} = \mathbf{E}\boldsymbol{\varphi}, \tag{3.50}$$

$$E_{k,n} = \frac{1}{N}\mathrm{e}^{-i\omega_k t_n}, \tag{3.51}$$

[3] The reader can refer to Nimmagadda et al. [72] for applications of the HB method to flow problems containing several fundamental frequencies.

where

- $\boldsymbol{\varphi} = \begin{bmatrix} \varphi_0 & \varphi_1 & \varphi_2 & \dots & \varphi_{N-1} \end{bmatrix}^\mathsf{T}$ is a vector containing a single conservative variable in a control volume Ω at the N time instances throughout the period. The nth time instance is $t_n = nT/N$.
- $\hat{\boldsymbol{\varphi}} = \begin{bmatrix} \hat{\varphi}_0 & \hat{\varphi}_1 & \hat{\varphi}_2 & \dots & \hat{\varphi}_K & \hat{\varphi}_{-K} & \dots & \hat{\varphi}_{-1} \end{bmatrix}^\mathsf{T}$ is the N-vector of Fourier coefficients in the frequency domain.

Applying the time derivative operator $\mathbf{D}_t$ to $\boldsymbol{\varphi}$ and noting that $\hat{\boldsymbol{\varphi}}$ does not depend on time give

$$\mathbf{D}_t \boldsymbol{\varphi} = \mathbf{D}_t (\mathbf{E}^{-1} \hat{\boldsymbol{\varphi}}) = \frac{\partial \mathbf{E}^{-1}}{\partial t} \hat{\boldsymbol{\varphi}} = \frac{\partial \mathbf{E}^{-1}}{\partial t} \mathbf{E} \boldsymbol{\varphi}, \tag{3.52}$$

and therefore

$$\mathbf{D}_t = \frac{\partial \mathbf{E}^{-1}}{\partial t} \mathbf{E}. \tag{3.53}$$

If the flow problem has only one fundamental frequency, the discrete frequencies specified in Equation (3.48) are $\omega_k = k2\pi/T$. In this case, the inverse Fourier transform $\mathbf{E}^{-1}$ and its time derivative appearing in Equation (3.53) have an analytic expression:

$$E^{-1}_{n,k} = \mathrm{e}^{i\omega_k t_n}, \tag{3.54}$$

$$\frac{\partial \mathbf{E}^{-1}}{\partial t} = \mathbf{E}^{-1} \mathbf{D}, \tag{3.55}$$

where $\mathbf{D}$ is a diagonal matrix with $D_{kk} = i\omega_k$. If the flow problem has several fundamental frequencies, it is easier to first write an analytical expression directly for $\mathbf{E}^{-1}$ in order to determine its derivative, and calculate $\mathbf{E}$ by numerically inverting $\mathbf{E}^{-1}$ [72].

For HB simulations, the time derivative of the conservative variables in Equation (3.47) of the dual-time stepping method is replaced by the product of the harmonic balance operator given by Equation (3.53) and the vector of the conservative variables at the N time instances. This product is considered as a source term, it connects each time instance to the other instances. Therefore, the unsteady problem is solved using N steady-state simulations that are marched simultaneously towards steady state in pseudo-time. The N converged steady-state flow solutions can then be spectrally interpolated to obtain the continuous unsteady solution. A disadvantage of the HB method is that it can become expensive in terms of memory requirements for a large number of input frequencies because the solver has to store the solutions for all time instances.

In the case of the flow response to periodic small amplitude oscillations of a structure at a given frequency, the computation time of the HB method with one mode is of the same

order as the linear frequency domain (LFD) [75–77], although the LFD method should be faster for multiple frequencies. However, the one-mode HB method is more accurate than the LFD method. The LFD method becomes less accurate as soon as moving shocks appear in the transonic flow regime. The reason of this loss of accuracy is related to the fact that the mean solution of the LFD method is obtained by a steady-state simulation at the mean position of the structure. However, the average position of the moving shocks can deviate significantly from their static position determined at the mean position of the structure. This discrepancy affects the accuracy of the LFD method to predict unsteady transonic flows [75–77].

3.2 Simulations of the transonic flow around a pitching NACA 64A010

The present section assesses the performance of the unsteady Euler and RANS approaches for predicting the unsteady transonic flow around a pitching airfoil. This configuration has been chosen for validation purposes, and it allows the study of shock waves that move due to structural oscillations.

The 2D transonic flow over a NACA 64A010 airfoil pitching around its quarter-chord point is used as a test case, based on the experiment performed by Davis [79]. The free-stream Mach number M_∞ is 0.796 and the Reynolds number Re based on the chord c is 12.56×10^6. The pitching motion at constant frequency is specified as

$$\alpha(\tau) = \bar{\alpha} + \hat{\alpha}\sin(k\tau), \tag{3.56}$$

where $\alpha(\tau)$ is the variation of the angle of attack with the non-dimensional time $\tau = tU_\infty/b$, U_∞ is the free-stream velocity, the semi-chord $b = c/2$, $\bar{\alpha}$ is the mean angle of attack, $\hat{\alpha}$ is the pitching amplitude, and the forcing reduced frequency is defined as $k = \omega b/U_\infty$ with ω the angular frequency. Unless otherwise specifically mentioned, all of the following results are obtained for $\bar{\alpha} = 0°$, $\hat{\alpha} = 1.01°$ and $k = 0.202$. As the mean angle of attack and pitching amplitude are small, massive separation of the flow does not occur.

The open source three-dimensional finite element mesh generator Gmsh [80] is used to create the meshes. The boundaries of the computational domain are located approximately $50c$ away from the airfoil in order to minimize their impact on the solution in the region of interest as illustrated in Figure 3.2. A C-type grid is appropriate for flows over an airfoil with a sharp trailing edge.

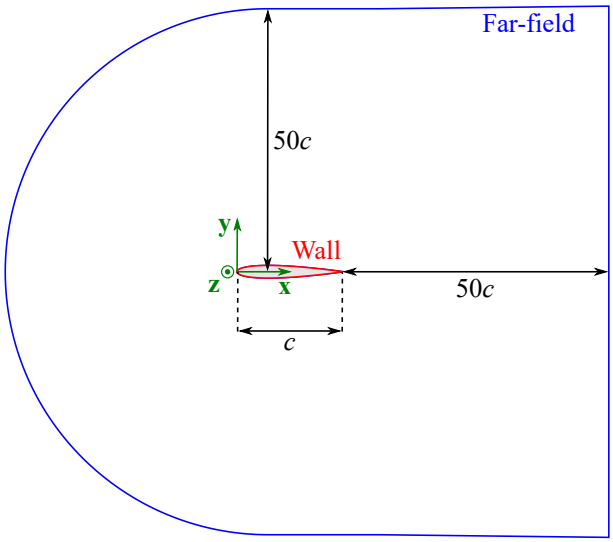

Figure 3.2: Computational domain for the pitching NACA 64A010 case.

The quality of the mesh is critical for the accuracy of the results. A body-fitted C-type structured grid is chosen for this simple geometry, as shown in Figure 3.3, because it is more efficient than an unstructured grid in terms of CPU time and memory requirements for the same accuracy [14]. The cells are clustered near the wall and wake regions where the flow varies strongly. Grid stretching is applied in the normal direction in order to decrease the computational cost. The size of the grid cells varies in a continuous way in all directions. The distortions of the grid are minimized.

The RANS model has a specific requirement in terms of mesh size at the wall in order to properly capture the turbulent boundary layer. The cells are orthogonal to the wall and the first grid spacing along the entire airfoil is set such that the distance normal to the wall in wall units y^+ satisfies the following criterion

$$y^+ = \frac{y u_*}{\nu} \lesssim 1, \tag{3.57}$$

$$u_* = \sqrt{\frac{\tau_w}{\rho}}, \tag{3.58}$$

$$\tau_w = \mu \left. \frac{\partial u}{\partial y} \right|_{y=0}, \tag{3.59}$$

where y is the distance normal to the surface, μ is the dynamic viscosity, τ_w is the wall shear stress, u_* is the friction velocity, and ν is the kinematic viscosity. This criterion is required in order to properly capture the turbulent boundary layer without using a wall function in the Spalart-Allmaras turbulence model.

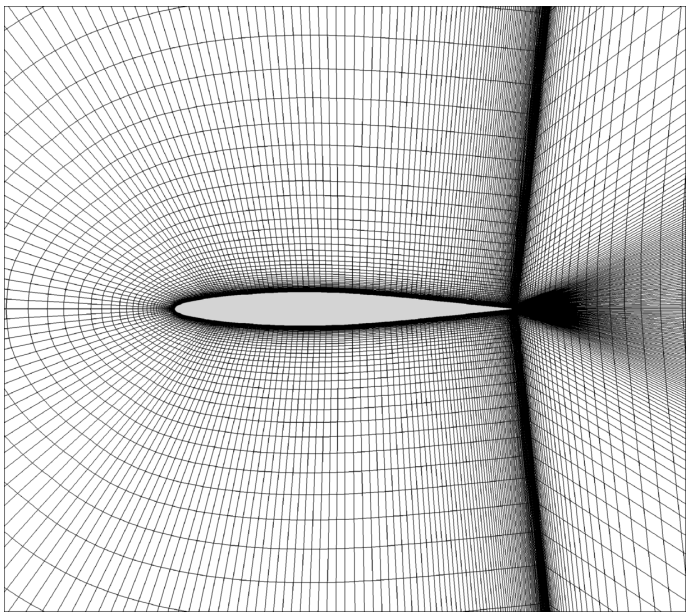

Figure 3.3: Computational grid used for the unsteady RANS simulations corresponding to Mesh II.

The characteristics of the mesh are defined so as to minimize the numerical error introduced by the spatial discretization. A grid refinement analysis is presented on the unsteady RANS simulations using the S-A model. The same simulation is performed on finer and finer grids, and the variation of the solution is analyzed. Three levels of grid refinement are considered. The first cell at the wall remains the same in each mesh. The number of cells increases from Mesh I to Mesh III as indicated in Table 3.1.

Mesh	**Number of points:**			**Number of quadrilaterals**
	around the airfoil	**in the normal direction**	**in the wake**	
I	200	86	52	26144
II	250	108	64	40824
III	300	130	76	58760

Table 3.1: Computational grid characteristics for the unsteady RANS simulations. Three levels of grid refinement are chosen for the grid convergence study.

The open-source CFD code SU2 is used to compute the unsteady flow problem on a rigidly transforming mesh. The choice of the time step is dictated by the smallest physical time scale of the flow that needs to be resolved and numerical stability. The time-accurate simulations use 25 time steps per period of oscillation to capture the relevant time scales. The free-stream flow state is used as the initial condition. The flow being time-periodic, the calculation is run over several periods of oscillation until transient effects are eliminated and a periodic state is reached.

Figure 3.4 shows the unsteady lift and drag coefficients obtained for simple harmonic motion using the RANS approach and the three meshes. Refining Mesh II does not change the solutions (i.e., grid independence is achieved) while the increase of the computational cost is not negligible. This grid convergence study confirms that the resolution of Mesh II is sufficient to provide accurate RANS results. In the following sections, the results computed using Mesh II are analyzed. A similar resolution is used for the Euler simulations presented in this work except that the first spacing is larger ($y \approx c/100$). Another important observation is that the unsteady simulation quickly reaches the periodic state for this problem with a boundary undergoing simple harmonic oscillations of small amplitude.

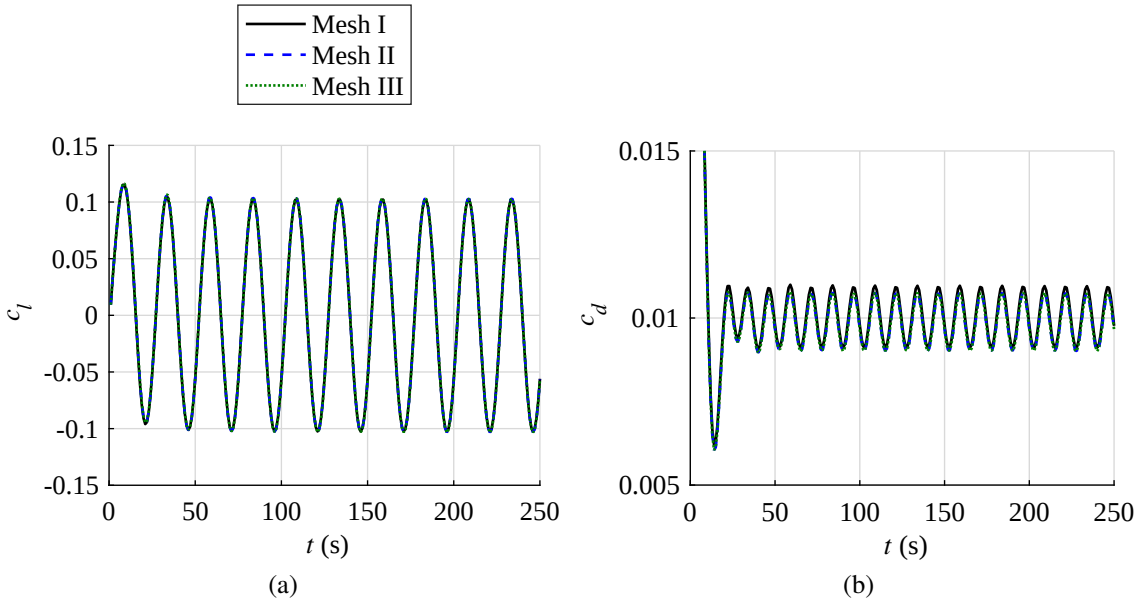

Figure 3.4: (a) Lift coefficient c_l and (b) drag coefficient c_d as a function of time t obtained by unsteady RANS simulations for three levels of grid refinement.

Figure 3.5 shows three snapshots of the Mach number field M at three instances of the oscillation cycle computed by Euler and RANS simulations. The free-stream flow is subsonic ($M_\infty < 1$) but close to 1. The flow becomes locally supersonic ($M > 1$) in some regions around the airfoil. These supersonic regions are delimited by the sonic lines ($M = 1$) represented by the black line in Figure 3.5. The shock waves lie at the downstream edge of the supersonic regions and their position and strength clearly vary over time due to the motion of the airfoil. Both the Euler and RANS models capture these moving shock waves.

The RANS solution includes the viscous boundary layer and wake. The shock waves can interact with the boundary layer. In this reference case, the boundary layer is very thin because the Reynolds number is large ($Re = 12.56 \times 10^6$) and it remains attached as the angle of attack remains small throughout the motion ($\bar{\alpha} = 0^\circ$ and $\hat{\alpha} = 1.01^\circ$). Massive flow separation does not occur in the reference case. Therefore, the Euler and RANS

models predict similar flow fields.

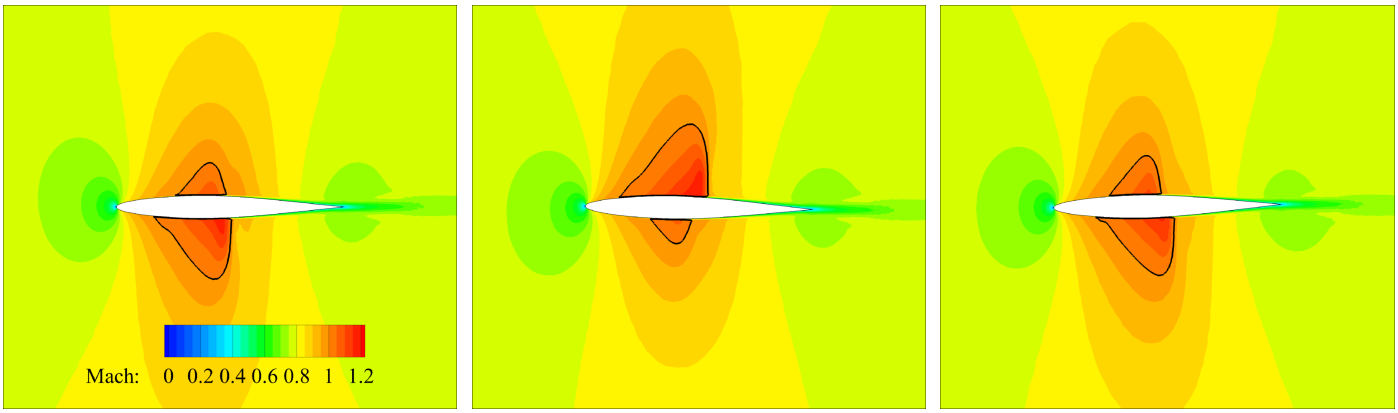

(a) $k\tau = 0°$ (b) $k\tau = 120°$ (c) $k\tau = 240°$

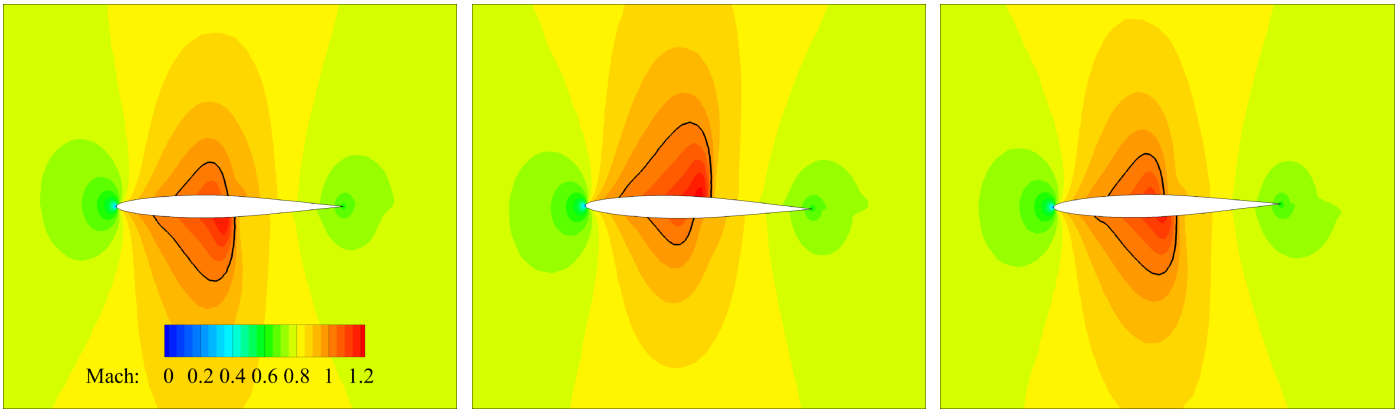

(d) $k\tau = 0°$ (e) $k\tau = 120°$ (f) $k\tau = 240°$

Figure 3.5: Contours of the Mach number M at different phases $k\tau$ of the forced oscillation cycle obtained by (a–c) an unsteady RANS simulation and (d–f) an unsteady Euler simulation. The black line represents the isoline $M = 1$.

The numerical results are compared with the experimental measurements in order to evaluate their accuracy. In the following figures, the black and blue curves are respectively associated with the RANS and Euler simulations. In Figure 3.6, the variation of the lift coefficient c_l in time is calculated from the pressure field. It can be seen that the RANS lift coefficient is slightly closer to the experiment compared to the Euler solution.

The chordwise location of the shock on the upper surface x_s is defined as the location of the maximum gradient of the pressure coefficient C_p similarly to the experiment. There is a slight shift between the Euler and RANS solutions because the thin attached boundary layer slightly modifies the pressure distribution compared to the inviscid case. The RANS solution is in slightly better agreement with the experimental results. The shock motion on the lower surface is similar due to the symmetry of the problem. Some discrepancies appear between the numerical and experimental data in the second half of the oscillation

cycle, probably because the shock wave on the upper surface becomes very weak so that it is difficult to define a precise shock position, even experimentally.

Overall, the time response of the lift coefficient and the motion of the shock wave predicted by the Euler and RANS models are both in good agreement with the experimental measurements for the reference conditions.

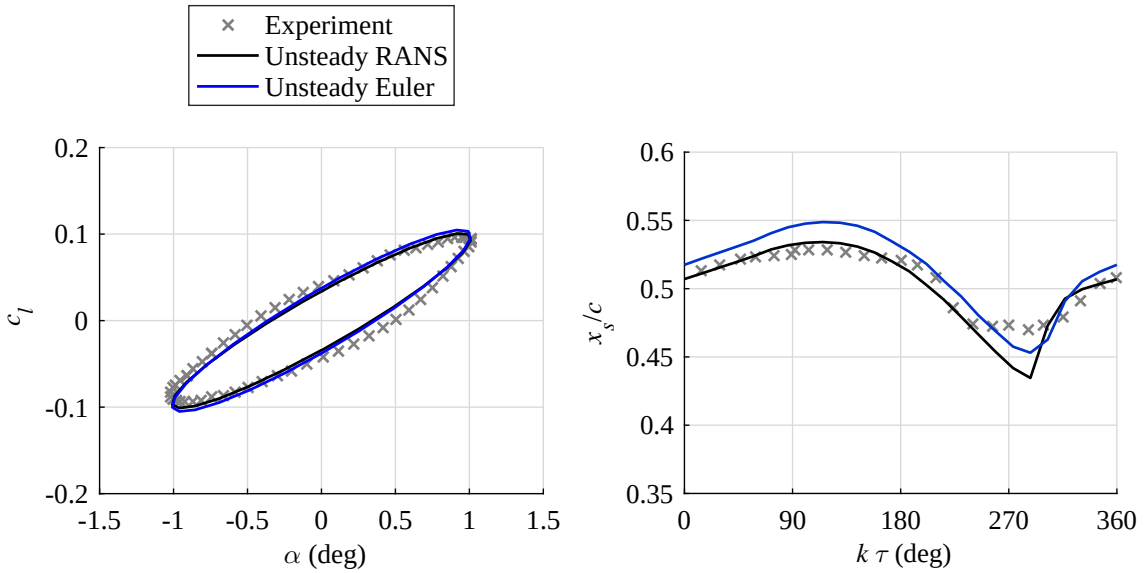

(a) Lift coefficient c_l as a function of the angle of attack α

(b) Chordwise position of the shock wave on the upper surface x_s over one oscillation cycle

Figure 3.6: Comparison of the unsteady RANS and Euler solutions with the experimental data of Davis [79] for the reference pitching NACA 64A010 case at the reduced frequency $k = 0.202$.

The DMI methodology aims to obtain the flow response to an imposed periodic deformation of the structure at any frequency by interpolating the most dominant flow dynamic modes obtained from a few high-fidelity simulations at different frequencies. The following section analyzes the relative contribution of the modes at a fixed forcing frequency. The objective is to determine how many flow dynamic modes are required to capture the flow dynamics with sufficient accuracy.

3.2.1 Contribution of the dynamic modes to the flow dynamics

High-fidelity flow simulations provide the entire flow field around the oscillating structure as a function of time. After the initial transient phase, the unsteady flow fields can be processed using dynamic mode decomposition to extract information about the flow response dynamics. The flow region used for DMD analysis is a square of side $2c$ centered on the airfoil. This spatial size is large enough to include the supersonic regions. Only one period of oscillation is considered, i.e., the transient phase is discarded, and 25 snapshots

are used.

Figure 3.7 shows the resulting modal amplitude α_i against the corresponding modal reduced frequency $\Im(\lambda_i)b/U_\infty$ of each DMD mode for the Euler and RANS simulations carried out at $k = 0.202$. Each modal amplitude distribution is discrete. The spectrum is symmetrical with respect to $\Im(\lambda_i) = 0$ because the input data are real [67]. The dynamic modes appear in complex conjugate pairs. For example, the dynamic modes associated with $i = 1$ and $i = 2$ are complex conjugates. Moreover, the eigenvalues are purely imaginary, i.e., there is no damping of the modes as the flow's time response is fully periodic after the transient phase.

The free stream has not been removed from the input flow data in this analysis. The highest peak represents the contribution of the mean flow, which is constant over time. The modal reduced frequency $\Im(\lambda_0)b/U_\infty$ associated with this mode is equal to zero. The next peak corresponds to the flow dynamic mode 1. It appears at the fundamental frequency corresponding to the frequency at which the pitching motion is forced such that $\Im(\lambda_1)b/U_\infty = k$.

This first dynamic mode contributes most to the flow dynamics. The higher harmonics (i.e., integer multiples of the fundamental frequency) are well distinguishable but their amplitude decreases rapidly with the modal frequency. This decrease is steeper in the Euler solution. Therefore, the modes at high $\Im(\lambda_i)b/U_\infty$ make a relatively small contribution to the flow dynamics. The dynamic modes include smaller and smaller scales as the modal frequency $\Im(\lambda_i)$ increases.

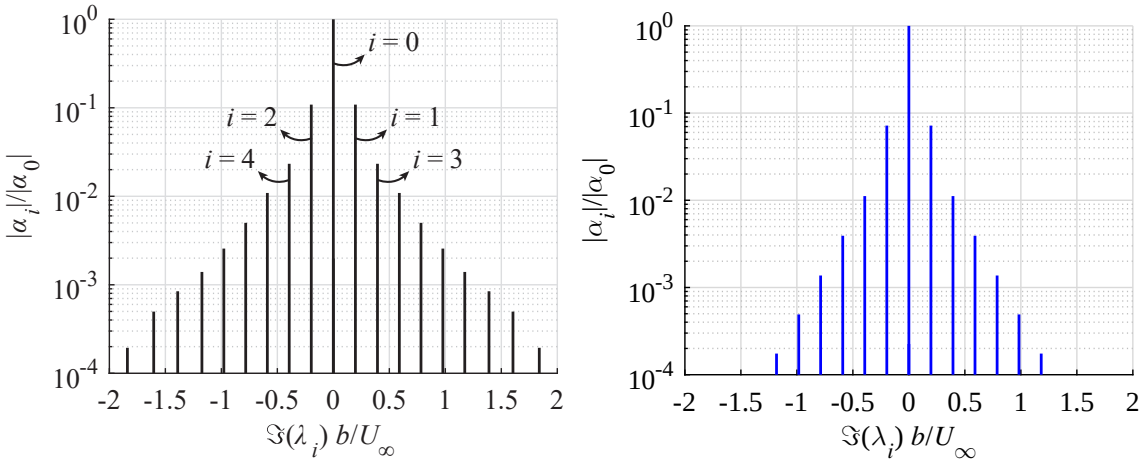

(a) Unsteady RANS

(b) Unsteady Euler

Figure 3.7: Absolute value of the modal amplitude $|\alpha_i|$ as a function of the modal reduced frequency $\Im(\lambda_i)b/U_\infty$ of the flow modes obtained by DMD of (a) unsteady RANS and (b) unsteady Euler pressure coefficient fields for the pitching NACA 64A010 case at the reduced frequency $k = 0.202$.

The time response of a flow field can be reconstructed from these DMD modes using

Equation (3.44). On the other hand, a good approximation of the flow dynamics can be obtained by using only the most dominant DMD modes in the reconstruction. In Figures 3.8 and 3.9, the flow dynamics is reconstructed using the mean flow and the first dynamic mode corresponding to the pitching frequency, i.e., $r = 3$ in Equation (3.44) for the one-mode reconstruction as the complex conjugate of each selected dynamic mode is also included in the reconstruction. Additionally, the first higher harmonic is included in the two-mode reconstruction ($r = 5$ in Equation (3.44)). The objective is to analyze the accuracy of the solution with respect to the number of modes included in the reconstruction.

For both the Euler and RANS approaches, the one-mode solution provides a very good approximation of the corresponding unsteady aerodynamic lift and moment coefficients c_l and c_m. Although a single mode already provides a relatively good prediction of the shock motion, including the second mode visibly improves the results.

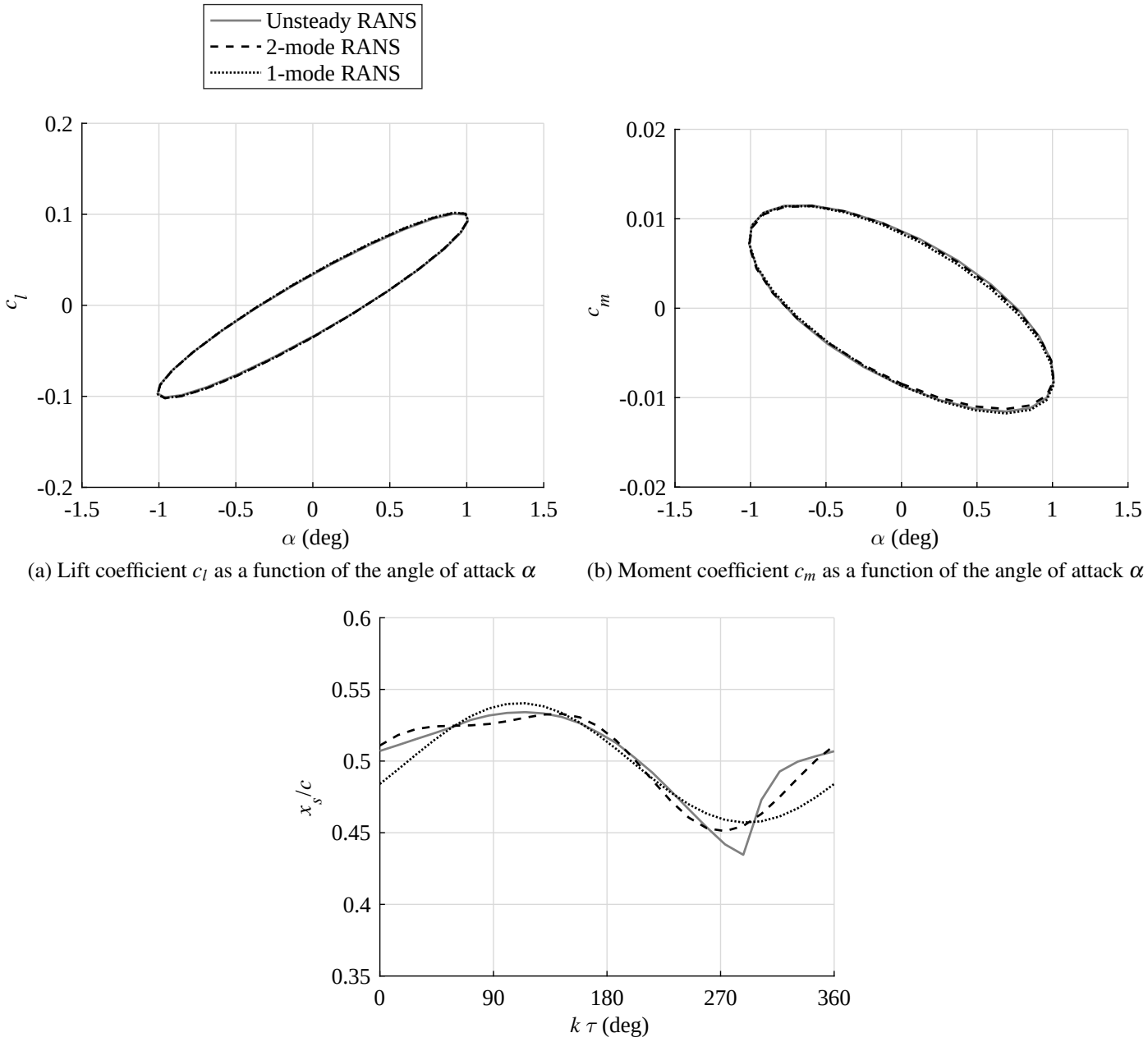

(a) Lift coefficient c_l as a function of the angle of attack α

(b) Moment coefficient c_m as a function of the angle of attack α

(c) Chordwise position of the shock on the upper surface x_s over one oscillation cycle

Figure 3.8: Comparison between the unsteady RANS solutions, the two-mode and one-mode DMD representations for the pitching NACA 64A010 case at the reduced frequency $k = 0.202$.

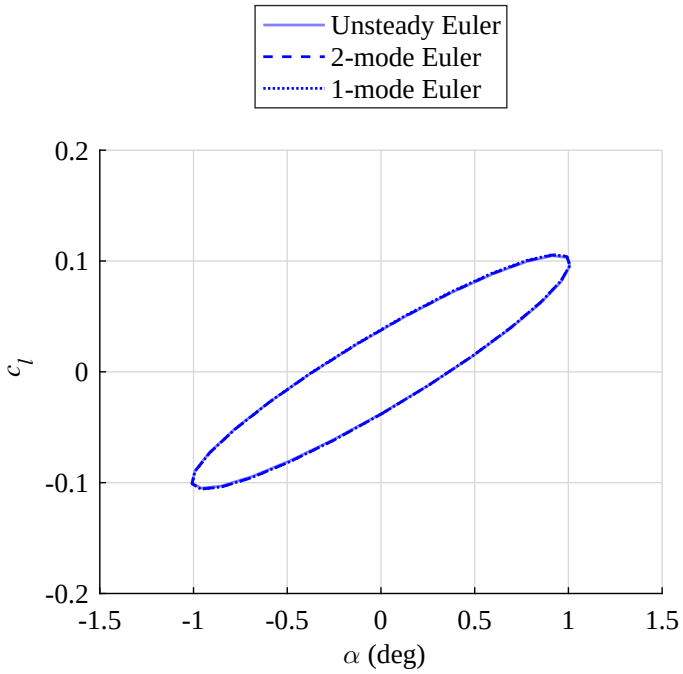

(a) Lift coefficient c_l as a function of the angle of attack α

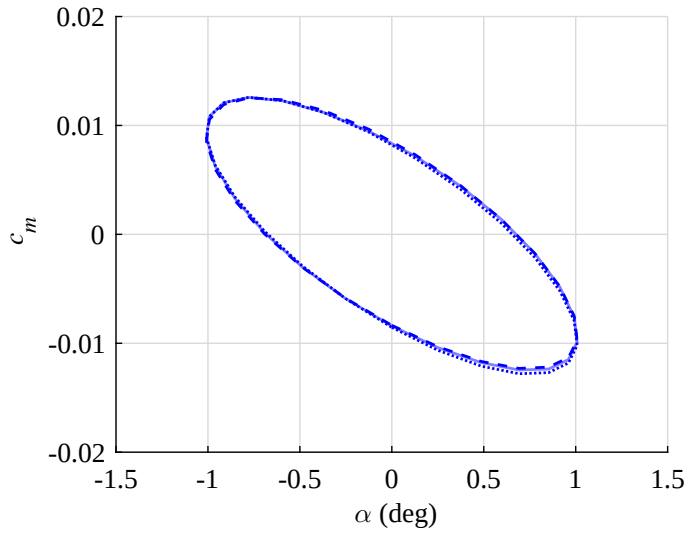

(b) Moment coefficient c_m as a function of the angle of attack α

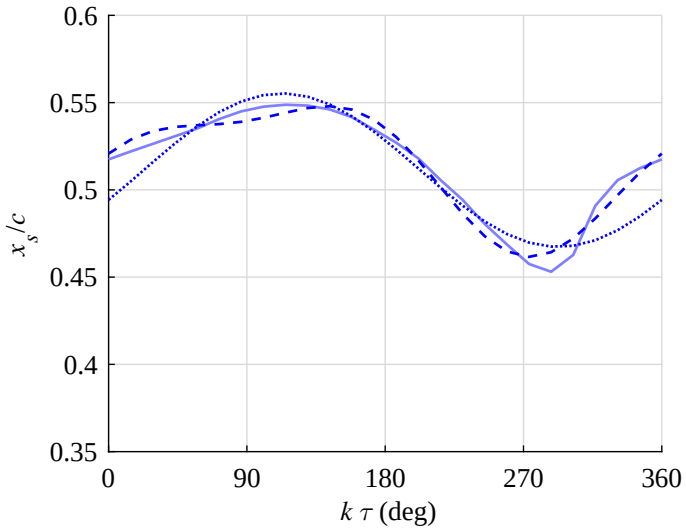

(c) Chordwise position of the shock on the upper surface x_s over one oscillation cycle

Figure 3.9: Comparison between the unsteady Euler solutions, the two-mode and one-mode DMD representations for the pitching NACA 64A010 case at the reduced frequency $k = 0.202$.

The harmonic balance method is suggested as an efficient alternative for calculating dynamic modes. The transonic flow around the pitching airfoil is simulated with the harmonic balance method using only the fundamental frequency of the flow, which is assumed to be equal to the imposed pitching frequency. Another simulation is carried out by adding the second harmonic. As discussed previously, the DMD modes appear at the frequency of oscillation and its harmonics, exactly as in the case of a harmonic balance procedure. Therefore, a harmonic balance solution with only the fundamental frequency corresponds to a single-mode DMD representation as illustrated in Figure 3.10a for the shock motion. If the second harmonic is included, the solution corresponds to a two-mode DMD representation as shown in Figure 3.10b.

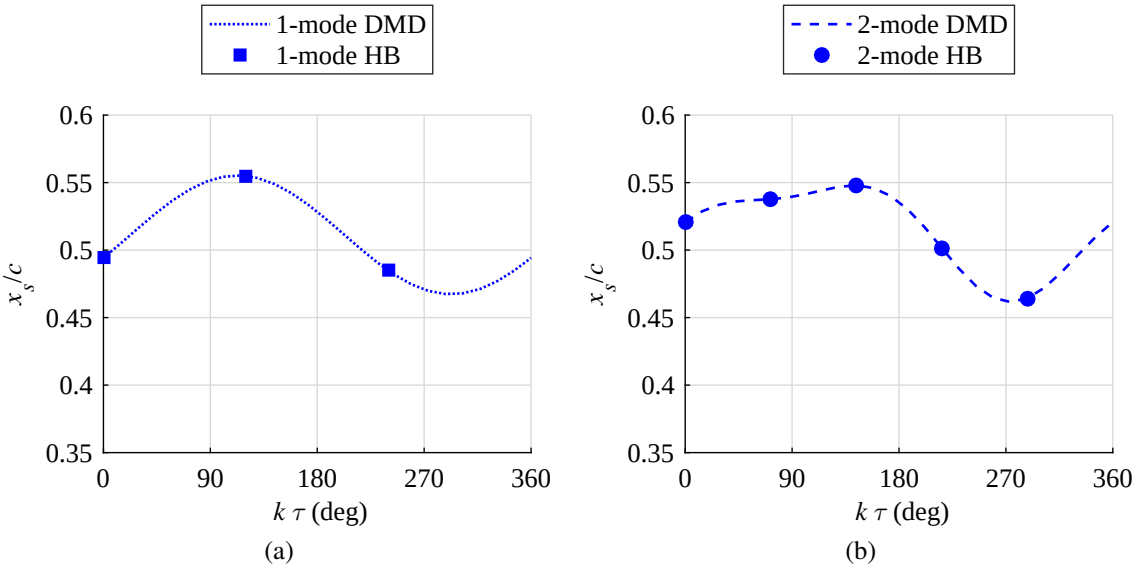

Figure 3.10: Comparison between the one-mode and two-mode DMD representations of the shock motion and the corresponding harmonic balance solutions for the pitching NACA 64A010 case at the reduced frequency $k = 0.202$.

On the same number of cores, an unsteady RANS calculation requires about ten times more runtime than an unsteady Euler calculation as shown in Table 3.2. A harmonic balance calculation using only the fundamental frequency involves three coupled steady-state calculations and requires half the computational time of the corresponding unsteady simulation for the present case. The computation time of a harmonic balance calculation using two input frequencies (five coupled steady-state calculations) is comparable to an unsteady simulation. If the number of included frequencies increases, the estimations are more accurate, but the HB method can become expensive in terms of memory requirements and computation time. In general, a harmonic balance simulation has a lower computation time than a time-accurate simulation because the flow transients are not considered. However, the flow transients smooth out rather quickly for the present

small-amplitude pitching airfoil.

Level of fidelity	Computation time (min on 8 cores)
Unsteady RANS	118.76
HB 2 RANS	120.10
HB 1 RANS	65.76
Unsteady Euler	12.38
HB 2 Euler	11.14
HB 1 Euler	6.18

Table 3.2: Computation time of the different levels of fidelity for the pitching NACA 64A010 case.

3.2.2 Influence of the reduced frequency

The dependence of the flow dynamics on the pitching frequency is assessed by comparing the results for several reduced frequencies k at the same nominal flow conditions. The pressure field is analyzed first as it is directly related to the aerodynamic forces, but the methodology could be applied to any other quantity. More specifically, DMD is applied to pressure coefficient fields generated by unsteady Euler simulations for three reduced frequencies $k = 0.1$, 0.202 and 0.3. This range of reduced frequencies is considered because the flutter instability is generally encountered for k of the order of 0.1 in most transonic flutter problems of aircraft wings or control surfaces [6]. The amplitude of the first dynamic mode decreases as the reduced frequency increases, but the first dynamic mode still contributes most to the flow dynamics as can be seen in the amplitude distributions given in Figure 3.11.

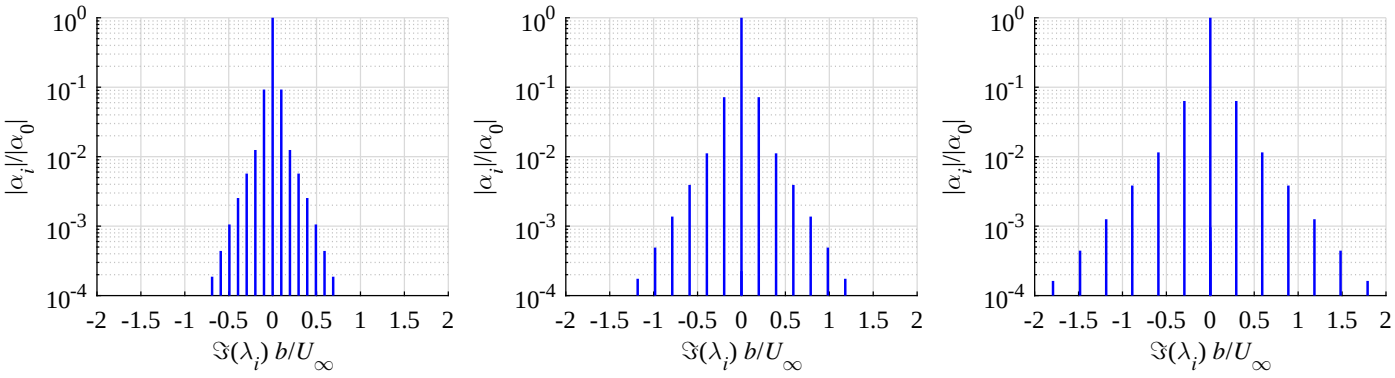

(a) $k = 0.1$ (b) $k = 0.202$ (c) $k = 0.3$

Figure 3.11: Absolute value of the modal amplitude $|\alpha_i|$ as a function of the modal reduced frequency $\Im(\lambda_i)b/U_\infty$ of the flow modes obtained by DMD of unsteady Euler pressure coefficient fields for the pitching NACA 64A010 case at three values of the reduced frequency k.

Figure 3.12 confirms that considering the first dynamic mode is sufficient to compute the time responses of the lift and moment coefficients, which are global quantities, for all selected values of k. Including the second dynamic mode does not really improve the results for c_l and c_m. On the other hand, it is more difficult to accurately capture a local quantity such as the shock wave motion, particularly at higher forcing reduced frequencies (e.g., $k = 0.3$). As the reduced frequency k increases, the shock wave motion starts to deviate from a simple harmonic solution. This observation is consistent with the amplitude distributions of Figure 3.11. The relative contribution of the higher dynamic modes becomes larger as k increases. The DMD reconstructions converge to the time-accurate solutions when the number of included modes increases. Figure 3.13 shows that at least three DMD modes are necessary to provide a relatively good approximation of the shock location at $k = 0.3$. Nonetheless, the accuracy of a flutter analysis depends mostly on the accuracy of the aerodynamic load prediction rather than the shock position itself. The above analysis thus shows that a relative good approximation can be obtained with a single dynamic mode.

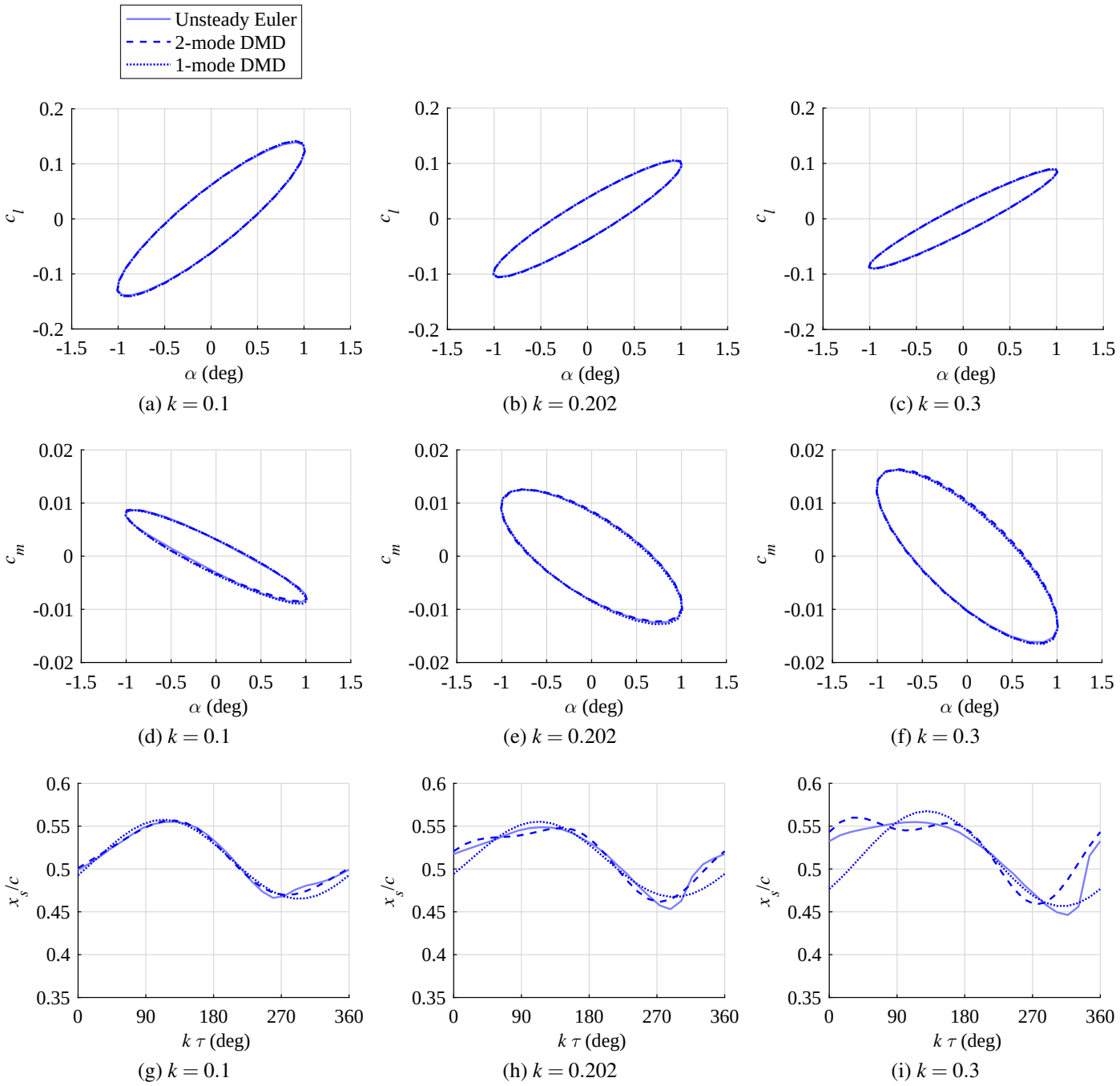

(a) $k = 0.1$ (b) $k = 0.202$ (c) $k = 0.3$

(d) $k = 0.1$ (e) $k = 0.202$ (f) $k = 0.3$

(g) $k = 0.1$ (h) $k = 0.202$ (i) $k = 0.3$

Figure 3.12: Comparison of the lift coefficient c_l, the moment coefficient c_m and the chordwise position of the shock on the upper surface x_s between the unsteady Euler solutions, the two-mode and one-mode DMD representations for the pitching NACA 64A010 case at three values of the reduced frequency k.

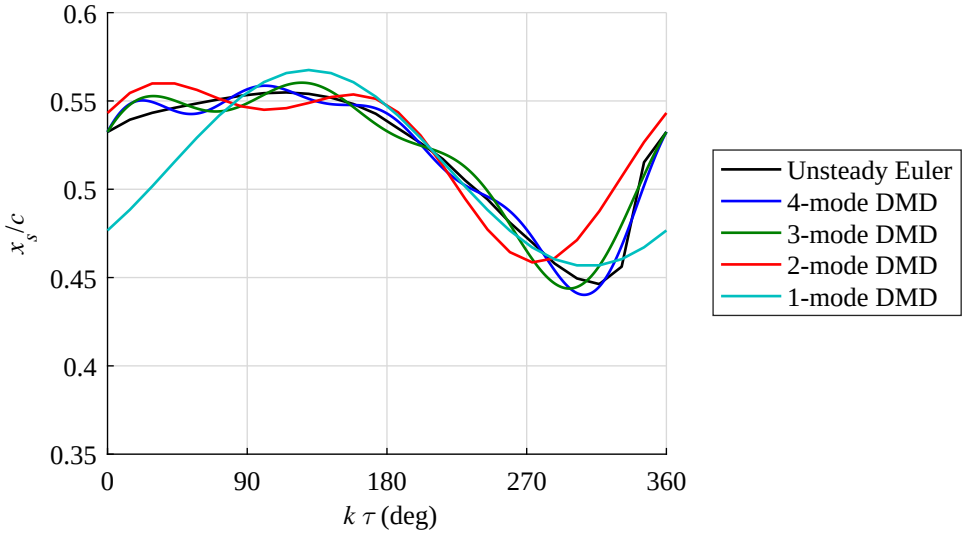

Figure 3.13: Comparison of the chordwise position of the shock on the upper surface x_s between the unsteady Euler solution and the DMD representations with different numbers of modes for the pitching NACA 64A010 case at the reduced frequency $k = 0.303$.

Figure 3.14 illustrates the shape $\alpha_0\boldsymbol{\phi}_0$ of DMD mode 0, i.e., the mean flow, as calculated from the three unsteady Euler simulations at $k = 0.1$, 0.202 and 0.3. It shows that the DMD representation of the mean flow remains essentially independent of the pitching reduced frequency k for such small-amplitude oscillations.

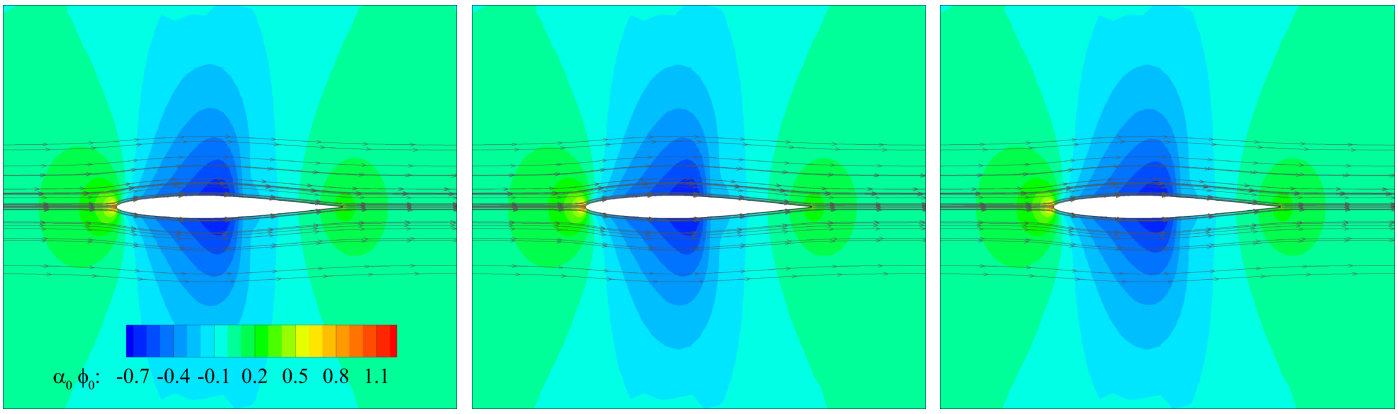

(a) $k = 0.1$ (b) $k = 0.202$ (c) $k = 0.3$

Figure 3.14: Influence of the reduced frequency k on the mean DMD mode $\alpha_0\boldsymbol{\phi}_0$ extracted from unsteady Euler flow fields for the pitching NACA 64A010 case. The filled contour plots represent the mean pressure mode, and the streamlines represent the mean velocity mode.

Each dynamic mode is characterized by a spatial structure oscillating at a single frequency $\Im(\lambda_i)$. The first dynamic mode shown in Figure 3.15 oscillates at the fundamental frequency (i.e., of the forced motion) and contains dynamically important structures.

Streamlines have been added to better visualize the mode shape, but one should keep in mind that these streamlines are not physical as the mean flow is not taken into account. It can be seen that the shape of the first dynamic mode changes progressively as k increases. The modal assurance criterion (MAC) is used in order to quantitatively demonstrate this observation. The MAC is a technique used to compare mode shapes [81]. Considering two different spatial modes $\boldsymbol{\phi}_A$ and $\boldsymbol{\phi}_B$, the MAC between these modes is calculated from

$$\mathrm{MAC}\left(\boldsymbol{\phi}_A, \boldsymbol{\phi}_B\right) = \left(\frac{\boldsymbol{\phi}_A^T \boldsymbol{\phi}_B}{\|\boldsymbol{\phi}_A\| \, \|\boldsymbol{\phi}_B\|} \right)^2 . \tag{3.60}$$

By definition, the MAC is bounded between 0 and 1. If MAC is equal to 1, then the correlation is perfect; if MAC = 0, then the two modes are fully uncorrelated.

The MAC matrices shown in Figure 3.15 quantitatively confirm that the shape of the first dynamic mode changes progressively with k. Moreover, the correlation becomes weaker as the reduced frequencies are further apart. As a result, the dynamics of the flow in time will change with k, and thus also the time response of the shock waves, which can profoundly affect the aeroelastic stability. It is therefore important to take into account this gradual transformation of the mode shape with frequency. These findings are also valid for the RANS results (not shown).

In summary, DMD of unsteady Euler or RANS simulations has shown that only a few modes are important to capture the dynamical behavior of the transonic flow when the small amplitude periodic motion is forced. The first dynamic mode, i.e., that corresponding to the frequency of the imposed motion, is sufficient to accurately estimate the lift and moment coefficients. Furthermore, the mode shapes change with the forcing frequency. This dependence on k must be captured for accurate flutter predictions.

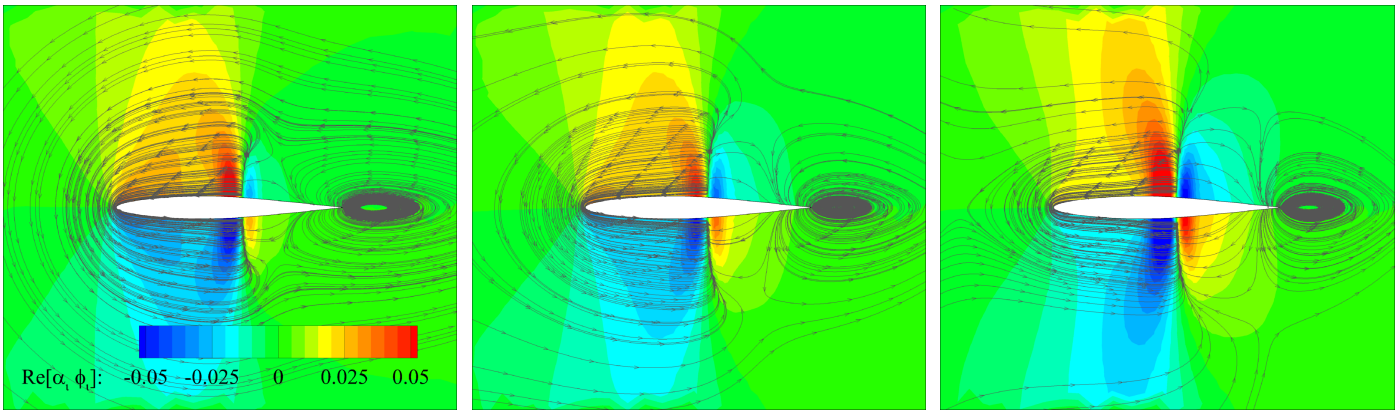

(a) $k = 0.1$ (b) $k = 0.202$ (c) $k = 0.3$

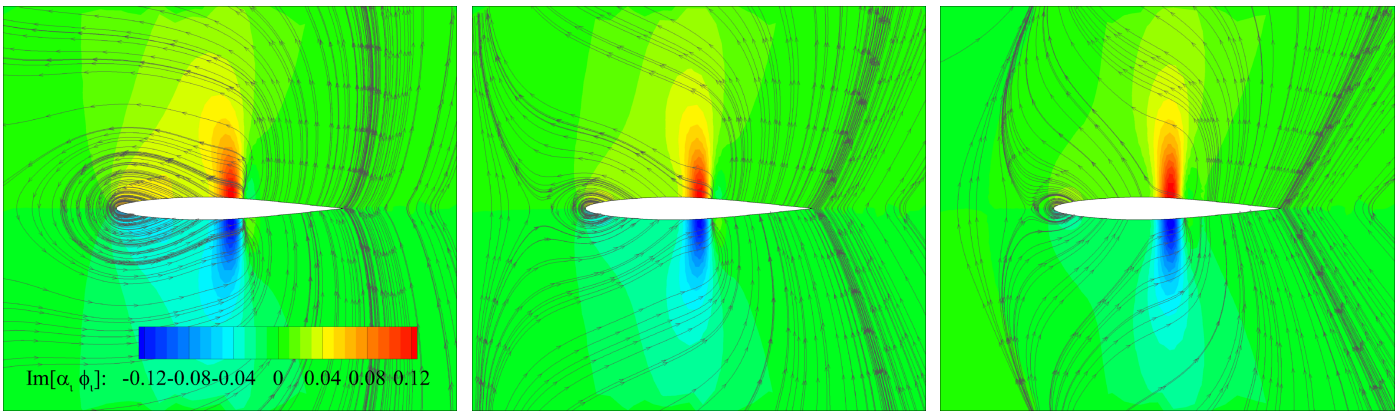

(d) $k = 0.1$ (e) $k = 0.202$ (f) $k = 0.3$

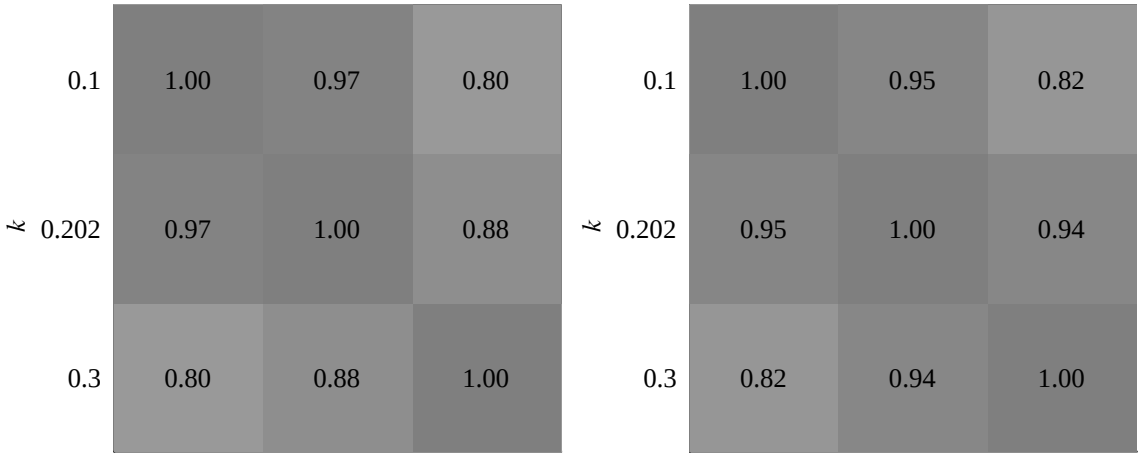

(g) (h)

Figure 3.15: Influence of the reduced frequency k on (a–c) the real part and (d–f) the imaginary part of the first dynamic mode $\alpha_1 \boldsymbol{\phi}_1$ extracted from unsteady Euler flow fields for the pitching NACA 64A010 case. The filled contour plots represent the first pressure mode, and the streamlines represent the first velocity mode. MAC matrices comparing (g) the real part and (h) the imaginary part of the first dynamic velocity modes at three values of k.

3.2.3 Dynamic mode interpolation

DMD of an unsteady high-fidelity simulation provides the relevant modes for a given oscillation frequency. If a different value of k is required, then another corresponding Euler or RANS simulation must be carried out. This approach becomes computationally expensive if a large number of frequencies is required as in a flutter analysis. The idea of the DMI methodology is thus to compute the most dominant modes at two nearby reduced frequencies k_1 and k_2. Then, the dynamic modes corresponding to other frequencies are estimated through linear interpolation, which makes it possible to take into account the progressive changes in the mode shape with k at a limited cost:

$$\boldsymbol{\phi}_i(k) = \frac{\boldsymbol{\phi}_i(k_2) - \boldsymbol{\phi}_i(k_1)}{k_2 - k_1}(k - k_1) + \boldsymbol{\phi}_i(k_1). \tag{3.61}$$

Higher-order interpolations requiring more reference simulations could also be used to achieve higher accuracy, but at the expense of higher computational cost.

As an example, the first dynamic modes of the pressure and velocity fields at $k = 0.202$ are obtained through interpolation between the corresponding modes at $k = 0.1$ and 0.3. Figure 3.16 compares the real and imaginary parts of the shape $\alpha_1\boldsymbol{\phi}_1$ of mode 1 estimated by interpolation to the corresponding exact mode for both the pressure coefficient (contours) and the velocity (streamlines). It can be seen that dynamic mode interpolation gives a good approximation as the exact and interpolated mode shapes are similar. This is quantitatively confirmed by the corresponding MAC values which are very close to 1: $\mathrm{MAC} = 0.98$ for the real part and $\mathrm{MAC} = 0.99$ for the imaginary part.

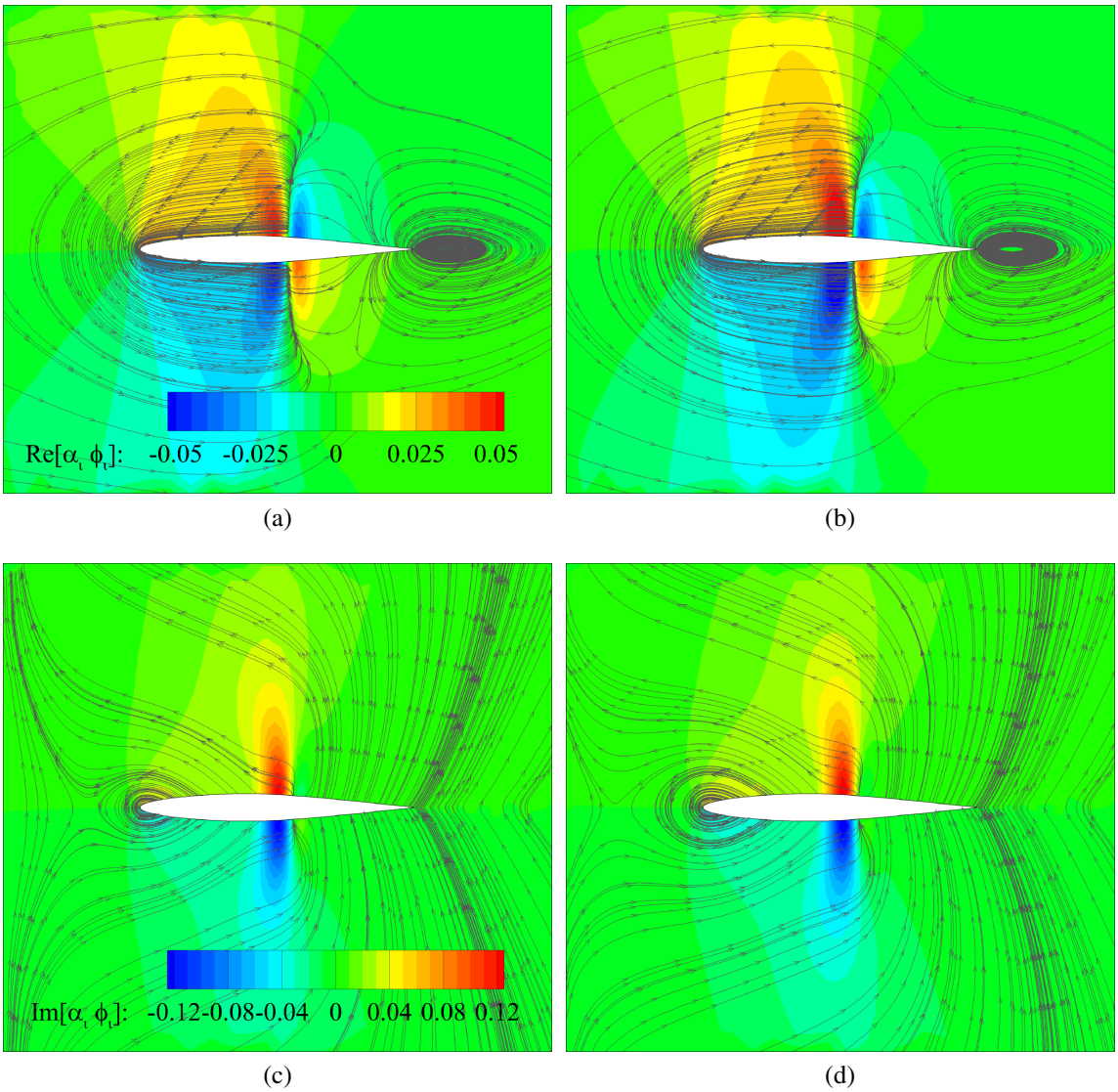

Figure 3.16: (a) Real part and (c) imaginary part of the first dynamic mode $\alpha_1 \boldsymbol{\phi}_1$ at $k = 0.202$ extracted from unsteady Euler flow fields for the pitching NACA 64A010 case. (b) Real part and (d) imaginary part of the first dynamic mode at $k = 0.202$ interpolated from the first dynamic modes at $k = 0.1$ and 0.3. The filled contour plots represent the first pressure mode, and the streamlines represent the first velocity mode.

The resulting one-mode solutions for the aerodynamic lift and moment coefficients and the shock location obtained from dynamic mode interpolation are in good agreement with the corresponding exact one-mode and unsteady solutions for both the Euler and RANS models, as illustrated in Figures 3.17 and 3.18. This dynamic mode interpolation can provide the aerodynamic loads for a range of reduced frequencies.

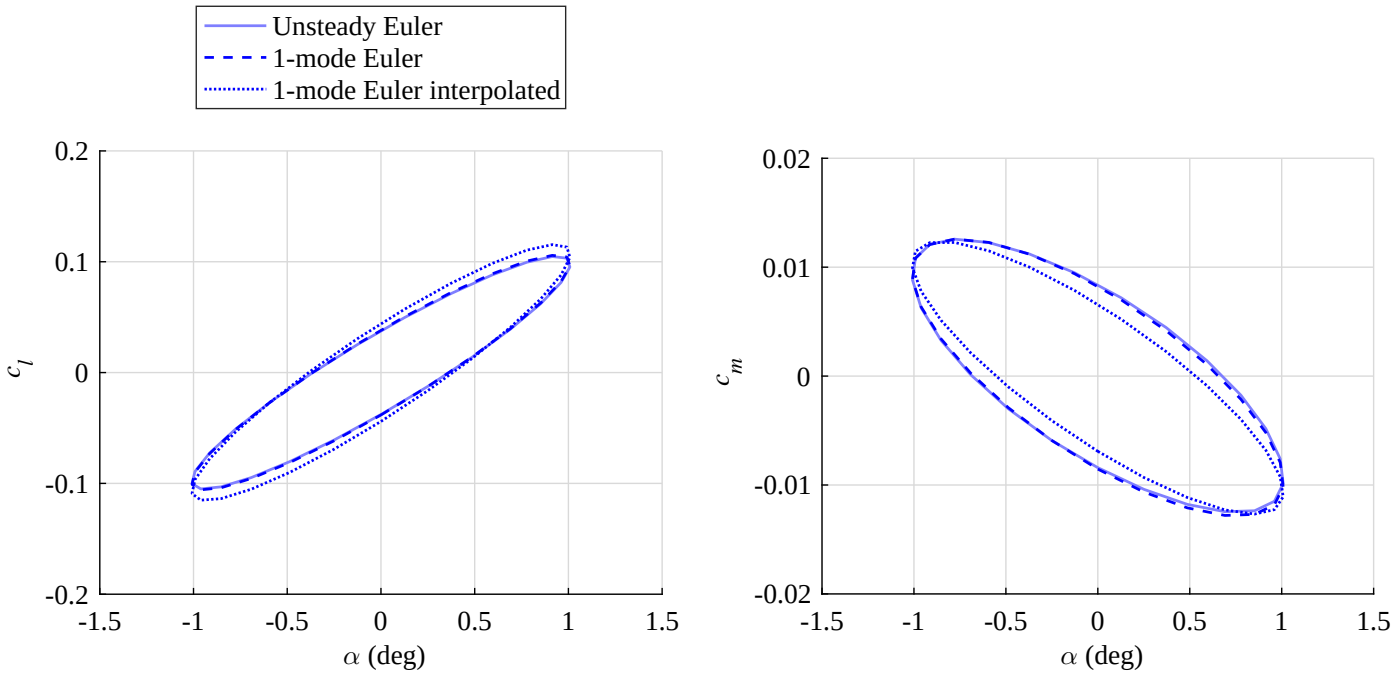

(a) Lift coefficient c_l as a function of the angle of attack α

(b) Moment coefficient c_m as a function of the angle of attack α

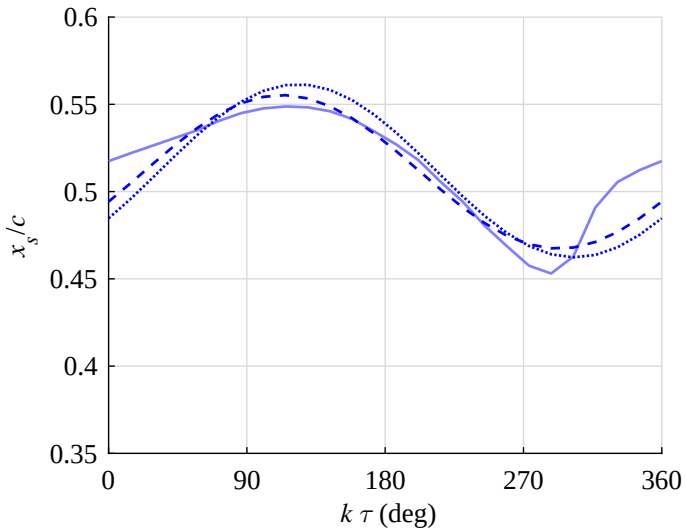

(c) Chordwise position of the shock on the upper surface x_s over one oscillation cycle

Figure 3.17: Comparison between the unsteady Euler solutions, the one-mode DMD representations and the present dynamic mode interpolation approach based on the first dynamic modes at $k = 0.1$ and 0.3 for the reference pitching NACA 64A010 case at the reduced frequency $k = 0.202$.

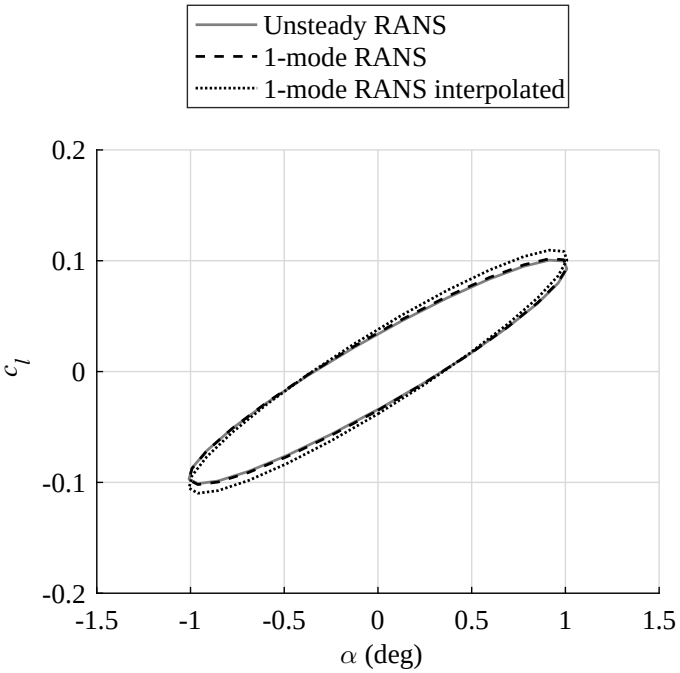

(a) Lift coefficient c_l as a function of the angle of attack α

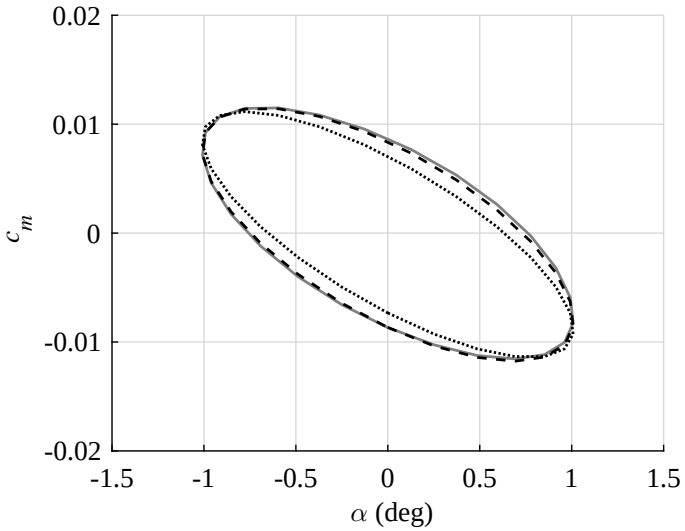

(b) Moment coefficient c_m as a function of the angle of attack α

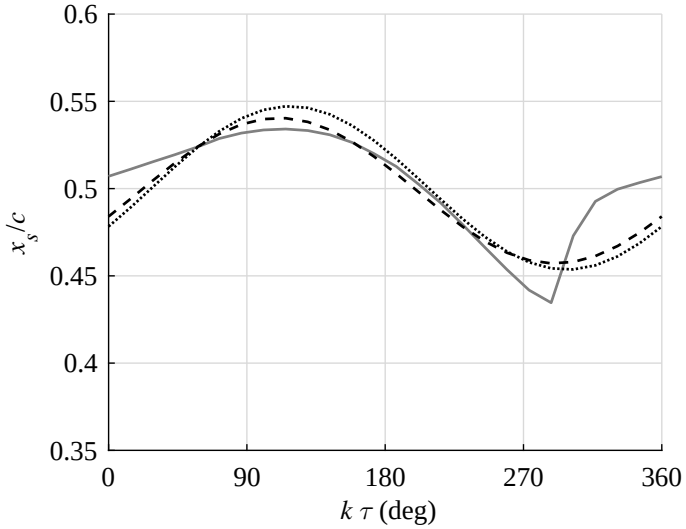

(c) Chordwise position of the shock on the upper surface x_s over one oscillation cycle

Figure 3.18: Comparison between the unsteady RANS solutions, the one-mode DMD representations and the present dynamic mode interpolation approach based on the first dynamic modes at $k = 0.1$ and 0.3 for the reference pitching NACA 64A010 case at the reduced frequency $k = 0.202$.

3.2.4 Influence of the motion amplitude

An amplitude of motion must be imposed for the reference unsteady simulations. Figure 3.19 analyzes the influence of the pitching amplitude $\hat{\alpha}$ on the amplitudes of the lift and moment coefficients $\hat{c}_l$ and $\hat{c}_m$. It can be seen that the values of $\hat{c}_l/\hat{\alpha}$ and $\hat{c}_m/\hat{\alpha}$ remain constant for small values of $\hat{\alpha}$, indicating a linear behavior. A departure from the linear behavior is observed for $\hat{\alpha} > 1$ deg. Therefore, as long as the amplitude of the motion remains small and massive flow separation does not occur, the aerodynamic forces can be scaled by the motion amplitude assuming a linear behavior. They become thus independent of the motion amplitude. This approximation is used for the flutter calculations presented in the next chapters.

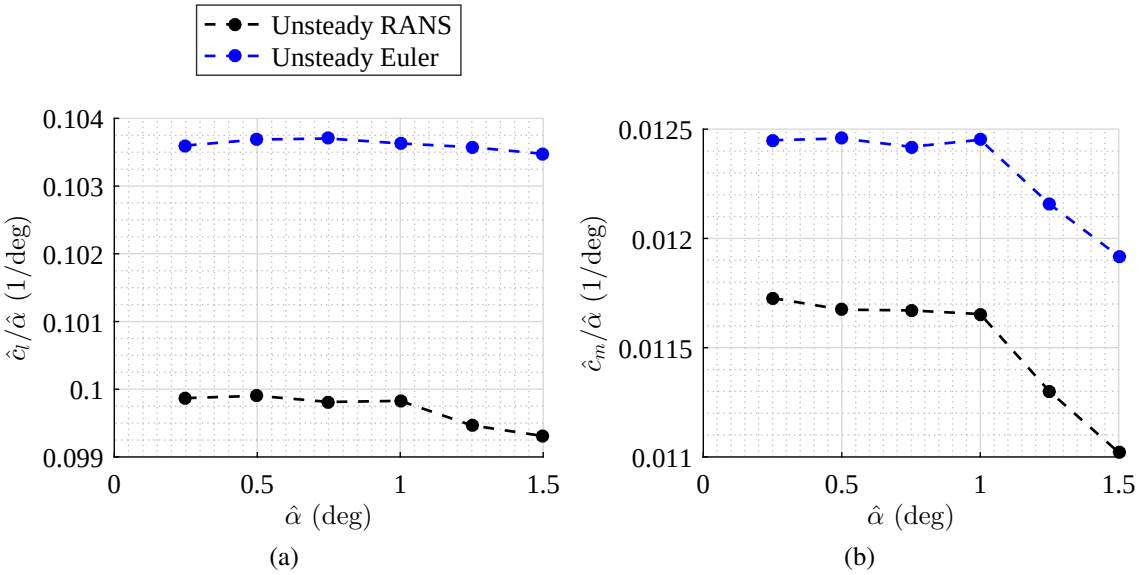

Figure 3.19: Influence of the amplitude of the pitching motion $\hat{\alpha}$ on the lift and moment coefficient amplitudes divided by the pitching amplitude, $\hat{c}_l/\hat{\alpha}$ and $\hat{c}_m/\hat{\alpha}$, for the reference pitching NACA 64A010 case at the reduced frequency $k = 0.202$.

3.3 Concluding remarks

The transonic flow around a pitching NACA 64A010 allowed the study of moving shock waves and has been used for validation purposes. The aerodynamic loads calculated at different levels of fidelity by both the Euler and RANS approaches are in good agreement with the experimental measurements of this high Reynolds number attached transonic flow.

The DMI methodology requires the most dominant dynamic modes of the flow response to small amplitude periodic oscillations of the structure for at least two frequencies. These dynamic modes can be extracted from unsteady flow fields by dynamic mode decomposition or computed directly by harmonic balance simulations. This chapter has shown that the first DMD mode contributes most to the flow dynamics so that the mean flow and first DMD mode are usually sufficient to represent the overall flow dynamics of the forced periodic motion. Moreover, the mode shapes progressively change with the frequency. The proposed unsteady aerodynamic model based on dynamic mode interpolation originates from these observations.

For small amplitude simple harmonic motions, interpolating from the most dominant modes at two nearby reference frequencies provides thus good estimates of the complete flow dynamics over a range of frequencies, provided that the frequency of interest is not too far from the range covered by the reference frequencies. From a computational point of view, only two unsteady simulations are required for each degree of freedom. In addition, a fully established periodic regime is quickly reached for the considered applications as they involve a forced motion, even for the 3D wings considered in the following chapters.

The DMI methodology has thus the ability to model the unsteady aerodynamic loads acting on wings oscillating in simple harmonic motion in the transonic flow regime. It is suitable for flutter analyses that involve small perturbations of the structure so that a linearization of the aerodynamic forces with respect to the deformation amplitude is possible. Chapter 4 presents several applications of the DMI methodology to transonic flutter calculations.

Chapter 4

Transonic flutter calculation methodology: description and validation

The unsteady aerodynamic modeling based on dynamic mode interpolation introduced in Chapter 3 can be used to obtain a frequency-domain aerodynamic force matrix. Aeroelastic stability analysis can then be performed using standard flutter solution techniques such as the *p-k* method.

This chapter presents the aeroelastic equations of motion used for flutter analysis. The computation of the aerodynamic force matrix using the DMI methodology is explained. The flutter solution techniques are then described. An important objective of this chapter is to validate the flutter solutions predicted using the DMI methodology by comparing with experimental measurements and time-accurate fluid-structure interaction simulations from the literature. The following key questions are investigated:

- What is the performance of the methodology for predicting the onset of transonic flutter for the 2D Isogai airfoil and 3D AGARD 445.6 wing models?
- What is the influence of the moving shock waves and the viscous boundary layer on the flutter boundary in the transonic flow regime?

4.1 Theoretical background

4.1.1 Derivation of the flutter equation

This section presents the derivation of the aeroelastic equations used for flutter analysis. The most general description of an aeroelastic system involves nonlinear governing equations for both the structural and fluid dynamics. In practice, an aeroelastic stability

analysis is generally carried out around a given wing shape (e.g., the flight shape in cruise) so that the equations governing the structural dynamics can be linearized around this wing shape for small deformations. The resulting aeroelastic equations in Cartesian coordinates are transformed to modal coordinates, which makes it possible to reduce the number of degrees of freedom of the system by retaining only a subset of the modes of vibration. A harmonic vibration of the structure is then assumed resulting in a frequency-domain formulation of the modal aeroelastic equations. The aerodynamic forces are assumed to vary linearly with the amplitude of the structural deformation for small amplitudes leading to the flutter equation, which corresponds to an eigenvalue problem for flutter analysis.

Flutter is a dynamic aeroelastic instability caused by the interaction of inertial, elastic and aerodynamic forces. After linearizing the equations governing the structural dynamics around a given wing shape assuming small deformations, the aeroelastic equations of motion for a N degrees-of-freedom system [3] can be expressed in matrix form as

$$\mathbf{M}\ddot{\mathbf{x}}(t) + \mathbf{C}\dot{\mathbf{x}}(t) + \mathbf{K}\mathbf{x}(t) = \mathbf{f}(t), \tag{4.1}$$

where $\mathbf{M}$ is the structural mass matrix, $\mathbf{C}$ is the structural damping matrix, $\mathbf{K}$ is the structural stiffness matrix, $\mathbf{x}$ is the vector of displacements at the nodes of the discrete system, and $\mathbf{f}$ is the vector of aerodynamic forces.

Undamped free vibration

The undamped free vibration of the discrete system is considered in order to determine the natural frequencies and the associated mode shapes. Neglecting the structural damping and aerodynamic forces in the aeroelastic equations of motion yields

$$\mathbf{M}\ddot{\mathbf{x}}(t) + \mathbf{K}\mathbf{x}(t) = \mathbf{0}. \tag{4.2}$$

The free vibration motion is expressed as

$$\mathbf{x}(t) = \hat{\mathbf{x}}\sin(\omega t), \tag{4.3}$$

where $\hat{\mathbf{x}}$ is the amplitude vector and ω is the free vibration frequency. Substituting this response into Equation (4.2) gives

$$\left(\mathbf{K} - \omega^2\mathbf{M}\right)\hat{\mathbf{x}} = \mathbf{0}. \tag{4.4}$$

The matrix $\left(\mathbf{K} - \omega^2\mathbf{M}\right)$ must be singular in order to obtain a non-trivial solution:

$$\det\left(\mathbf{K} - \omega^2\mathbf{M}\right) = 0. \tag{4.5}$$

The resulting Nth-order polynomial in ω^2 is solved to obtain the natural frequencies ω_j, $j \in \{1,2,3,\ldots,N\}$, at which the system oscillates in free vibration. There are as many natural frequencies as degrees of freedom in the discrete system. For each natural frequency ω_j, the corresponding normal mode $\hat{\mathbf{x}}_j$ is computed from

$$\left(\mathbf{K} - \omega_j^2 \mathbf{M}\right) \hat{\mathbf{x}}_j = \mathbf{0}, \qquad j \in \{1,2,3,\ldots,N\}. \tag{4.6}$$

Each mode shape defines the relative displacements of each node when the system oscillates at the associated natural frequency. A mode shape thus describes a characteristic shape and its amplitude depends on the chosen mode shape normalization. The modal matrix $\mathbf{\Phi}$ contains the N normal mode shapes of the discrete system:

$$\mathbf{\Phi} = \begin{bmatrix} \hat{\mathbf{x}}_1 & \hat{\mathbf{x}}_2 & \hat{\mathbf{x}}_3 & \ldots & \hat{\mathbf{x}}_N \end{bmatrix}. \tag{4.7}$$

Transformation to modal coordinates

The vector of displacements $\mathbf{x}$ is transformed to modal coordinates $\mathbf{q}$ using the modal matrix $\mathbf{\Phi}$:

$$\mathbf{x}(t) = \mathbf{\Phi}\mathbf{q}(t). \tag{4.8}$$

The modal coordinate $q_j(t)$ corresponds to the amplitude of the jth mode shape present in the motion at time t. The equations of motion can be expressed in a modal coordinate system by substituting Equation (4.8) into Equation (4.1) and pre-multiplying by the transpose of the modal matrix $\mathbf{\Phi}^\mathsf{T}$:

$$\mathbf{\Phi}^\mathsf{T}\mathbf{M}\mathbf{\Phi}\ddot{\mathbf{q}}(t) + \mathbf{\Phi}^\mathsf{T}\mathbf{C}\mathbf{\Phi}\dot{\mathbf{q}}(t) + \mathbf{\Phi}^\mathsf{T}\mathbf{K}\mathbf{\Phi}\mathbf{q}(t) = \mathbf{\Phi}^\mathsf{T}\mathbf{f}(t), \tag{4.9}$$

$$\mathbf{M}_q\ddot{\mathbf{q}}(t) + \mathbf{C}_q\dot{\mathbf{q}}(t) + \mathbf{K}_q\mathbf{q}(t) = \mathbf{f}_q(t), \tag{4.10}$$

where $\mathbf{M}_q = \mathbf{\Phi}^\mathsf{T}\mathbf{M}\mathbf{\Phi}$ is the modal mass matrix, $\mathbf{C}_q = \mathbf{\Phi}^\mathsf{T}\mathbf{C}\mathbf{\Phi}$ is the modal structural damping matrix, $\mathbf{K}_q = \mathbf{\Phi}^\mathsf{T}\mathbf{K}\mathbf{\Phi}$ is the modal stiffness matrix, and $\mathbf{f}_q(t) = \mathbf{\Phi}^\mathsf{T}\mathbf{f}(t)$ is the modal aerodynamic force vector. The values of $\mathbf{M}_q$, $\mathbf{C}_q$, $\mathbf{K}_q$ and $\mathbf{f}_q$ depend on the normalization chosen for the mode shapes. In this thesis, the mode shapes are normalized such that the modal mass matrix becomes the identity matrix. A mode shape can also be normalized so that its maximum value or its vector norm is equal to unity.

In general, the system has a large number of degrees of freedom. The number of modes of vibration included in the solution can be reduced because the frequency range of interest is usually limited in practical applications. The modal transformation can then

be approximated using only a subset of modes:

$$\mathbf{x}(t) \approx \mathbf{\Phi}_n \mathbf{q}_n(t), \tag{4.11}$$

with the reduced modal matrix $\mathbf{\Phi}_n = [\hat{\mathbf{x}}_1, \hat{\mathbf{x}}_2, \hat{\mathbf{x}}_3, \ldots, \hat{\mathbf{x}}_n]$, $n < N$, and the reduced set of modal coordinates $\mathbf{q}_n$. A system of N physical degrees of freedom can be analyzed by n modal equations.

Harmonic vibration

The assumption of a damped sinusoidal motion makes it possible to define the damping, which will control whether flutter occurs or not:

$$\mathbf{q}(t) = \hat{\mathbf{q}}\, \mathrm{e}^{p\frac{U_\infty}{L}t} = \hat{\mathbf{q}}\, \mathrm{e}^{p\tau}, \tag{4.12}$$

where $\hat{\mathbf{q}}$ is the amplitude, U_∞ is the airspeed, L is a reference length, and $\tau = tU_\infty/L$ is the non-dimensional time. The non-dimensional parameter p is defined such that

$$p = g + ik, \tag{4.13}$$

where i is the imaginary unit, $k = \omega L/U_\infty$ is the reduced frequency, ω is the oscillatory frequency, and $g = \gamma k$. The parameter γ is the true damping coefficient that defines a rate of decay:

$$\gamma = \frac{1}{2\pi} \ln\left(\frac{a_{i+1}}{a_i}\right), \tag{4.14}$$

where a_i and a_{i+1} correspond to the amplitudes of successive cycles. The value of γ is negative for a decaying system response in time ($a_{i+1} < a_i$), zero for a constant amplitude response ($a_{i+1} = a_i$) and positive for a growing response ($a_{i+1} > a_i$).

Amplitude linearization

The aerodynamic forces are assumed to vary linearly with the amplitude of the structural deformation for sufficiently small values of the amplitude:

$$\mathbf{f}_q(t) = \frac{1}{2}\rho_\infty U_\infty^2 \mathbf{Q}(p)\hat{\mathbf{q}}\, \mathrm{e}^{p\tau}, \tag{4.15}$$

where ρ_∞ is the free-stream air density, $q_\infty = \frac{1}{2}\rho_\infty U_\infty^2$ is the dynamic pressure, and $\mathbf{Q}(p)$ is the complex modal aerodynamic force matrix for a harmonic motion of reduced frequency $\Im(p) = k$ and damping characterized by $\Re(p) = g$. The general form of the flutter equation

can be obtained by introducing Equations (4.12) and (4.15) into Equation (4.10):

$$\left[\frac{U_\infty^2}{L^2}\mathbf{M}_q p^2 + \frac{U_\infty}{L}\mathbf{C}_q p + \mathbf{K}_q - \frac{1}{2}\rho_\infty U_\infty^2 \mathbf{Q}(p)\right]\hat{\mathbf{q}} = \mathbf{0}. \tag{4.16}$$

Most of the available unsteady aerodynamic methods (e.g., the doublet lattice approach) calculate the modal aerodynamic force matrix $\mathbf{Q}$ in the frequency domain for undamped simple harmonic motion. The following section explains how this matrix $\mathbf{Q}$ can be computed using the DMI methodology.

4.1.2 Computation of the modal aerodynamic force matrix using the DMI methodology

Figure 4.1 illustrates the main steps of the entire methodology for transonic flutter calculations that captures the shock motion and can also take into account the shock-boundary layer interaction. The goal here is to obtain the modal aerodynamic force matrix $\mathbf{Q}$ as a function of the reduced frequency k:

- The first step consists in choosing a structural model built using any finite element (FE) code such as Metafor [82] or MSC Nastran [83]. The FE model can be very detailed such as an actual aircraft composite wing. A configuration is then chosen and the structural model is linearized around it. The mass matrix $\mathbf{M}$, the stiffness matrix $\mathbf{K}$ and the resulting modal matrix $\mathbf{\Phi}$ and modal frequencies are obtained from the FE model. There is no interaction with the solid solver once the modal parameters have been extracted. Note that simpler structural models can also be used (e.g., solid body oscillators).

- The structural modes appearing at high frequencies are discarded because their impact on the aeroelastic stability is generally not critical. The relevant structural modes that are selected are then used to impose the motion of the wing in the unsteady Euler or RANS simulations. If the geometry of the structural model is different from the wing skin used in the CFD simulations, an interpolation technique is necessary to obtain the modal displacements on the external surface of the wing. In this chapter, the geometry of the structure is the same as the geometry used for the CFD simulations so that even a bilinear interpolation can be used to obtain the structural displacements on the nodes of the CFD grid. In industry, structural engineers generally model only the internal structure of the wing. Chapter 5 will introduce the infinite plate spline (IPS) method to transfer the displacements computed in an internal load-carrying component to the external skin of the wing.

- For a given free-stream Mach number M_∞ and Reynolds number Re, unsteady Euler

or RANS simulations are carried out sequentially, in which the motion of the wing is imposed based on each selected structural mode for at least two different reduced frequencies. A small value of the motion amplitude is chosen so that the aerodynamic forces can be scaled by the motion amplitude assuming a linear behavior as mentioned in Section 3.2.4. A simple harmonic motion is imposed for each mode considered. The forcing reduced frequencies are chosen knowing that transonic flutter typically appears at reduced frequencies of the order of 0.1 in practical transonic flutter problems involving aircraft wings or control surfaces [6].

- The unsteady flow fields obtained for the reference reduced frequencies and each structural mode are then processed using dynamic mode decomposition in order to extract the dominant flow modes. These dominant flow modes are typically those corresponding to the frequency that has been imposed in the simulation. More specifically, DMD is applied to the surface pressure fields over one period. About 25 snapshots equidistant in time are used. Note that the dominant flow modes could also be directly obtained by harmonic balance simulations.

- The dominant flow modes are then interpolated to take into account the progressive modification of the mode shape with the reduced frequency and to accurately estimate the flow dynamics for a range of k. The frequency-domain modal aerodynamic force matrix $\mathbf{Q}(ik)$ can then be computed using the principle of virtual work, as explained in Dimitriadis [84, 85]:

$$\mathbf{Q}(ik) = \mathbf{W}^{\intercal}\mathbf{N}(ik), \tag{4.17}$$

  where $\mathbf{W}$ is the modal matrix that contains the modal displacements of each cell center of the CFD mesh on the wing surface, which are interpolated from the discrete structural model. The size of matrix $\mathbf{W}$ is $N_c \times n$ where N_c is the number of cells on the CFD surface mesh and n is the number of retained modes. $\mathbf{N}(ik)$ is a $N_c \times n$ matrix that contains the aerodynamic normal forces acting on the cells of the CFD surface mesh due to imposed modal deformations of the wing specified by the matrix $\mathbf{W}$ (e.g., the first column of $\mathbf{N}(ik)$ corresponds to the contribution due to the first mode shape). The aerodynamic normal force contribution of each cell of the CFD surface mesh is computed by integrating the pressure over the corresponding cell area.

- The flutter point can be computed by either the p-k or g method. These methods are described below.

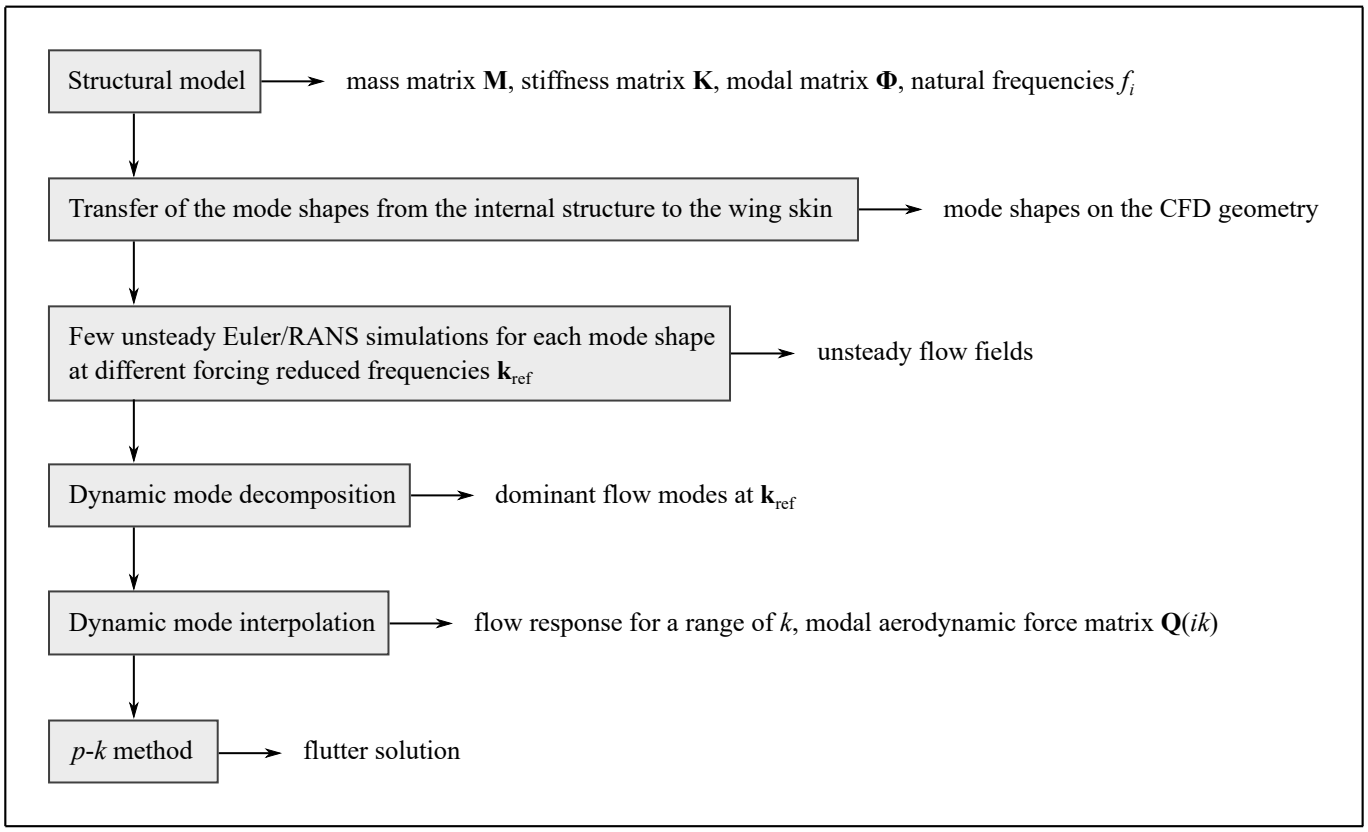

Figure 4.1: Overview of the main steps of the DMI-based aeroelastic methodology.

4.1.3 Flutter solution methods

The typical flutter solution methods are explained starting from the traditional *p-k* method and then the *g* and modified *p-k* methods.

p-k method

The *p-k* method [3, 54] is an approximate method to determine a rate-of-decay solution of the flutter equation. It assumes that the modal aerodynamic force matrix in the flutter equation given in Equation (4.16) is only available for undamped simple harmonic motion, i.e., $\mathbf{Q}(p) \approx \mathbf{Q}(ik)$:

$$\left[\frac{U_\infty^2}{L^2}\mathbf{M}_q p^2 + \frac{U_\infty}{L}\mathbf{C}_q p + \mathbf{K}_q - \frac{1}{2}\rho_\infty U_\infty^2 \mathbf{Q}(ik)\right]\hat{\mathbf{q}} = \mathbf{0}. \tag{4.18}$$

This assumption is valid only at the flutter condition, where the damping is zero and the system vibrates with a constant amplitude. However, the *p-k* method generally provides

good approximations of the true damping for aeroelastic responses with slowly decreasing (or increasing) amplitudes [54].

For a given free-stream Mach number M_∞ and dynamic pressure $1/2\rho_\infty U_\infty$ and for each individual mode of vibration, the *p-k* method is applied according to the following steps:

- An initial guess for the frequency ω of the mode is chosen (e.g., the wind-off frequency or the frequency obtained for a previous airspeed). The reduced frequency is calculated knowing the frequency and the velocity: $k = \omega L/U_\infty$.
- The aerodynamic force matrix is computed for the current reduced frequency.
- Equation (4.18) corresponds to a quadratic eigenvalue problem involving modal mass, modal damping and modal stiffness matrices. This quadratic eigenvalue problem is solved for the system eigenvalues p at a given combination of density ρ_∞ and velocity U_∞ using one of the numerical methods explained in Tisseur and Meerbergen [86]. The frequencies of the system at this flight condition are then determined using Equation (4.13): $k = \Im(p)$.
- The frequency of the system closest to the initial guess is chosen and the procedure is repeated until the frequency converges for the considered structural mode. The corresponding damping coefficient is then obtained from Equation (4.13): $\gamma = \Re(p)/k$.

This iterative procedure is repeated for each structural mode of interest and for different free-stream velocities.

Note that imposing the flight Mach number M_∞ and choosing a free-stream velocity U_∞ at each iteration still leaves one additional degree of freedom. In particular, the free-stream density ρ_∞ in Equation (4.18) is still undetermined, and an additional constraint is required to set it:

- For a **matched** flutter solution, a standard atmosphere (ISA) is assumed. This relates the density to the temperature, which is itself computed from the speed of sound, knowing velocity and Mach number. Such flutter calculations are carried out in Chapter 5 for the Embraer benchmark wing.
- For an **unmatched** flutter solution, the density is usually kept constant. Such flutter calculations are performed in Chapter 4 for the Isogai and AGARD test cases.

g-method

The *g*-method adds a first-order damping term to Equation (4.18) of the *p-k* method in order to better approximate the true damping of the aeroelastic system over the entire

velocity range of interest. The following expression for the modal aerodynamic force matrix is derived for small g by using a damping perturbation method [87]:

$$\mathbf{Q}(p) \approx \mathbf{Q}(ik) + g\mathbf{Q}'(ik), \tag{4.19}$$

where $\mathbf{Q}'(ik)$ denotes the derivative of $\mathbf{Q}(ik)$ with respect to k, which can be calculated by a central differencing scheme. The g-method equation is obtained by substituting Equation (4.19) into the flutter equation given in Equation (4.16):

$$\left[\frac{U_\infty^2}{L^2}\mathbf{M}_q p^2 + \frac{U_\infty}{L}\mathbf{C}_q p + \mathbf{K}_q - \frac{1}{2}\rho_\infty U_\infty^2 \mathbf{Q}'(ik)g - \frac{1}{2}\rho_\infty U_\infty^2 \mathbf{Q}(ik)\right]\hat{\mathbf{q}} = \mathbf{0}. \tag{4.20}$$

The solution algorithm consists first in substituting the expression of p given in Equation (4.13) into Equation (4.20) to obtain a second-order system in terms of g:

$$\left[\mathbf{A}_2 g^2 + \mathbf{A}_1 g + \mathbf{A}_0\right]\hat{\mathbf{q}} = \mathbf{0}, \tag{4.21}$$

where

$$\mathbf{A}_2 = \frac{U_\infty^2}{L^2}\mathbf{M}_q, \tag{4.22}$$

$$\mathbf{A}_1 = 2ik\frac{U_\infty^2}{L^2}\mathbf{M}_q + \frac{U_\infty}{L}\mathbf{C}_q - \frac{1}{2}\rho_\infty U_\infty^2 \mathbf{Q}'(ik), \tag{4.23}$$

$$\mathbf{A}_0 = -k^2\frac{U_\infty^2}{L^2}\mathbf{M}_q + ik\frac{U_\infty}{L}\mathbf{C}_q + \mathbf{K}_q - \frac{1}{2}\rho_\infty U_\infty^2 \mathbf{Q}(ik). \tag{4.24}$$

The solutions of Equation (4.21) exist when $\Im(g) = 0$ because g is a real parameter by definition. A reduced frequency sweep technique is used to search for this condition. More precisely, the quadratic eigenvalue problem given in Equation (4.21) is solved for the eigenvalues g starting from a minimum reduced frequency k and gradually increasing k by Δk the imaginary part of the eigenvalues changes sign. The reduced frequency at which the condition $\Im(g) = 0$ is satisfied can then be determined by interpolation. The resulting damping coefficient and frequency are then obtained using the definitions of g and k:

$$\gamma = \frac{\Re(g)}{k}, \tag{4.25}$$

$$\omega = k\frac{U_\infty}{L}. \tag{4.26}$$

At the flutter condition (zero damping), both the p-k and g methods reduce to the same equation. Indeed, setting $g = 0$ in Equation (4.20) of the g-method results in Equation (4.18) of the p-k method.

Modified *p-k* method

Rodden et al. [88] also proposed to add an aerodynamic damping term to Equation (4.18) of the *p-k* method for more reliable damping prediction. The modified *p-k* method equation is given by

$$\left[\frac{U_\infty^2}{L^2}\mathbf{M}_q p^2 + \frac{U_\infty}{L}\mathbf{C}_q p + \mathbf{K}_q - \frac{1}{2}\rho_\infty U_\infty^2 \frac{\Im(\mathbf{Q}(ik))}{k} g - \frac{1}{2}\rho_\infty U_\infty^2 \mathbf{Q}(ik)\right]\hat{\mathbf{q}} = \mathbf{0}, \tag{4.27}$$

which reduces to the original formulation given in Equation (4.18) at the flutter point where $g = 0$. Introducing $\mathbf{Q}(ik) = \Re(\mathbf{Q}(ik)) + i\Im(\mathbf{Q}(ik))$ into Equation (4.27) yields

$$\left[\frac{U_\infty^2}{L^2}\mathbf{M}_q p^2 + \left(\frac{U_\infty}{L}\mathbf{C}_q - \frac{1}{2}\rho_\infty U_\infty^2 \frac{\Im(\mathbf{Q}(ik))}{k}\right) p + \mathbf{K}_q - \frac{1}{2}\rho_\infty U_\infty^2 \Re(\mathbf{Q}(ik))\right]\hat{\mathbf{q}} = \mathbf{0}. \tag{4.28}$$

Equation (4.28) highlights that the real part of $\mathbf{Q}$ is in phase with the harmonic vibration and corresponds to the aerodynamic stiffness, while the imaginary part of $\mathbf{Q}$ is in phase with the vibration velocity and represents the aerodynamic damping. The solution procedure for the modified *p-k* method is the same as for the original *p-k* method.

4.2 Isogai wing section

In this section, the proposed methodology is used to analyze the aeroelastic stability of the two-dimensional Isogai wing validation case. The accuracy of the methodology is assessed by comparing with results available in the literature.

4.2.1 Structural model

As illustrated in Figure 4.2, the Isogai wing section aeroelastic model (case A) [89, 90] consists of a 2D airfoil with two degrees of freedom; it can undergo a combination of pitching α and plunging h motions. The geometry is a NACA 64A010 airfoil with chord $c = 2b$, which is the same symmetric airfoil as for the pitching airfoil studied in Section 3.2. The pitch degree of freedom is defined positive nose up and the plunge degree of freedom is positive downwards. The aeroelastic equations of motion for this system can be expressed in terms of mixed coordinates (i.e., translational and rotational coordinates) and have the same general form as in Equation (4.1):

$$\underbrace{\begin{bmatrix} m_a & S \\ S & I_\alpha \end{bmatrix}}_{\mathbf{M}} \begin{bmatrix} \ddot{h}(t) \\ \ddot{\alpha}(t) \end{bmatrix} + \underbrace{\begin{bmatrix} C_h & 0 \\ 0 & C_\alpha \end{bmatrix}}_{\mathbf{C}} \begin{bmatrix} \dot{h}(t) \\ \dot{\alpha}(t) \end{bmatrix} + \underbrace{\begin{bmatrix} K_h & 0 \\ 0 & K_\alpha \end{bmatrix}}_{\mathbf{K}} \underbrace{\begin{bmatrix} h(t) \\ \alpha(t) \end{bmatrix}}_{\mathbf{q}} = \begin{bmatrix} -l(t) \\ m(t) \end{bmatrix}, \tag{4.29}$$

where l is the aerodynamic lift (positive upwards) and m is the aerodynamic moment with respect to the elastic axis (positive nose up). All the structural parameters shown in Figure 4.2, in which the mass, damping and stiffness matrices directly depend, are taken from Alonso and Jameson [91] and Isogai [89]. These parameters were chosen empirically to represent the dynamics of an outboard section of a sweptback wing in the transonic flow regime. The airfoil mass m_a is computed from the airfoil mass ratio $\mu = m_a/(\pi\rho_\infty b^2) = 60$ where ρ_∞ is the free-stream air density. The static unbalance is given by $S_\alpha = m_a b x_\alpha$ with $x_\alpha = 1.8$. The moment of inertia of the airfoil around the elastic axis is $I_\alpha = m_a b^2 r_\alpha^2$ with $r_\alpha^2 = 3.48$. The damping coefficients for the plunging and pitching modes C_h and C_α are zero. The stiffness associated with the plunging mode is $K_h = m_a \omega_h^2$ with the uncoupled natural frequency of the section in plunge $\omega_h = 100\,\mathrm{rad/s}$. The stiffness of the pitching mode is $K_\alpha = I_\alpha \omega_\alpha^2$ with the uncoupled natural frequency of the pitching mode $\omega_\alpha = 100\,\mathrm{rad/s}$. The parameter a defines the non-dimensional location of the elastic axis: $a = 0$ corresponds to the midchord and $a = -1$ to the leading edge of the airfoil. In the Isogai case, $a = -2$ so that the point of rotation lies ahead of the leading edge. On the other hand, the aerodynamic forces depend on the dynamics of the airfoil and are not explicitly known because of the nonlinearity of the problem.

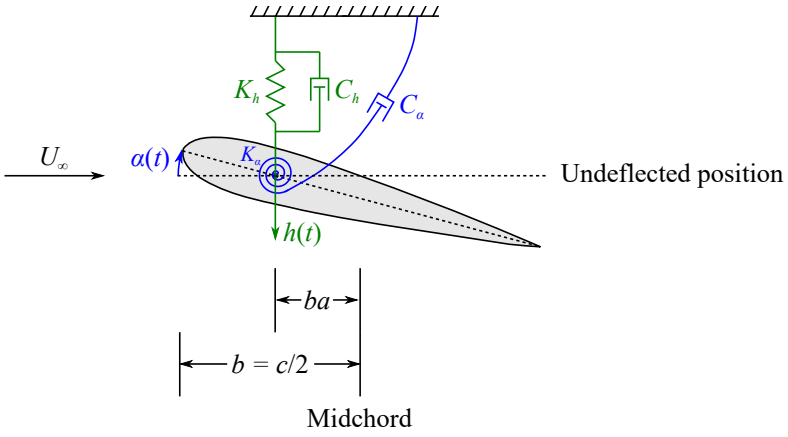

Figure 4.2: Typical two-degree-of-freedom wing section model. (Adapted from Alonso and Jameson [91].)

4.2.2 Computation of the aerodynamic force matrix

The dynamic mode interpolation approach is used to model the fluid flow, and more specifically the aerodynamic forces. For a sinusoidal motion, Chapter 3 has shown that the aerodynamic lift and moment calculated using the flow's first dynamic mode are in good agreement with the unsteady solutions even at forcing reduced frequencies that can be considered high in the context of transonic flutter problems. In general, the amplitude of the aerodynamic forces depends not only on the flow conditions and the reduced frequency but also on the plunging and pitching amplitudes $\hat{h}$ and $\hat{\alpha}$. However, if small oscillations of the geometry are considered, the amplitude of the aerodynamic forces is linear in the amplitude of the airfoil motion as discussed in Section 3.2.4. Therefore, assuming a sinusoidal motion of the airfoil and a resulting oscillating lift and moment, and separating the contribution of the plunging and pitching motions for small amplitudes, the right-hand side of the aeroelastic equations of motion becomes

$$\begin{bmatrix} -l(t) \\ m(t) \end{bmatrix} = \begin{bmatrix} \dfrac{-\hat{l}_{\text{plunge}}(k)}{\hat{h}_0} & \dfrac{-\hat{l}_{\text{pitch}}(k)}{\hat{\alpha}_0} \\ \dfrac{\hat{m}_{\text{plunge}}(k)}{\hat{h}_0} & \dfrac{\hat{m}_{\text{pitch}}(k)}{\hat{\alpha}_0} \end{bmatrix} \begin{bmatrix} \hat{h} \\ \hat{\alpha} \end{bmatrix} \mathrm{e}^{ik\tau}, \tag{4.30}$$

where $\hat{l}_{\text{plunge}}$ and $\hat{m}_{\text{plunge}}$ denote the lift and moment amplitudes due only to an imposed plunging motion of amplitude $\hat{h}_0$, and $\hat{l}_{\text{pitch}}$ and $\hat{m}_{\text{pitch}}$ represent those due to an imposed pitching motion of amplitude $\hat{\alpha}_0$. Expressing Equation (4.30) in terms of the aerodynamic

coefficients yields

$$\begin{bmatrix} -l(t) \\ m(t) \end{bmatrix} = \frac{1}{2}\rho_\infty U_\infty^2 \underbrace{\begin{bmatrix} \frac{-c\,\hat{c}_{l_{\text{plunge}}}(k)}{\hat{h}_0} & \frac{-c\,\hat{c}_{l_{\text{pitch}}}(k)}{\hat{\alpha}_0} \\ \frac{c^2\,\hat{c}_{m_{\text{plunge}}}(k)}{\hat{h}_0} & \frac{c^2\,\hat{c}_{m_{\text{pitch}}}(k)}{\hat{\alpha}_0} \end{bmatrix}}_{\mathbf{Q}} \begin{bmatrix} \hat{h} \\ \hat{\alpha} \end{bmatrix} \mathrm{e}^{ik\tau}. \tag{4.31}$$

The aerodynamic parameters $\hat{c}_{l_{\text{pitch}}}$ and $\hat{c}_{m_{\text{pitch}}}$ are calculated as follows:

- Two reference reduced frequencies are chosen for a given flow condition. The present calculations use k = 0.1 and 0.3 because the methodology must accurately capture the unsteady nonlinear aerodynamic effects over a certain range of reduced frequencies. Then, unsteady Euler or RANS simulations are performed for the airfoil in forced small amplitude pitching motion at the two chosen reduced frequencies. A small amplitude is sufficient for flutter analysis and the pitching amplitude is set to $\hat{\alpha}_0 = 1^\circ$. The fluid domain and the mesh used for these simulations are similar to those described in Section 3.2.

- The next step consists in obtaining the first dynamic modes of the resulting pressure fields by dynamic mode decomposition.

- The first dynamic pressure mode is then computed at any other reduced frequency by interpolation between the solutions at the two reference reduced frequencies. From the interpolated dynamic pressure mode, the lift and moment coefficients are determined in the frequency domain and normalized by the amplitude $\hat{\alpha}_0$ of the imposed pitching motion.

The entire procedure can be repeated for the plunging motion. The plunging amplitude $\hat{h}_0$ is set to $0.1c$ here. Finally, the matrix $\mathbf{Q}$ can be computed for a given free-stream Mach number using only four unsteady simulations. The procedure can be repeated for other values of the Mach number.

4.2.3 Flutter results

For a given Mach number, the flutter solution methods provide the variations of the frequencies f and damping coefficients γ of the system as a function of the speed index $U_{\text{index}} = U_\infty/(b\omega_\alpha\sqrt{\mu})$. Flutter occurs when at least one of the system's damping coefficients is equal to zero. The speed index at which this occurs corresponds to the flutter speed index.

Inviscid flow modeling

The results based on an inviscid flow modeling (i.e., based on Euler simulations) are analyzed first. Figure 4.3 shows the damping evolution associated with each mode of the aeroelastic system obtained by the *p-k*, modified *p-k* and *g* methods at $M_\infty = 0.85$ and $\mu = 60$. This example includes two flutter points: the damping coefficient of the first mode (mostly plunge) crosses zero at $U_{\text{index}} = 0.47$ and the damping coefficient of the second mode (mostly pitch) becomes zero at $U_{\text{index}} = 2.46$. Note that the modes of the aeroelastic system at a non-zero airspeed are linear combinations of the wind-off plunging and pitching degrees of freedom. A wind-on mode is therefore mostly plunge or mostly pitch depending on whether its frequency is closer to that of the wind-off plunge or wind-off pitch. All three methods predict the same flutter points. Indeed, at $g = 0$ (flutter), the flutter equation for the three solution techniques reduces to the same form. These methods also capture the decay rates of the modes at subcritical speeds. Slight differences are observed between the three techniques before the flutter points. In the following, the *p-k* method is chosen to compare the flutter results calculated by different aerodynamic models for consistency.

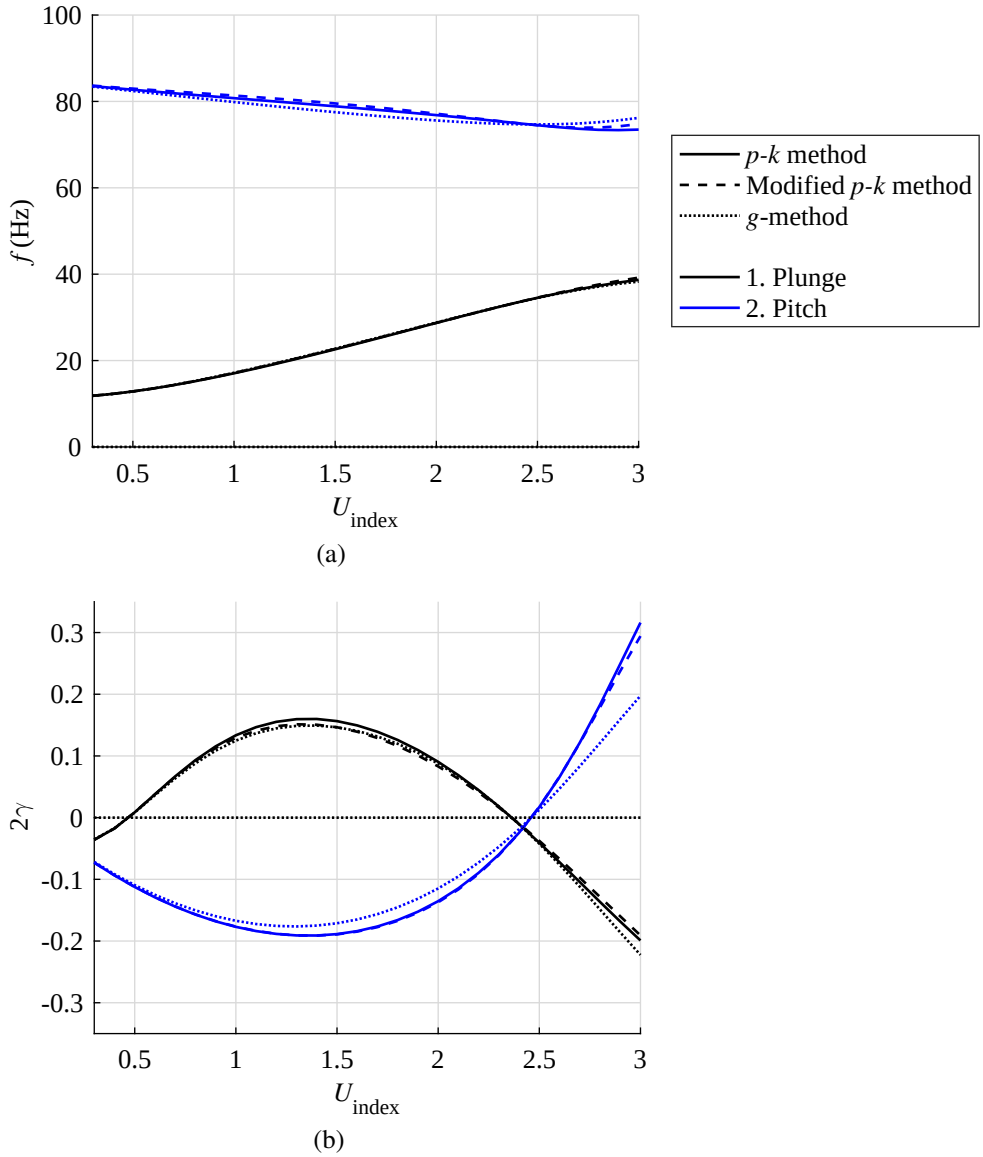

Figure 4.3: Evolution of the frequency f and the damping coefficient γ associated with each mode of the aeroelastic system as a function of the speed index U_{index} at a free-stream Mach number $M_\infty = 0.85$ and an airfoil mass ratio $\mu = 60$ obtained by the present methodology based on unsteady Euler simulations.

Although the Isogai aeroelastic problem is two-dimensional, computing its flutter boundary is challenging. This is due to the nonlinearity inherent to the transonic flow regime. In particular, the flutter speed is lower in the transonic flow regime compared to the subsonic and supersonic flow regimes as illustrated in Figure 4.4. This dramatic decrease in the flutter speed is known as the transonic dip and is caused by moving shock waves [6, 91]. This phenomenon can only be modeled by taking into account the flow nonlinearities. A steep rise of the flutter boundary occurs in the post-dip region where

the shock waves reach the trailing edge of the airfoil. Furthermore, the Isogai aeroelastic problem presents two folds in the case of inviscid flow modeling.

Figure 4.4 validates the results obtained by the present methodology by comparing them with reference solutions from the literature [48,91–93] based on unsteady Euler simulations of the full fluid-structure interaction (FSI) problem. The methodology provides a very good estimate of the flutter boundary. The transonic dip is accurately predicted. The multiple flutter points in the range $0.85 < M_\infty < 0.9$ (approximately) are directly captured with the methodology based only on four unsteady Euler simulations for each free-stream Mach number. The proposed approach provides good results at lower cost. Capturing these multiple flutter points relying on time-domain FSI simulations is more expensive because it requires simulating the unsteady response of the system for many different airspeeds and Mach numbers.

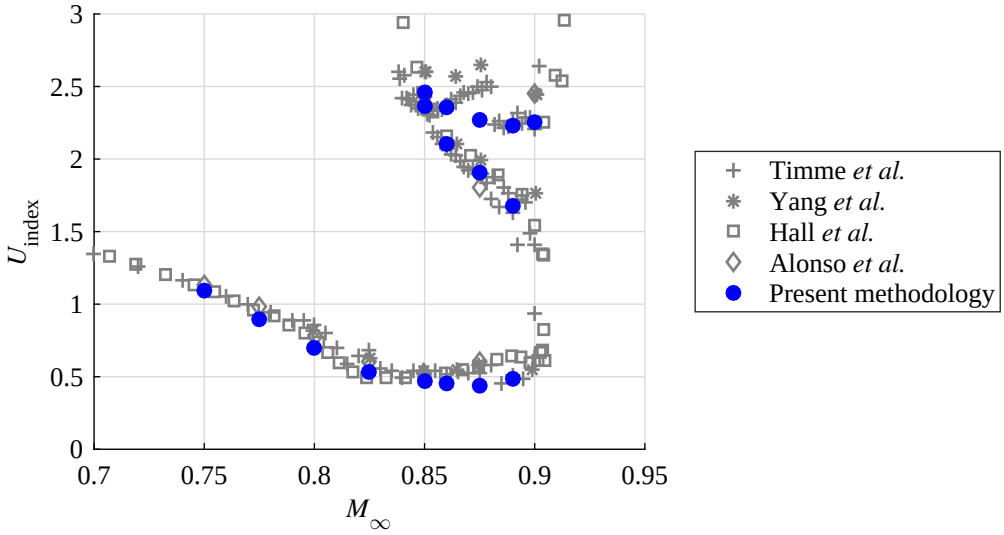

Figure 4.4: Flutter boundary (i.e., flutter speed index U_{index} as a function of the free-stream Mach number M_∞) for the Isogai wing section obtained with the present methodology and compared to time-accurate fluid-structure interaction simulations using the Euler equations [48, 91–93].

The Isogai case presents different flutter behaviors depending on the free-stream Mach number. Figure 4.5 illustrates three different flutter behaviors. All these behaviors are captured from the same four unsteady simulations for each Mach number.

- For $M_\infty = 0.75$, the two damping coefficients are negative below $U_{\text{index}} = 1.09$ and the system is therefore stable in this speed range. The damping coefficient associated with the first mode (mostly plunge) crosses zero at $U_{\text{index}} = 1.09$, which corresponds to the flutter point. The associated reduced frequency at flutter is 0.14.

- For $M = 0.875$, the aeroelastic problem presents several flutter points. The first flutter point is triggered by the first mode (mostly plunge) at $U_{\text{index}} = 0.44$ and

$k = 0.23$. This first flutter point corresponds to the critical condition that should not be exceeded in practice (e.g., wind tunnel experiments). Time-accurate aeroelastic solutions also reveal that the mode that goes unstable at the bottom of the transonic dip is mostly a plunging mode [91]. However, this flutter mode is a hump mode, i.e., it becomes stable again at $U_{\text{index}} = 1.91$. Therefore, the system is unstable from $U_{\text{index}} = 0.44$ to 1.91. Numerical simulations show that the system is stable between $U_{\text{index}} = 1.91$ and 2.25 as both damping coefficients are negative. Then, the damping coefficient of the second mode (mostly pitch) vanishes at $U_{\text{index}} = 2.25$, and the corresponding reduced frequency $k = 0.27$ is higher than the one of the first flutter point. The system remains unstable beyond this flutter speed index.

- For $M = 0.9$, the damping coefficient associated with the second mode is zero at $U_{\text{index}} = 2.25$. It appears at $k = 0.28$.

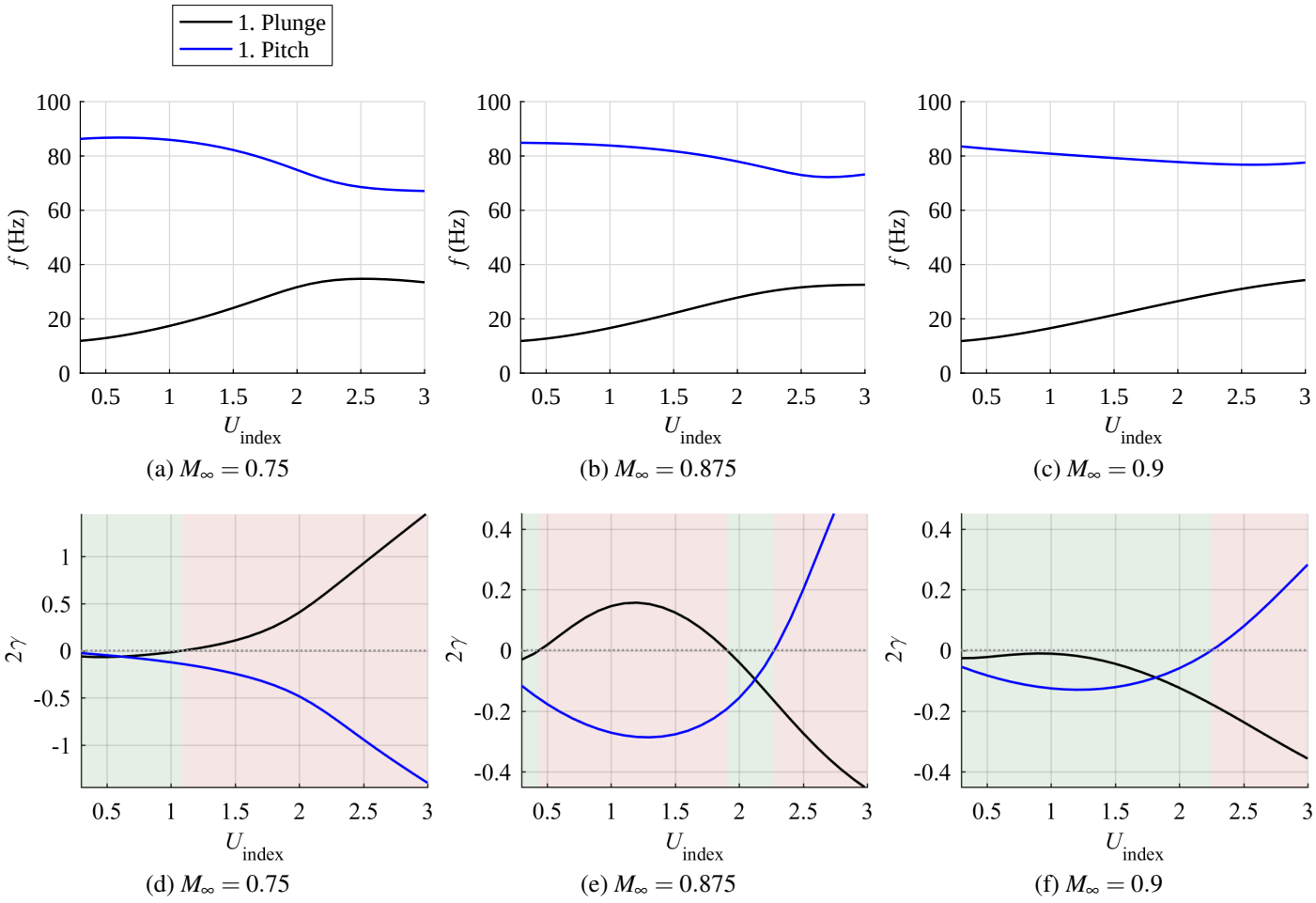

(a) $M_\infty = 0.75$ (b) $M_\infty = 0.875$ (c) $M_\infty = 0.9$

(d) $M_\infty = 0.75$ (e) $M_\infty = 0.875$ (f) $M_\infty = 0.9$

Figure 4.5: Evolution of the frequency f and the damping coefficient γ associated with each mode of the aeroelastic system as a function of the speed index U_{index} for three different free-stream Mach numbers and an airfoil mass ratio $\mu = 60$ obtained by the present methodology based on unsteady Euler simulations.

The predicted flutter mode is mostly a pitching mode for the upper unstable branch of the flutter boundary, which is consistent with the literature. However, some discrepancies are observed for this upper unstable branch between the present results and the reference data from the literature, but also among these reference data (see Figure 4.4). These differences may have different origins.

Firstly, the computational meshes might differ, introducing numerical errors. Note that in the present case, a careful mesh-refinement analysis has been performed for the high-fidelity simulations used as basis for the interpolation. The boundaries of the computational domain are far from the region of interest in order to minimize their impact on the solution, and the mesh is finer near the airfoil.

Secondly, the time step used in the unsteady Euler simulations from the literature might be too large, which could introduce numerical errors. The main reason is that most

of these works have based their time step on the frequency associated with the lower branch of the flutter boundary. The reduced frequency is slightly higher for the upper branch. However, the reduced frequency is normalized by the velocity, and the upper branch corresponds to a much larger speed index so that the frequency of the upper branch is much higher. The simulations of the second mode flutter on the upper unstable branch are thus most likely under-resolved in time [91]. In the DMI methodology, 25 snapshots are taken per period, even for the simulations at $k = 0.3$, so that the dominant modes are always resolved adequately. Nonetheless, these discrepancies at the upper branch are not excessively critical since the first flutter point appearing at a lower speed index is usually the one constraining the design and it is accurately estimated.

Finally, the interpolation operation used in the DMI methodology to obtain the modal aerodynamic force matrix $\mathbf{Q}$ can introduce an error. This potential source of discrepancy is excluded by recalculating one point of the upper branch using a much tighter interval of frequency as shown in Figure 4.6a. For example, at $M_\infty = 0.875$, the two flutter reduced frequencies are $k = 0.23$ and 0.27. These values are in the range delimited by the reference k given by 0.1 and 0.3. Using more reference reduced frequencies in this interval ($k = 0.1$, 0.15, 0.2, 0.25 and 0.3) provides a better approximation of the flutter points because the errors related to the dynamic mode interpolation are reduced. Nevertheless, using only two reference k equal to 0.1 and 0.3 does not change much the flutter predictions, which suggests to rely on these two reference k for fast but still accurate flutter calculations.

The solutions can be less accurate if the two reference k are too far apart. This is illustrated in Figure 4.6b where the sensitivity of the method on the two selected frequencies is analyzed. For example, relying on $k = 0.1$ and 0.5 overestimates the flutter speeds, especially the one on the upper branch, compared to the most accurate solution. On the other hand, using a narrow interval $k = 0.1$ and 0.15 below the flutter reduced frequencies still gives good estimates of the flutter points for this simple configuration. Extrapolation from the reference frequencies is thus acceptable provided that the flutter k are not too far from the reference k. For a reliable flutter prediction, the range covered by the reference reduced frequencies must be close to the flutter reduced frequency. This condition can be verified a posteriori based on the flutter results. While general guidelines cannot be formulated, in practice, a first set of values for k can be used and, depending on the results, the calculation could be repeated using improved values.

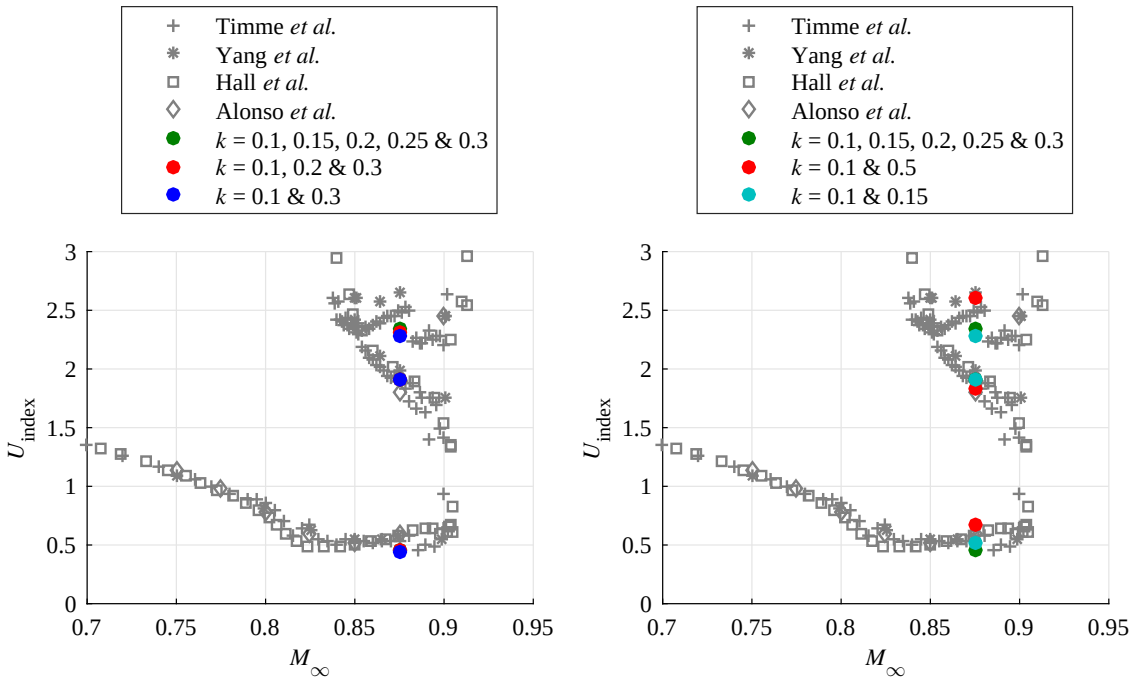

(a) (b)

Figure 4.6: Flutter boundary (i.e., flutter speed index U_{index} as a function of the free-stream Mach number M_∞) for the Isogai wing section obtained with the present methodology based on different sets of reference reduced frequencies and compared to time-accurate fluid-structure interaction simulations using the Euler equations [48, 91–93].

Viscous flow modeling

Figure 4.7 compares the flutter boundary at a Reynolds number $Re = 6 \times 10^6$ computed using the present methodology based on unsteady RANS simulations with some reference results obtained from time-domain FSI simulations [92]. The methodology provides a very good prediction of the transonic flutter boundary. In particular, the transonic dip is well captured. The first mode of vibration is the flutter mode for each point of the flutter boundary. The methodology achieves an accuracy similar to the time-accurate FSI simulations, but at a lower computational cost. This analysis illustrates that the proposed methodology can also be used using RANS modeling.

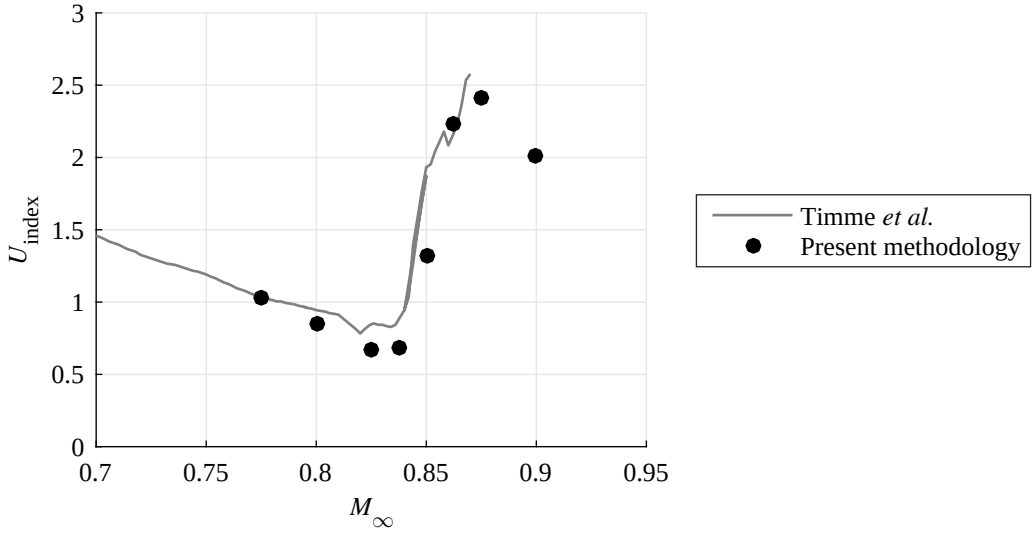

Figure 4.7: Flutter boundary at a Reynolds number $Re = 6 \times 10^6$ for the Isogai wing section obtained with the present methodology and compared to time-accurate fluid-structure interaction simulations using the RANS equations [92].

Figure 4.8 compares the predictions of the present methodology based on the unsteady RANS and Euler models. To further highlight the advantage of the methodology, the results obtained with a typical linear panel method are also shown for comparison [6]. Although the linear aerodynamic models are very fast, they fail to correctly capture the decrease of the flutter speed index in the transonic region because they do not model the moving shock waves. The flutter speed index is overpredicted in the transonic flow regime, which can lead to an inappropriate and unsafe design. This comparison highlights the importance of including shock waves for flutter calculations in transonic conditions.

It can be seen that the RANS model reduces the amplitude and extent of the transonic dip compared to the inviscid case. It also suppresses the fold of the flutter boundary and the higher-frequency flutter mode appearing in the inviscid case. The flutter speed index is slightly higher than the Euler solution until $M_\infty = 0.825$. The steep increase in the flutter speed index appears at a lower free-stream Mach number for the RANS model ($M_\infty \approx 0.84$) compared to the Euler model ($M_\infty \approx 0.89$). Including the viscous boundary layer significantly affects the flutter boundary in the transonic flow regime.

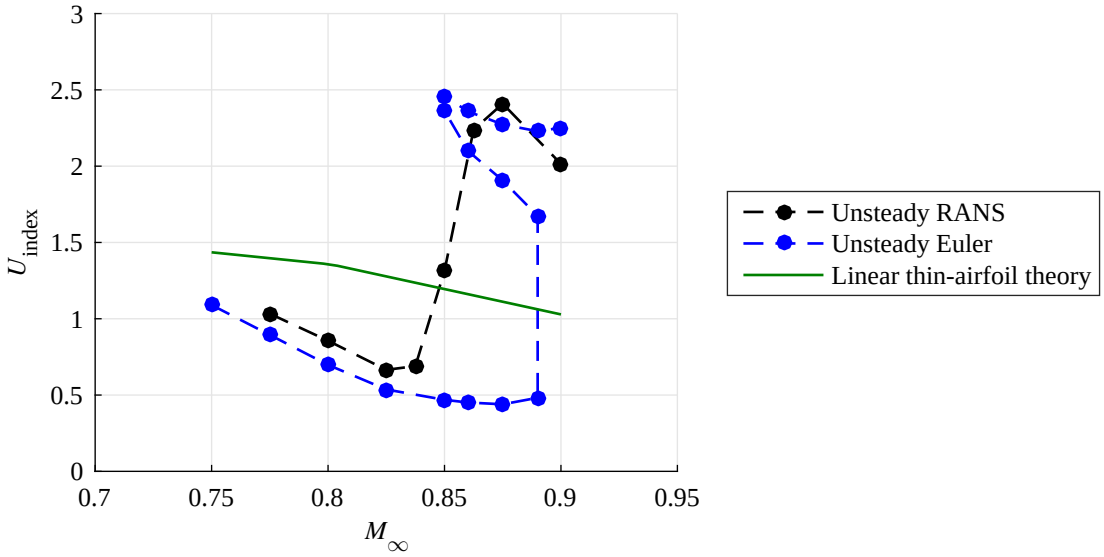

Figure 4.8: Flutter boundary for the Isogai wing section obtained with the present methodology based on viscous flow modeling at $Re = 6 \times 10^6$ and inviscid flow modeling. The flutter boundary obtained from the linear thin-airfoil theory is also shown.

Figure 4.9 plots the modal damping against airspeed for $M_\infty = 0.85$, which allows the characterization of the subcritical behavior of the system. There are significant differences between the viscous and inviscid cases. In the viscous case, only the damping coefficient of the first mode becomes zero, and the flutter speed index is much higher than the first flutter point appearing in the inviscid case. Moreover, the flutter mechanism obtained with viscous flow modeling is less abrupt compared to the inviscid case as the critical damping coefficient approaches the critical speed with a smaller gradient.

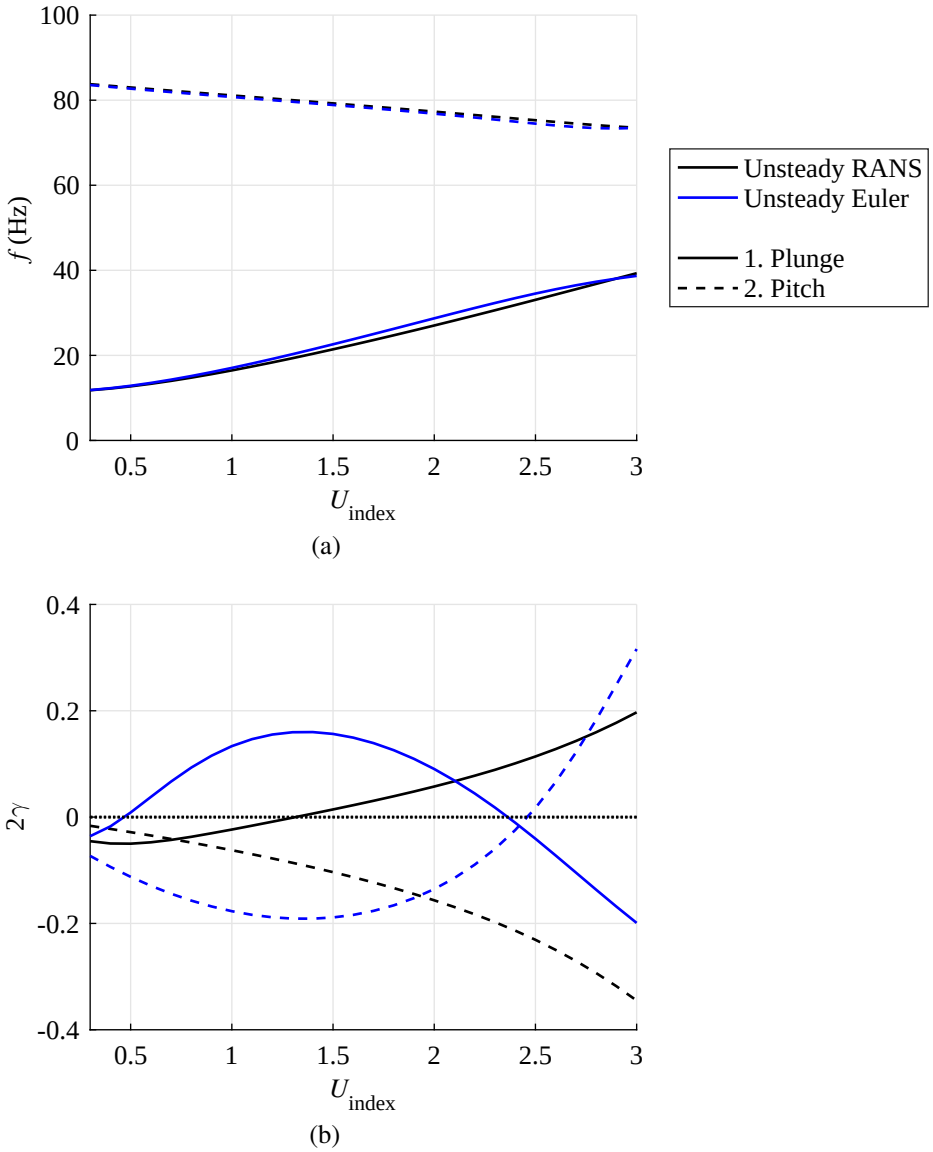

Figure 4.9: Evolution of the frequency f and the damping coefficient γ associated with each mode of the aeroelastic system as a function of the speed index U_{index} for a free-stream Mach number $M_\infty = 0.85$ obtained by the present methodology. The black curves correspond to the viscous flow results at a Reynolds number $Re = 6 \times 10^6$ and the blue curves to the inviscid flow results.

Now that the results obtained with our methodology have been validated, the influence of the Reynolds number will be analyzed in more detail in the next section.

4.2.4 Influence of the Reynolds number

As the Reynolds number decreases, the thickness of the boundary layer increases and the flutter speed index increases in the transonic flow regime as can be seen in Figure 4.10.

The results computed by including the boundary layer are more conservative compared to the inviscid results. It is therefore advantageous to rely on the Euler approach to compute the flutter boundary in the transonic flow regime for this system that does not experience large regions of flow separation. Firstly, the flutter speed obtained using the Euler approach is more restrictive. Secondly, unsteady Euler simulations have lower computational cost than unsteady RANS ones. In addition, the meshing is easier for the Euler model because there is no constraint for the first grid spacing as the boundary layer is not modeled.

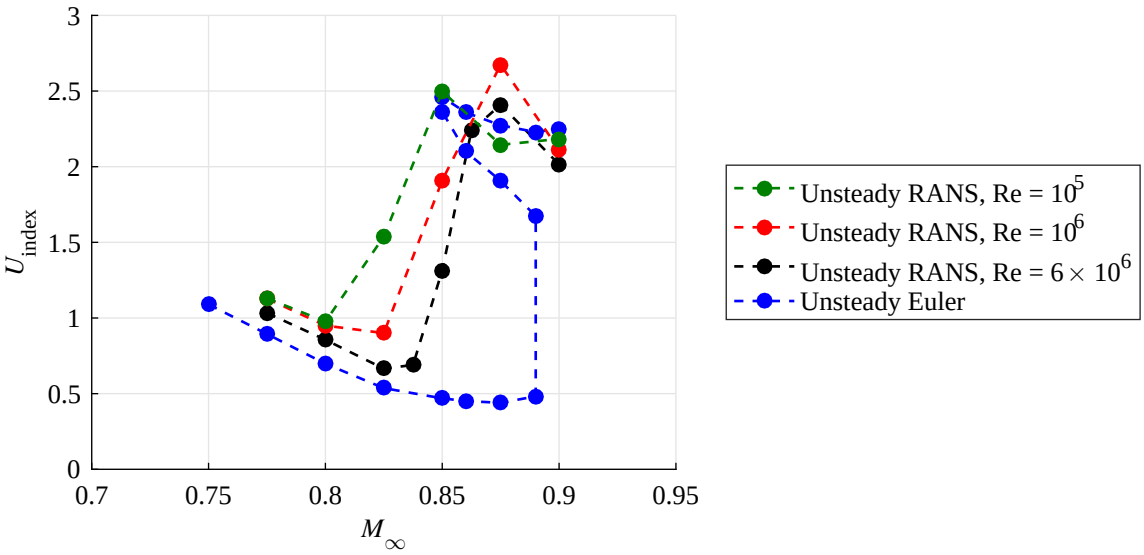

Figure 4.10: Influence of the Reynolds number *Re* on the flutter boundary for the Isogai wing section obtained with the present methodology.

In order to better understand the effect of the Reynolds number, the aerodynamic force matrix $\mathbf{Q}$ is considered at a particular condition: the flutter point obtained with the Euler model at $M_\infty = 0.825$ where $U_{\text{index}} = 0.5354$ and $k = 0.2012$. Figure 4.11 shows the components of $\mathbf{Q}(k = 0.2012)$ that are directly related to the aerodynamic lift and moment coefficients due to the plunging and pitching motions as indicated in Equation (4.31). The imaginary part of $\mathbf{Q}$ quantifies the amount of aerodynamic damping present in the aeroelastic equations. A positive value of a component of $\Im(\mathbf{Q})$ gives a negative aerodynamic damping as can be inferred from Equation (4.28). In the example of Figure 4.11, only the Euler model, which predicts an unstable response at this particular condition, has components with a positive imaginary part.

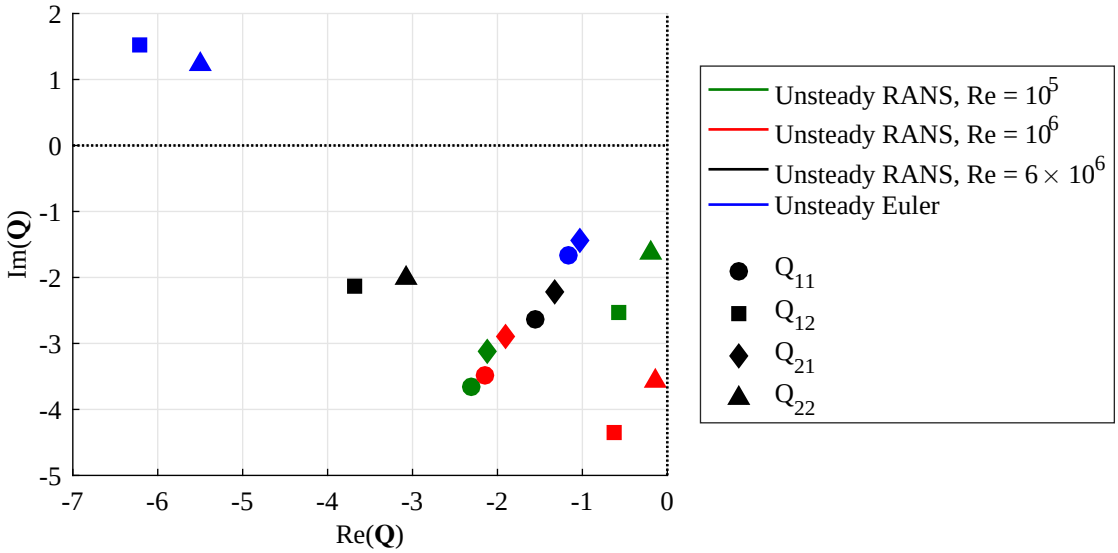

Figure 4.11: Components of the aerodynamic force matrix $\mathbf{Q}$ at a free-stream Mach number $M_\infty = 0.825$ and a reduced frequency $k = 0.2012$ corresponding to the flutter point predicted by the Euler model.

The matrix $\mathbf{Q}$ is directly related to the unsteady pressure distributions. The distribution of the surface pressure coefficient C_p can be written as

$$C_p(x,y,z,t) \approx \bar{C}_p(x,y,z) + \Im\left(\hat{C}_p(x,y,z)\, e^{i\omega t}\right), \tag{4.32}$$

where $\bar{C}_p(x,y,z)$ and $\hat{C}_p(x,y,z)$ are respectively the mean and amplitude of the unsteady pressure coefficient. The pressure field at a particular reduced frequency is directly available using the dynamic mode interpolation.

Figure 4.12 compares the amplitude of the unsteady pressure coefficient difference between the upper and lower surfaces $\Delta\hat{C}_p$ at the same conditions as Figure 4.11. The main differences appear in the height of the peak in the shock wave region, which directly affects the amplitude and phase of the aerodynamic coefficients associated with the plunging and pitching motions. The peak is higher in the Euler solutions. The effects of the moving shock waves are therefore more pronounced in the inviscid case, decreasing the flutter speed. As the Reynolds number decreases, the height of the peak decreases. Therefore, the influence of the shock waves on $\Delta\hat{C}_p$ becomes weaker when Re is reduced and the thickness of the boundary layer increases. This phenomenon further highlights the importance of shock motion on the flutter stability of transonic wings.

It should be emphasized that the accuracy of the viscous results depends on the turbulence model used in the RANS calculations. In other words, the results can only be as good as the turbulence modeling. Because the present work mainly focused on the overall methodology, the simple SA model was deemed sufficient. Nonetheless, one should

keep this limitation in mind when interpreting the RANS results and the impact of viscous effects on the flutter boundary. In particular, better RANS models should be considered. This is beyond the scope of the present analysis and thus left as future work.

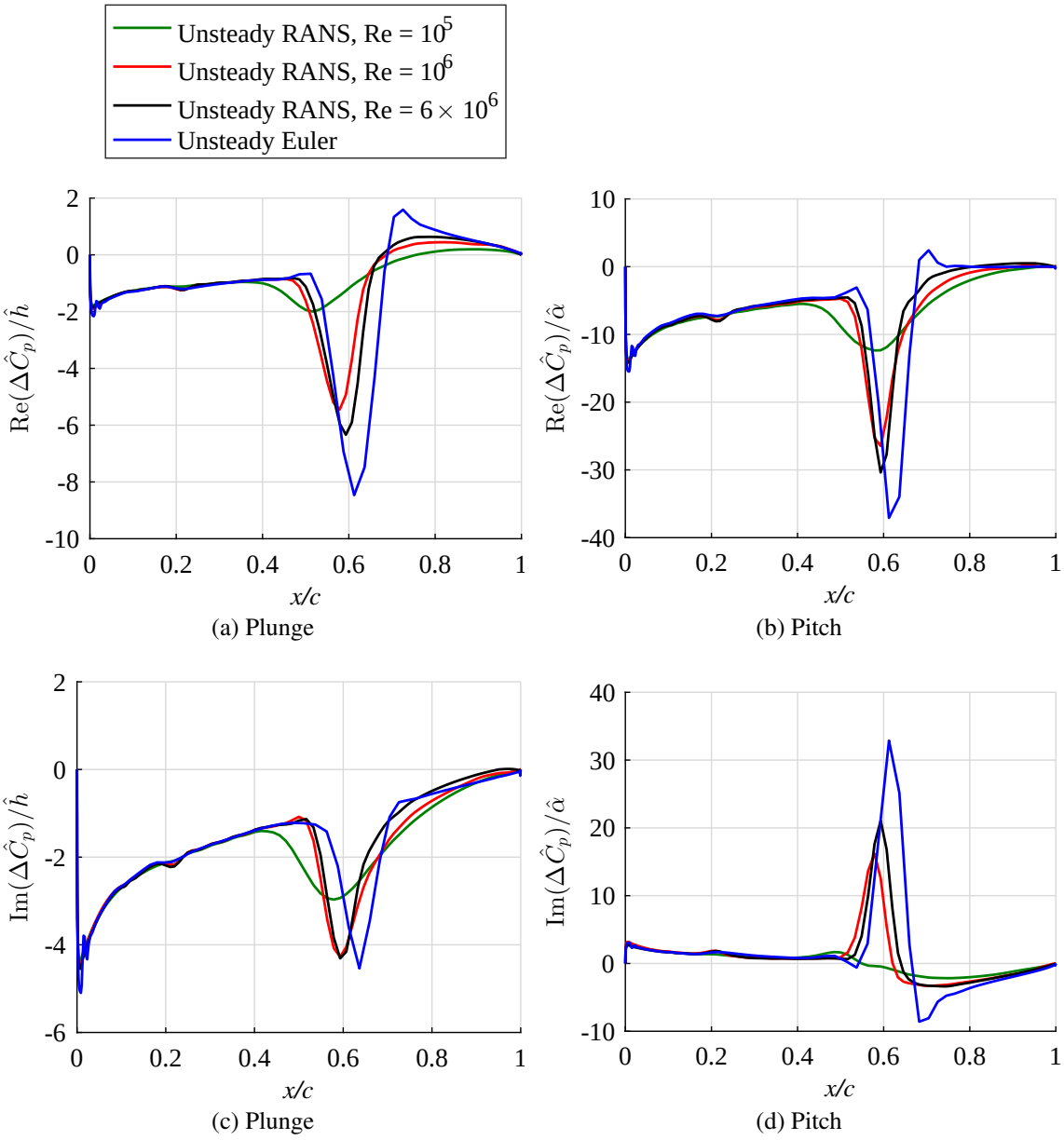

(a) Plunge (b) Pitch

(c) Plunge (d) Pitch

Figure 4.12: Amplitude of the unsteady pressure coefficient difference between the upper and lower surfaces $\Delta\hat{C}_p$ that results from imposing a harmonic pitching or plunging motion at a free-stream Mach number $M_\infty = 0.825$, a reduced frequency $k = 0.2012$ and different Reynolds numbers. The values are normalized by the amplitude of the motion.

The 2D pitch and plunge airfoil configuration has been used to validate the flutter solutions predicted by the proposed methodology for inviscid and viscous flow modeling. The analysis has shown that the nature of the transonic dip depends on the spatial and

temporal variations of the shock waves and their strength. The next section applies the methodology to a 3D wing configuration.

4.3 AGARD 445.6 wing

In this section, the methodology is used to analyze the aeroelastic stability of the three-dimensional AGARD wing validation case. The accuracy of the methodology is assessed by comparing with results available in the literature.

4.3.1 Structural model

The AGARD 445.6 wing model considered here corresponds to the weakened wall-mounted semispan model 3 of Yates et al. [94]. The cross section is a symmetric NACA 65A004 profile. The model is made of laminated mahogany wood. The geometrical and structural characteristics are summarized in Tables 4.1 and 4.2.

Parameter	**Symbol**	**Value**
Root chord	c_r	0.559 m
Tip chord	c_t	0.368 m
Taper ratio	λ	0.658
Quarter-chord sweepback	Λ	45°
Mean aerodynamic chord	$\bar{\bar{c}}$	0.470 m
Semi-span	b_s	0.762 m
Aspect ratio	AR	1.621
Wing surface	S	0.353 m^2

Table 4.1: Geometrical parameters of the AGARD 445.6 wing.

Parameter	**Symbol**	**Value**
Longitudinal Young's modulus	E_1	3.151 GPa
Transverse Young's moduli	E_2, E_3	0.4162 GPa
Shear moduli	G_{12}, G_{13}, G_{23}	0.4392 GPa
Poisson's ratio	ν_{12}, ν_{13}, ν_{23}	0.31
Density	ρ_s	381.98 kg/m^3

Table 4.2: Material properties of the AGARD 445.6 wing.

The finite element model constructed using Metafor has already been validated in Thomas et al. [95]. This structural model is used to obtain the mass matrix $\mathbf{M}$, the stiffness matrix $\mathbf{K}$, the modal matrix $\mathbf{\Phi}$ and the modal frequencies. The matrices $\mathbf{M}$, $\mathbf{K}$ and $\mathbf{\Phi}$ are all square matrices of size $N \times N$ with N the total number of degrees of freedom

contained in the finite element model. The first four modes of vibration of the structure are considered as for the reference article of Thomas et al. [95] where unsteady Euler-based fluid-structure interaction (FSI) simulations of the same flow problem have been performed. Therefore, the modal matrices $\mathbf{M}_q$ and $\mathbf{K}_q$ are square matrices of reduced size $n \times n$ where $n = 4$. The mode shapes and their characteristics are given in Figure 4.13. The fourth mode has a natural frequency about ten times higher than that of the first mode.

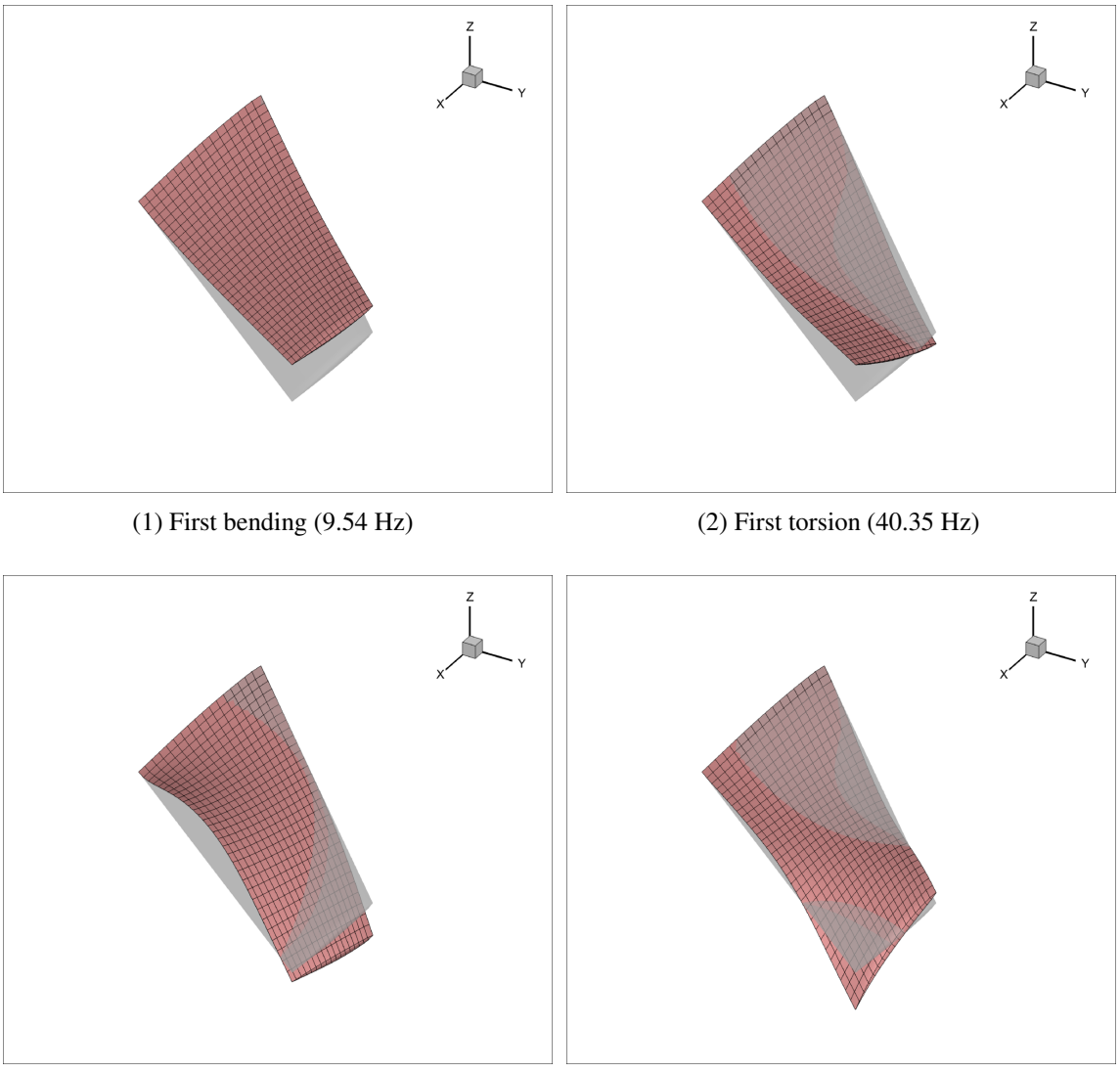

(1) First bending (9.54 Hz)

(2) First torsion (40.35 Hz)

(3) Second bending (50.22 Hz)

(4) Second torsion (97.67 Hz)

Figure 4.13: First four mode shapes of the AGARD 445.6 wing.

4.3.2 Unsteady aerodynamic forces

The DMI methodology is used to calculate the aerodynamic forces as a function of the reduced frequency included in the matrix $\mathbf{N}(ik)$. The computational domain for the Euler and RANS simulations is a large hemisphere that extends up to $25c_r$ from the wing in each direction as illustrated in Figure 4.14. The geometry of the wing has a rounded trailing edge and a rounded wing tip. The wing root is attached to the boundary in the x-z plane where a symmetry condition is used to mirror the flow with respect to that boundary in order to reduce the computational cost.

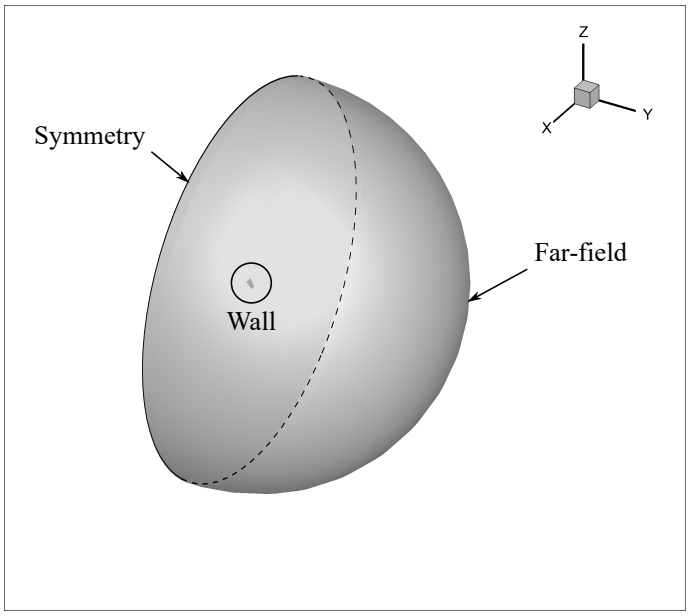

Figure 4.14: Computational domain used for the unsteady Euler and RANS simulations.

For the Euler simulations, the structured mesh generated by Gmsh consists of 248,000 hexahedra elements and 238,719 nodes. It corresponds to the same resolution as in the reference article [95], which is used to compare the present methodology with unsteady Euler-based fluid-structure interaction simulations. The mesh on the surface of the wing and plane of symmetry is shown in Figure 4.15.

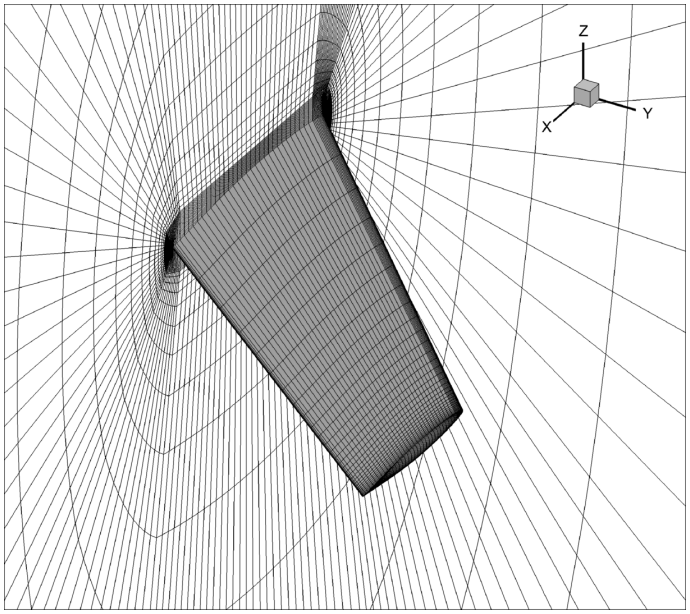

Figure 4.15: Computational grid used for the unsteady Euler simulations.

The geometry of the structural model is the same as the wing aerodynamic shape. However, the structural grid (1230 nodes on the wing surface) is different from the CFD mesh (6280 nodes on the wing surface). Different interpolation methods can be used to transfer the structural mode shapes to the CFD mesh. Even a simple bilinear interpolation works well in this case for the displacements as illustrated for the first mode shape in Figure 4.16.

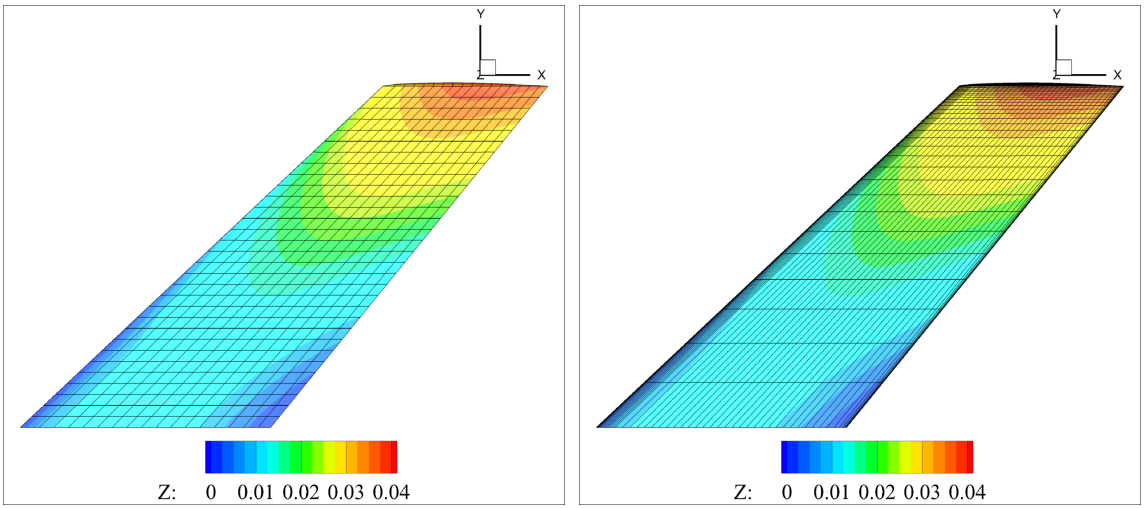

(a) Structural mesh

(b) CFD mesh on the wing surface

Figure 4.16: Interpolation of the bending mode from the structural mesh to the CFD mesh on the wing surface. The contours show the z degree of freedom (vertical position).

The numerical tool CUPyDO [95] is used to prescribe the motion of the boundary surface in time for the CFD simulations performed in SU2. For each of the four chosen modes, two unsteady Euler or RANS simulations are carried out for the wing oscillating in simple harmonic motion at two different forcing reduced frequencies $k = 0.05$ and 0.2 based on half the mean aerodynamic chord $\bar{\bar{c}}$. The mean position of the wing corresponds to the undeformed wing at an angle of attack of zero degrees. Similarly to the 2D case discussed in Section 4.2, the imposed amplitude of the sinusoidal motion is kept small, so that a linear behavior with respect to the amplitude can be assumed for the unsteady pressure. Specifically, the maximum out-of-plane deflection of the wing is set to $0.08\,\bar{\bar{c}}$.

Figure 4.17 shows snapshots of the Mach contours obtained from the unsteady Euler simulations for the first bending and first torsion modes at $M_\infty = 0.96$. Large regions of supersonic flow are visible on the wing surface. The extent of the supersonic region varies with phase angle; this variation is more important in the torsion motion.

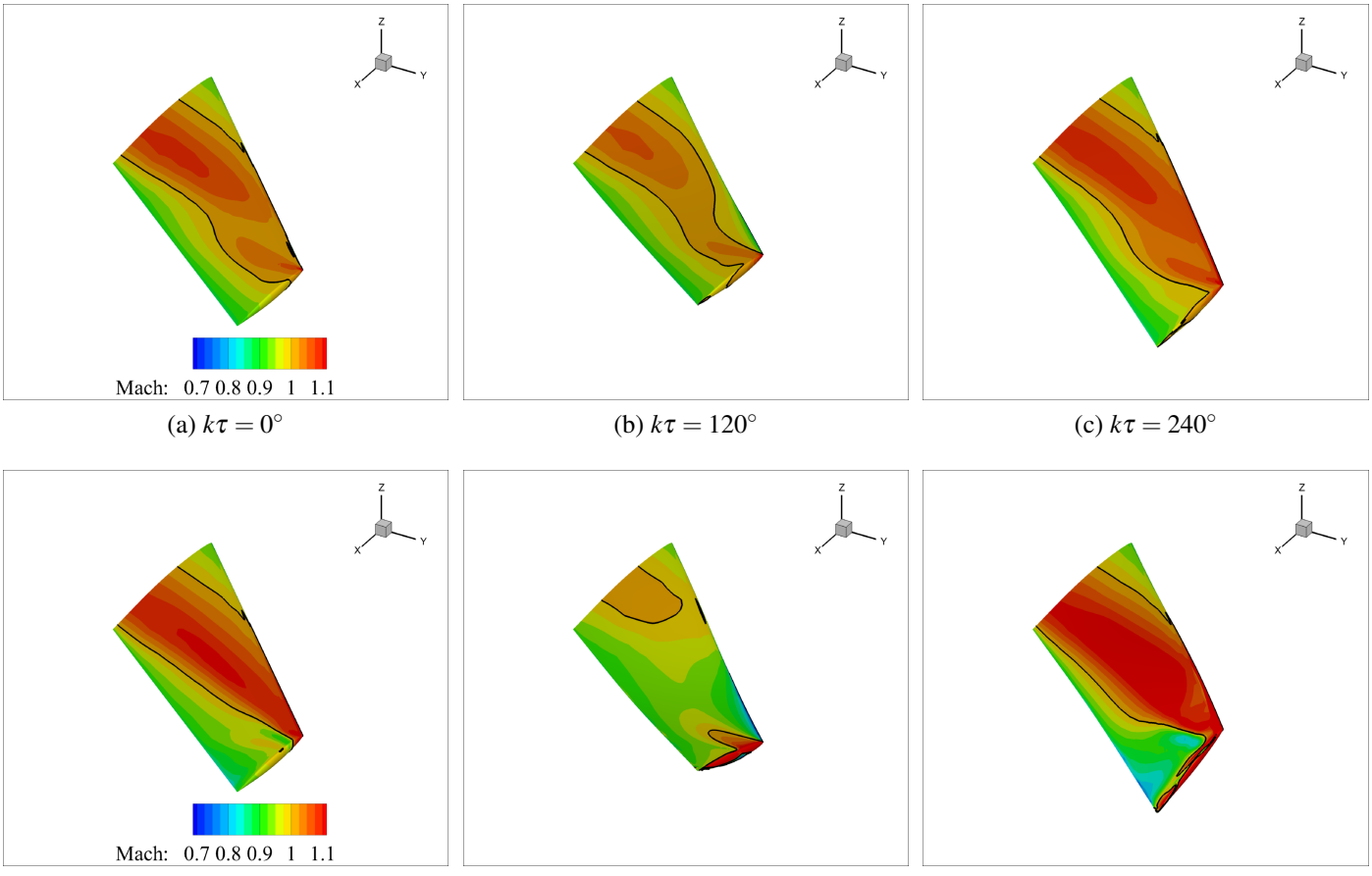

(a) $k\tau = 0°$ (b) $k\tau = 120°$ (c) $k\tau = 240°$

(d) $k\tau = 0°$ (e) $k\tau = 120°$ (f) $k\tau = 240°$

Figure 4.17: Contours of the Mach number at three phases of (a-c) the mode 1 motion and (d-f) the mode 2 motion at a free-stream Mach number $M_\infty = 0.96$ obtained by unsteady Euler simulations. The black line represents $M = 1$.

The reference unsteady Euler simulations generate the unsteady flow fields that can be processed using DMD in order to obtain the reference dynamic modes. Following the guidelines of Chapter 4, only the first dynamic modes are considered in the dynamic mode interpolation procedure to estimate the flow response at any reduced frequency k. The accuracy of this assumption is verified in Figure 4.18 where the variation of the lift coefficient of the AGARD 445.6 wing due to forced modal deformations at $k = 0.1$ is estimated from interpolation of the reference first dynamic pressure modes for $k = 0.05$ and 0.2. It can be seen that the solutions based on one interpolated DMD mode are in good agreement with the exact unsteady Euler solutions at $k = 0.1$ for all bending and torsion modes of the wing. The dynamic mode interpolation is therefore able to accurately capture the variation of the aerodynamic forces in a range of reduced frequencies for all modes of vibration of a three-dimensional wing.

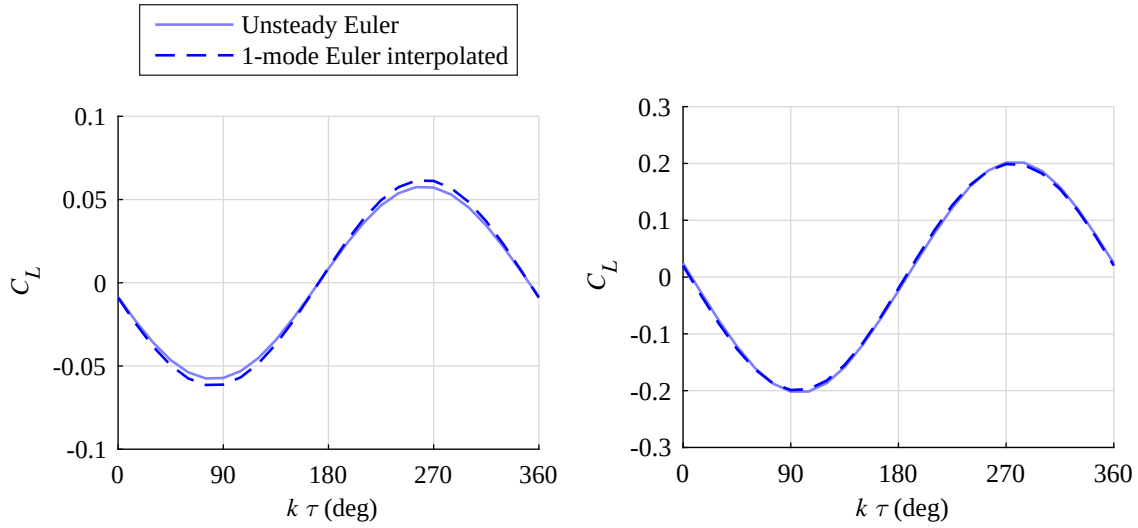

(1) First bending

(2) First torsion

(3) Second bending

(4) Second torsion

Figure 4.18: Comparison between the unsteady Euler solutions and the present dynamic mode interpolation approach using the first dynamic pressure modes at two reduced frequencies $k = 0.05$ and 0.2 to predict the lift coefficient C_L of the AGARD 445.6 wing oscillating in the direction of its modes of vibration at $k = 0.1$ and a free-stream Mach number $M_\infty = 0.9$.

4.3.3 Flutter results

The range of free-stream Mach numbers extends from $M_\infty = 0.499$ to 1.141 in the experimental investigation [94] as indicated in Table 4.3. The Reynolds numbers based on the experimental conditions and the mean aerodynamic chord are in the range $Re = 0.546 \times 10^6$ to 1.890×10^6.

Mach	**Reynolds number**	**Density (kg/m^3)**
0.499	1.890×10^6	0.4278
0.678	1.260×10^6	0.2082
0.901	0.816×10^6	0.0995
0.960	0.596×10^6	0.0634
1.072	0.546×10^6	0.0551
1.141	0.829×10^6	0.0783

Table 4.3: Flow conditions for the aeroelastic analysis of the AGARD 445.6 wing.

The speed index for the AGARD 445.6 wing case is defined as

$$U_{\text{index}} = \frac{U_\infty}{0.5 c_r \omega_2 \sqrt{\mu}}, \tag{4.33}$$

where ω_2 is the natural frequency of the first torsion mode and $\mu = m/(\rho_\infty V)$ is the mass ratio with $m = 1.863$ kg and $V = 0.130$ m^3. Figure 4.19 shows the frequency and damping values as a function of the speed index computed by the *p-k* method at $M_\infty = 0.901$ and $\rho_\infty = 0.0995$ kg/m^3. The damping of the first mode crosses the zero-damping axis at $U_{\text{index}} = 0.3537$. The frequency curves corresponding to the first and second modes of vibration approach each other as U_{index} increases indicating a coupling between these two modes. The curves associated with the third and fourth modes remain essentially constant suggesting that their impact on the onset of the flutter instability is negligible.

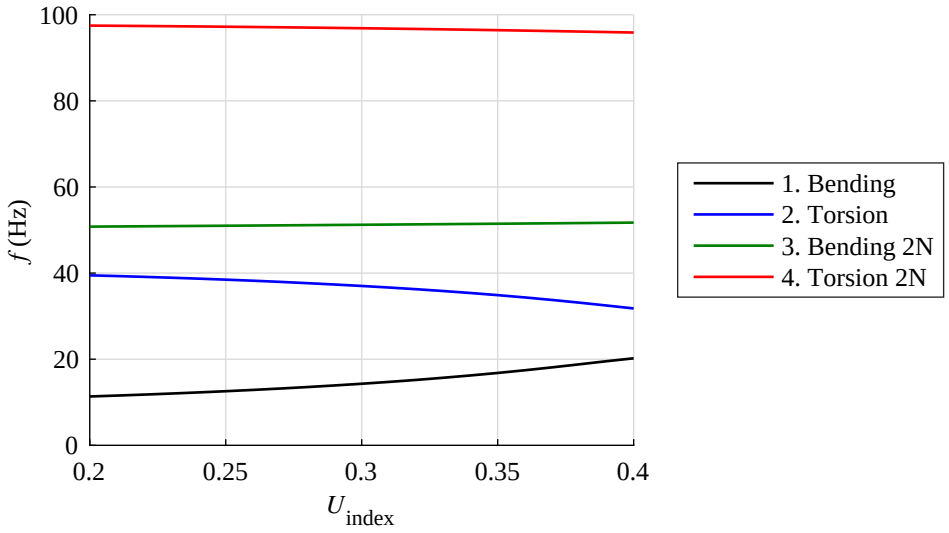

(a)

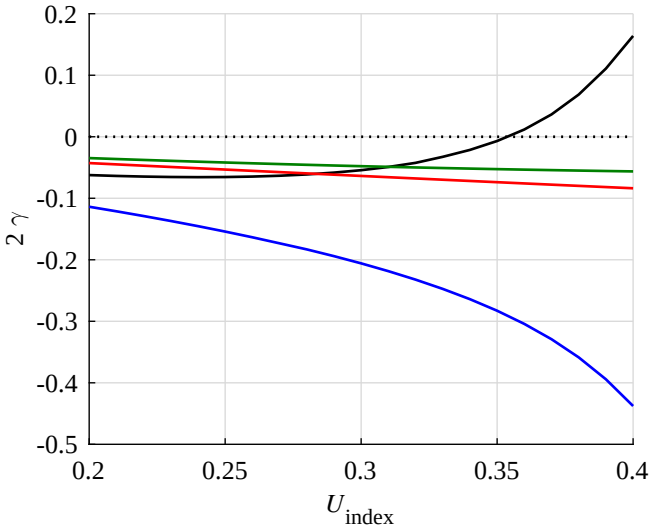

(b)

Figure 4.19: Evolution of the frequency f and the damping coefficient γ associated with each mode of vibration of the AGARD 445.6 wing as a function of the speed index U_{index} for a free-stream Mach number $M_\infty = 0.901$ and a free-stream density $\rho_\infty = 0.0995\ \text{kg}/\text{m}^3$ obtained by the present methodology based on unsteady Euler simulations.

Figure 4.20 demonstrates that the flutter boundary in the subsonic and transonic flow regime computed by the present methodology is in good agreement with the experiment and the numerical flutter results from the literature at the same Mach numbers and mass ratios [94–98]. The transonic dip is accurately predicted. The first mode (mostly bending), which has the lowest natural frequency, is the flutter mode for all considered Mach numbers.

Since the methodology can only be as good as the FSI results, one can observe some

discrepancies with the experimental data for supersonic Mach numbers similarly to other numerical studies. The cause of these discrepancies is unclear. As suggested by Thomas et al. [95], the wing tip geometry (sharp or rounded), the viscous effects or the effect of the structural damping could have an impact on the flutter boundary in the supersonic flow regime.

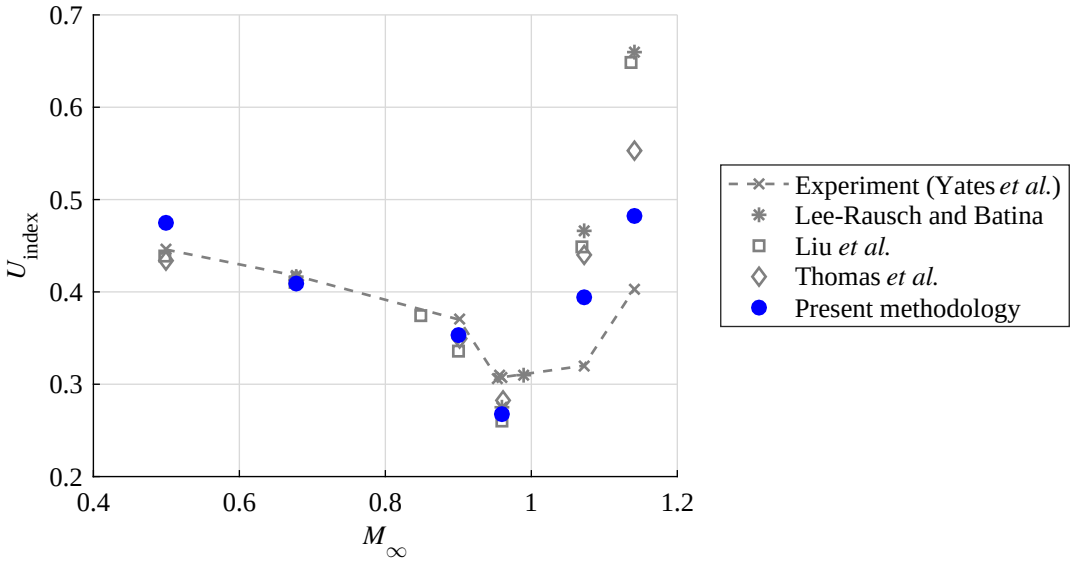

Figure 4.20: Flutter boundary (i.e., flutter speed index U_{index} as a function of the free-stream Mach number M_∞) for the AGARD 445.6 wing obtained with the present methodology and compared to time-accurate fluid-structure simulations using the Euler equations [94, 95, 97, 98].

4.3.4 Inclusion of the viscous boundary layer

In this section, the DMI-based aeroelastic methodology is used based on unsteady RANS simulations. The meshes have a similar resolution to the one presented in Figure 4.15, but the region around the wing is refined to properly capture the boundary layer.

As shown in Figure 4.21, the flutter speed indices predicted by the RANS model are higher than those calculated with the Euler model. This observation is consistent with the results obtained for the Isogai wing section aeroelastic case presented in Figure 4.8. The RANS model reduces the amplitude of the transonic dip compared to the inviscid case and it is in better agreement with the experimental measurements for subsonic free-stream Mach numbers, especially at $M_\infty = 0.96$. However, the inclusion of the viscous boundary layer does not explain the discrepancies appearing for supersonic free-stream Mach numbers.

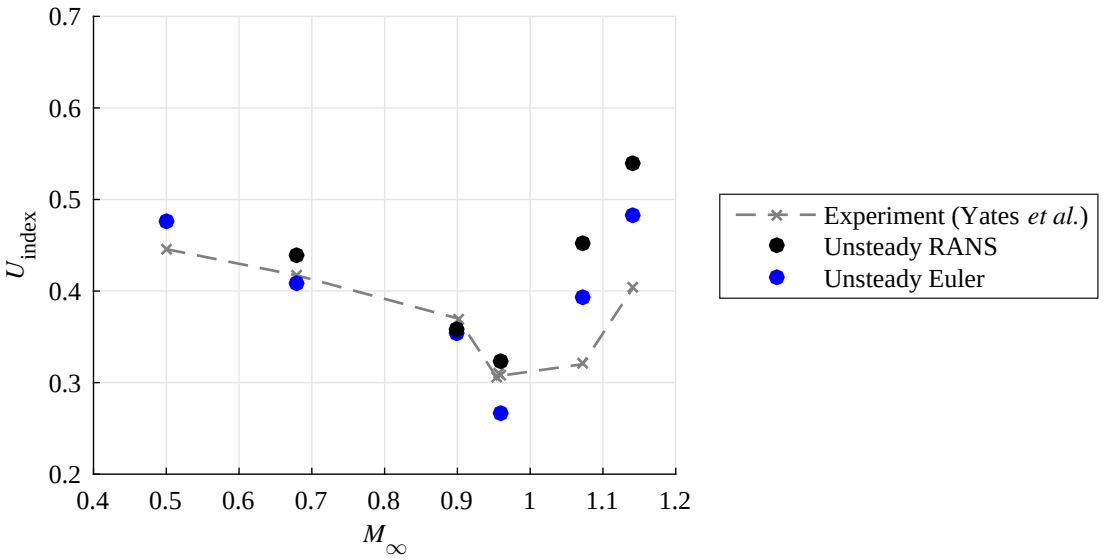

Figure 4.21: Flutter boundary for the AGARD 445.6 wing obtained from the experiment and the present methodology based on viscous and inviscid flow modeling.

In this case, the computational time required to reach a fully established periodic state (approximately 4 periods of oscillation) is about 3.21 hours on 16 cores (Intel E5-2650 processors at 2.0 GHz) for an unsteady Euler simulation and 9.04 hours for an unsteady RANS simulation. A more detailed evaluation of the accuracy and computation cost of the proposed methodology compared to industrial methods and higher fidelity fluid-structure interaction simulations is presented in Chapter 5.

4.4 Concluding remarks

The transonic flutter calculation methodology based on only two reference frequencies is able to predict the flutter boundary of the 2D Isogai airfoil and 3D AGARD 445.6 wing models with a precision similar to that of higher fidelity fluid-structure interaction (FSI) simulations, but at a lower computational cost.

A sensitivity analysis has been performed regarding the choice of the forcing reduced frequencies. It has been concluded that the range covered by these reference reduced frequencies must be close to the flutter reduced frequency for reliable flutter prediction. This condition must be checked a posteriori.

This chapter has illustrated that taking into account aerodynamic nonlinearities such as transonic shocks and viscous boundary layers significantly affects the flutter boundary. The strength and dynamics of the shock waves have an important impact on the shape of the well-known transonic dip characterized by a dramatic decrease in the flutter speed in

the transonic flow regime. In the considered cases, the flows remain essentially attached and the resulting inviscid flutter solutions are more restrictive than the viscous solutions. Chapter 5 will thus use the methodology based on unsteady Euler simulations to study the aeroelastic stability of a more complex and realistic wing structure.

Chapter 5

Transonic flutter calculations of the Embraer benchmark wing and comparison with standard industrial methods

This chapter addresses the problem of calculating the transonic aeroelastic stability of a benchmark wing made of composite materials that has been provided by the Brazilian aerospace company Embraer[1]. This application is important because future aircraft developments benefit from significant weight savings and efficiency improvement resulting from the widespread use of composite materials and multidisciplinary optimization procedures [99, 100]. As the structural mass decreases, the dynamic behavior of composite wings can become increasingly dominated by aeroelastic effects. The main objectives of this chapter are to apply our transonic flutter calculation methodology to this realistic composite wing and to compare its performance (accuracy and computational cost) with different methods commonly used in the industry during the preliminary design.

This chapter is organized as follows. The different levels of fidelity used to model the aeroelastic problem are first presented. This is followed by a description of the aeroelastic case. This chapter also introduces the infinite plate spline technique used to transfer the mode shapes from the internal structure to the wing skin. The contributions of the novel methodology are then highlighted by comparing unsteady pressure distributions and flutter results with industrial methods. Finally, higher fidelity time-accurate fluid-structure interaction simulations are performed in order to validate the flutter predictions. The following key questions are also investigated:

- How does a better prediction of moving shocks impact the flutter onset in the case

[1] http://embraer.com

of a realistic composite wing?

- What are the additional difficulties that can be encountered with flexible composite wings in transonic conditions from an aeroelastic modeling point of view?

5.1 Unsteady aerodynamic models

A review of the different unsteady aerodynamic models used for aeroelastic stability calculations has been presented in Chapter 2. In this chapter, the modal aerodynamic force matrix in the frequency domain $\mathbf{Q}(ik)$ is computed at different levels of fidelity using the following four tools:

- **ZONA6** is an unsteady panel method for solving the linearized potential flow equation, which is available in the ZAERO software package [23, 26]. This unsteady panel method is suitable for studying purely subsonic flows over lifting surfaces or wing-body configurations. However, the linearized potential equation cannot handle nonlinear transonic effects. It is thus expected that ZONA6 will fail to capture the shock waves present in transonic flows.

- **ZTRAN** is an unsteady field-panel method featured in ZAERO that solves the time-linearized transonic small disturbance (TLTSD) equation. The unsteady flow due to small perturbations is decomposed into a steady background flow contribution and an unsteady linear potential contribution. In this work, the steady background flow is obtained from a steady Euler simulation using the commercial solver CFD++ [101]. The unsteady linear potential contribution is computed by ZONA6. There is no guarantee that the nonlinear dynamics of the shock waves is accurately calculated since the steady background flow contains only information on the steady shocks and the unsteadiness of the flow is calculated by a linear panel method.

- **TRANSFORMER** (transonic non-entropic formulation of Embraer) is a confidential solver developed by Embraer that aims to correct some of ZTRAN's deficiencies. This approach also corrects the unsteady panel method by means of a steady nonlinear flow solution.

- The unsteady aerodynamic modeling technique based on **dynamic mode interpolation (DMI)** for transonic flutter calculations as presented in Section 4.1.2. For the benchmark wing, the infinite plate spline technique is used to transfer the structural mode shapes onto the wing aerodynamic shape.

5.2 Structural model

The Embraer benchmark wing (EBW) is a generic wing model representing a regional transport aircraft wing [99]. The model has been developed as part of a collaborative research project between Embraer and several international institutions, and it is used as a benchmark for comparing different analysis and optimization methods. Its configuration, aerodynamic shape, structural sizing and mass distribution are realistic.

Several versions of the wing model exist. A simplified version is used for the present analysis. In particular, the stiffness and inertia effects of the pylon and the engine are removed. Moreover, the rotation of the aileron around its hinge line is blocked such that any relative movement with respect to the wing is avoided. Nonetheless, the aileron structure and mass are not removed. The geometry of the benchmark wing is shown in Figure 5.1, and key design parameters are summarized in Table 5.1. Only the untwisted version is used in the following analysis. The thickness of the wing varies over the span. Four profile shapes are defined along the span as shown in Figure 5.1.

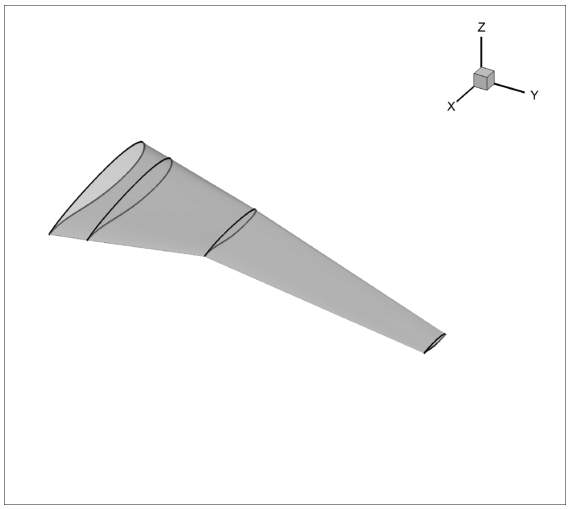

Figure 5.1: Geometry of the benchmark wing.

Parameter	Value
Aspect ratio AR	9.69
Taper ratio	0.28
Leading edge sweep	26.19°
Dihedral angle	5°

Table 5.1: Geometrical parameters of the benchmark wing.

The finite element (FE) model of the benchmark wing constructed using MSC Nastran represents only the internal structure whose geometry is shown in red in Figure 5.2. Although this model is adequate to analyze the structural dynamics, it does not include

the skin and its connection to it. This means that the deformation of the external wing structure that is seen by the flow cannot be readily obtained, and the forces exerted by the flow onto the skin cannot be directly imposed/transferred to the FE model. This precludes a direct application of the wing FE model for fluid-structure interaction (FSI) simulations. Since extending the available FE model to include the wing skin and its connection to the internal structure would be highly complex and would modify the overall dynamics of the structure, a different approach based on a modal description is used here. More specifically, the infinite plate spline (IPS) technique is used to determine the mean plane deformation first, and then the skin displacement is obtained from this mean plane by projection. The IPS technique is presented in the following section.

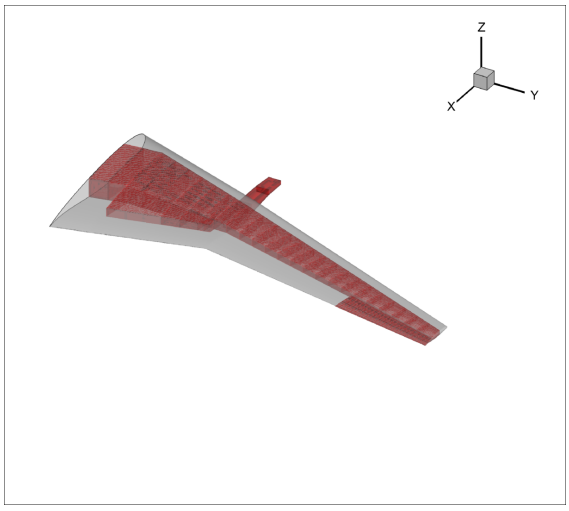

Figure 5.2: The internal structural model of the Embrear benchmark wing (red) and its wing skin (gray).

5.2.1 Infinite plate spline

Aeroelastic analysis requires the coupling of the structural and aerodynamic responses. In the preliminary design stage, the structural model may only represent the internal load-carrying structure while the aerodynamic model considers the external surface of the wing. A method is therefore necessary to transfer the displacements calculated on the structural mesh to the aerodynamic mesh.

The infinite plate spline (IPS) approach is based on the deflection equation of a plate of infinite extent [102]. The method is illustrated here for the interpolation of wing deflections. The differential equation that governs the bending deflections of an infinite plate with uniform thickness can be written as

$$D\nabla^2\nabla^2 W = q, \tag{5.1}$$

where D is the plate rigidity, ∇^2 is the Laplacian, $W(x,y)$ is the plate deflection at a point (x,y), and q is the distributed load on the plate. In the considered problem, the deflections are imposed at N independent points (x_i,y_i), $i \in \{1,2,3,\ldots,N\}$. For example, these deflections can represent the displacements associated with a mode of vibration obtained from the structural finite element model. The method then consists in determining the point loads P_i that must be applied at these N points so that the deformation of the infinite plate satisfies the given deflections. Once the deformation of the infinite plate is known, the deflection at the aerodynamic grid points can be evaluated.

The detailed description of the derivation of the general solution for the deflection is available in Harder and Desmarais [102]. The first step consists in finding the deflection due to a point load. Then, the deflection of the entire surface spline due to N point loads can be inferred. By imposing that the surface spline must become flat very far from the applied loads, the following equation for the deflection can be derived

$$W(x,y) = a_0 + a_1 x + a_2 y + \sum_{i=1}^{N} F_i r_i^2 \ln(r_i^2), \tag{5.2}$$

where $r_i^2 = (x-x_i)^2 + (y-y_i)^2$ and $F_i = P_i/(16\pi D)$. The $N+3$ unknown coefficients a_0, a_1, a_2 and F_i are determined from the discrete force and moment equilibrium equations:

$$\sum_{i=1}^{N} F_i = 0, \tag{5.3}$$

$$\sum_{i=1}^{N} x_i F_i = 0, \tag{5.4}$$

$$\sum_{i=1}^{N} y_i F_i = 0, \tag{5.5}$$

and by forcing the plate to pass through the N specified points:

$$W_j = a_0 + a_1 x_j + a_2 y_j + \sum_{i=1}^{N} F_i r_{ij}^2 \ln(r_{ij}^2), \qquad j \in \{1,2,3,\ldots,N\}, \tag{5.6}$$

where W_j are the given deflections at the N points and $r_{ij}^2 = (x_i - x_j)^2 + (y_i - y_j)^2$. If $i = j$, then $r_{ij} = 0$ and the logarithmic term $\ln(r_{ij}^2)$ does not exist but $\lim_{r\to 0} r_{ij}^2 \ln(r_{ij}^2) = 0$. At least three non-colinear points (x_i,y_i) must be specified to use a surface spline.

The following system of linear equations can be written in matrix form by combining

Equations (5.3) to (5.6):

$$\underbrace{\begin{bmatrix} 0 \\ 0 \\ 0 \\ W_1 \\ W_2 \\ \vdots \\ W_N \end{bmatrix}}_{\mathbf{b}} = \underbrace{\begin{bmatrix} 0 & 0 & 0 & 1 & 1 & \dots & 1 \\ 0 & 0 & 0 & x_1 & x_2 & \dots & x_N \\ 0 & 0 & 0 & y_1 & y_2 & \dots & y_N \\ 1 & x_1 & y_1 & 0 & K_{12} & \dots & K_{1N} \\ 1 & x_2 & y_2 & K_{21} & 0 & \dots & K_{2N} \\ \vdots & \vdots & \vdots & \vdots & \vdots & \ddots & \vdots \\ 1 & x_N & y_N & K_{N1} & K_{N2} & \dots & 0 \end{bmatrix}}_{\mathbf{A}} \underbrace{\begin{bmatrix} a_0 \\ a_1 \\ a_2 \\ F_1 \\ F_2 \\ \vdots \\ F_N \end{bmatrix}}_{\mathbf{x}} . \tag{5.7}$$

where $K_{ij} = r_{ij}^2 \ln(r_{ij}^2)$. The unknowns appearing in the surface spline equation given in Equation (5.2) are grouped in the vector $\mathbf{x}$. The elements on the main diagonal of the matrix $\mathbf{A}$ are all equal to zero. An LU factorization with partial pivoting [103, 104] can be used to solve this system of linear equations.

The IPS method provides displacements along a single direction. The method was first developed to interpolate normal displacements, i.e., the deflection W in Equation (5.1) represents a displacement in the normal direction to the wing plane. However, the IPS method can be applied for computing the displacements along the streamwise and lateral directions in the same way as just presented. In that case, the variable D in Equation (5.1) represents some in-plane flexural rigidity.

In the case of the Embrear benchmark wing, the displacements associated with the mode shapes are obtained on the structural mesh using MSC Nastran. These displacements are then transferred to the mean plane of the wing using the infinite plate spline method. Figure 5.3 illustrates the result of this procedure for the first bending mode. The surface given in Figure 5.3 is used for the unsteady panel method and it covers the whole planform of the wing.

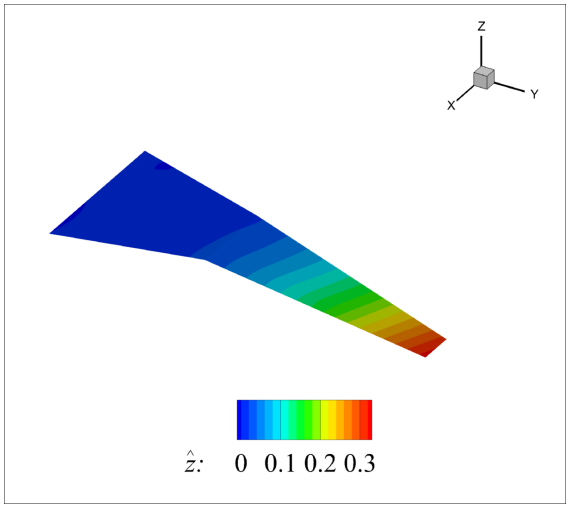

Figure 5.3: Vertical displacement field on the wing mean surface associated with the first bending mode obtained from the internal structure using the infinite plate spline method.

Each modal displacement field on the mean surface of the wing can then be projected on the skin of the wing used for the Euler simulations. As illustrated in Figure 5.4, the displacement at one point on the wing skin is obtained from the closest point on the wing mean surface where the displacement field is known from IPS.

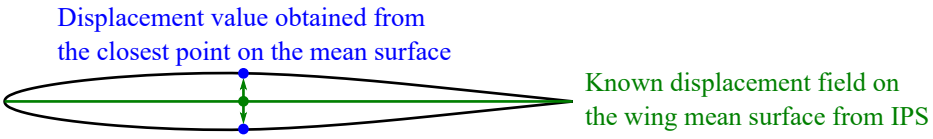

Figure 5.4: Projection of the modal displacements from the wing mean surface to the external surface of the wing.

5.2.2 Modal description for the dynamics of the structure

The first six modes of vibration are considered to represent the structural behavior in the stability analysis as flutter typically appears due to the coupling of the lower order structural modes. Figure 5.5 represents the first six mode shapes for the benchmark wing. The corresponding natural frequencies have been nondimensionalized for confidentiality reasons. The nondimensionalization of a variable is indicated by the asterisk symbol. It can be seen that the wing in-plane mode appears at low frequency, which is not usual

for a more classical metallic wing. In this model, the wing is made of composite materials, which makes it lighter and more flexible than a metallic counterpart, and aeroelastic problems can be critical. The structural matrices are extracted from the FE model.

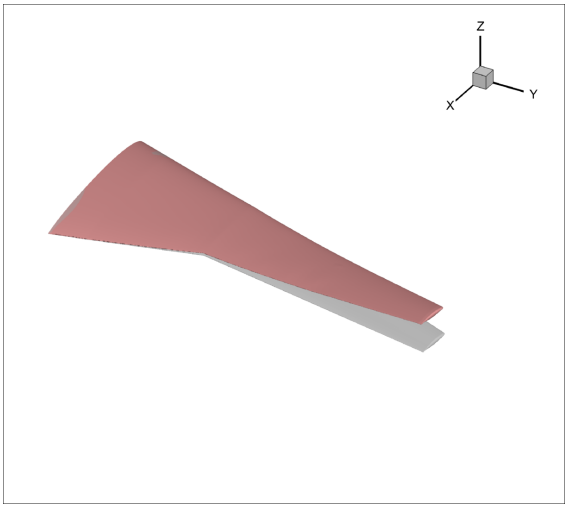

(1) Wing bending ($f^* = 1$)

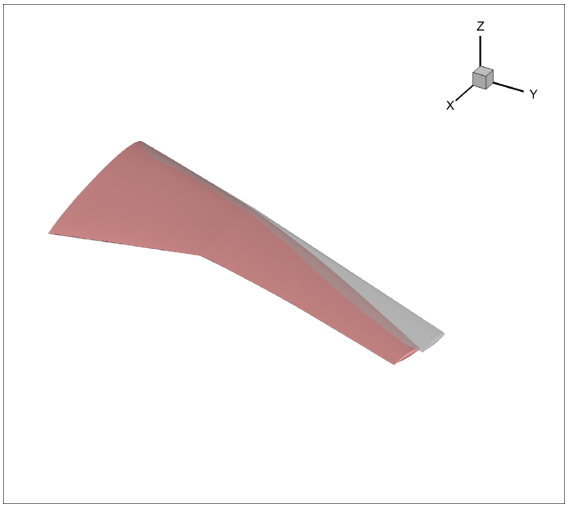

(2) Wing in-plane ($f^* = 2.547$)

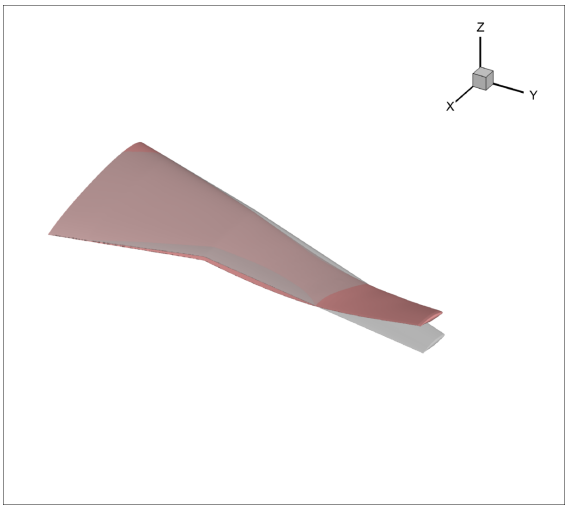

(3) Wing bending with 2 nodes ($f^* = 3.067$)

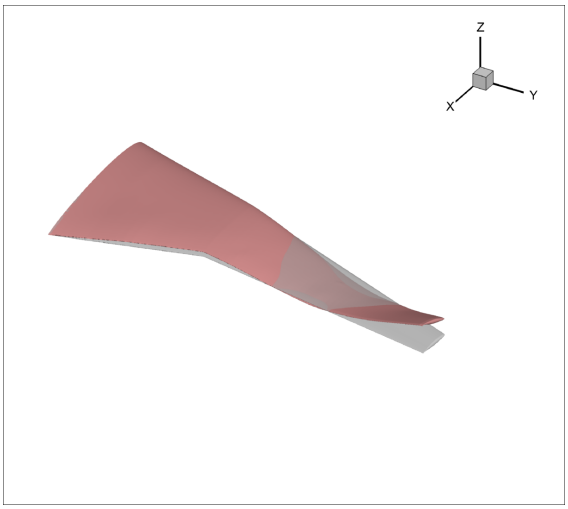

(4) Wing bending with 3 nodes ($f^* = 5.480$)

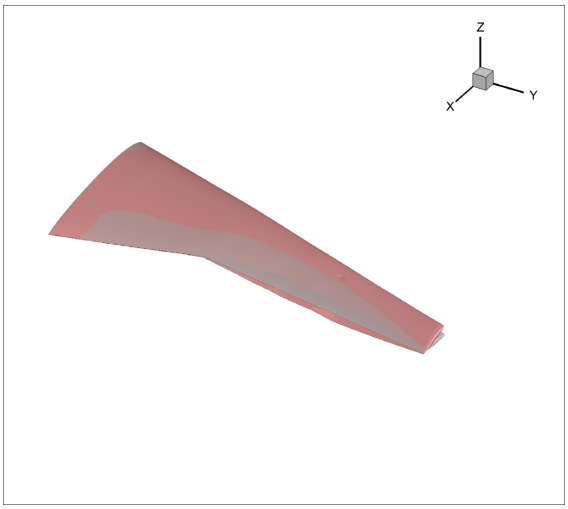

(5) Wing torsion ($f^* = 6.905$)

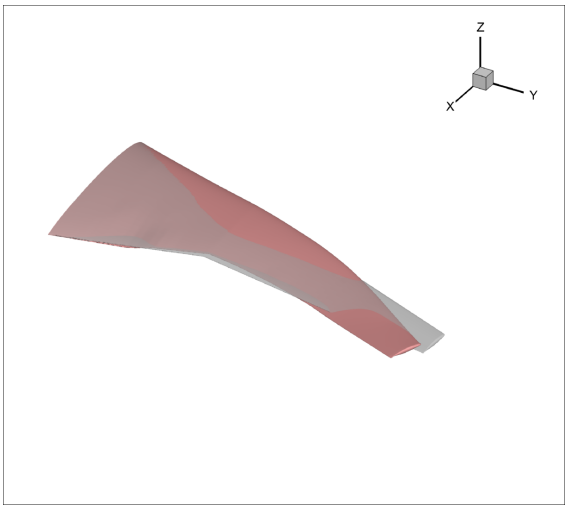

(6) Wing in-plane with 2 nodes ($f^* = 7.351$)

Figure 5.5: First six mode shapes for the benchmark wing.

5.3 Steady pressure distributions

This section presents the steady-state Euler solution, which is required for the ZTRAN and TRANSFORMER approaches. Note that our methodology is based on unsteady simulations and will thus not rely on the following results. The objectives here are to choose the mesh resolution and check the consistency between the solver SU2 used in our methodology and the commercial solver CFD++ used in ZTRAN and TRANSFORMER.

Only Euler simulations are considered in this chapter. The effects of viscosity are therefore not taken into account. The flight condition used to compute the reference nonlinear CFD solutions is given in Table 5.2.

Parameter	**Value**
Altitude	36000 ft $\approx$ 10.97 km
Free-stream Mach number M_∞	0.8
Angle of attack α	0°
Reference length L (half of the chord at $y = 25\%$ semi-span)	$4.143/2$ m
Reynolds number Re based on L	12.586×10^6
Reference area for force coefficients	47.644 m^2

Table 5.2: Flight condition used for the numerical simulations.

The mesh is unstructured, as can be seen in Figure 5.6. The size of the computational domain is 50 times the root chord in order to minimize the impact of the boundaries on the solution in the region of interest. A grid convergence study is carried out to ensure that the resolution is sufficient to provide accurate results. Figure 5.7 shows the steady pressure coefficient C_p field for the static benchmark wing at $M_\infty = 0.8$ and $\alpha = 0^\circ$, which includes a strong shock wave located near the trailing edge of the wing. This flow solution is computed using a first mesh labeled Mesh I and a finer version of this mesh labeled Mesh II. It can be seen that both solutions are similar suggesting that Mesh I is sufficiently fine.

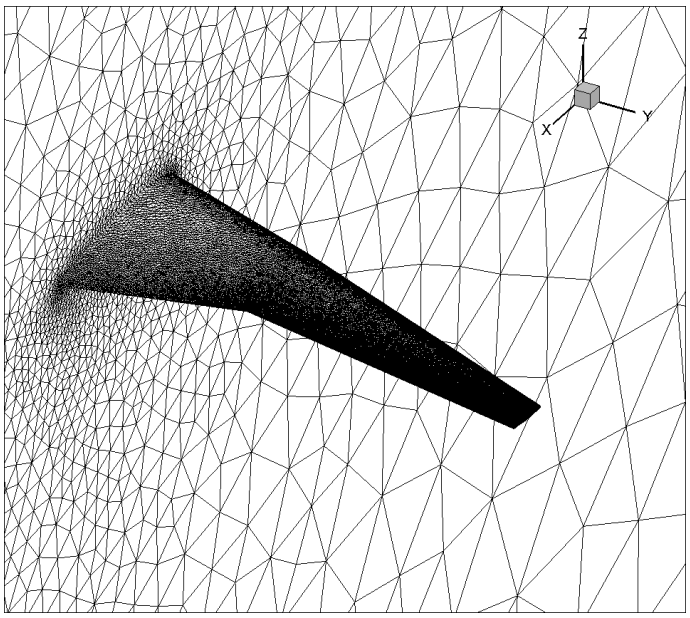

Figure 5.6: Mesh I (354204 tetrahedra) used for Euler simulations.

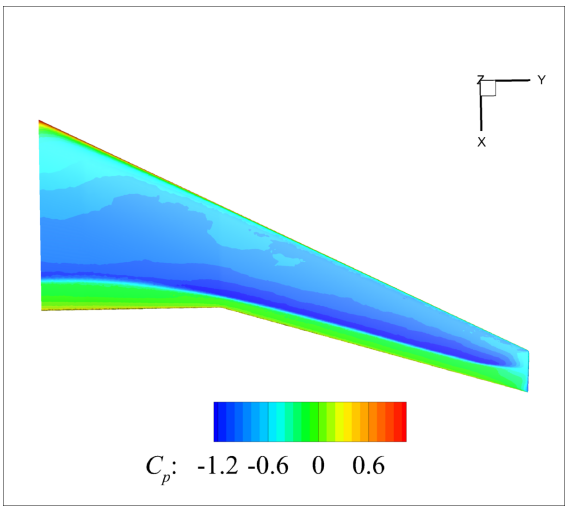

(a) Pressure coefficient field using Mesh I

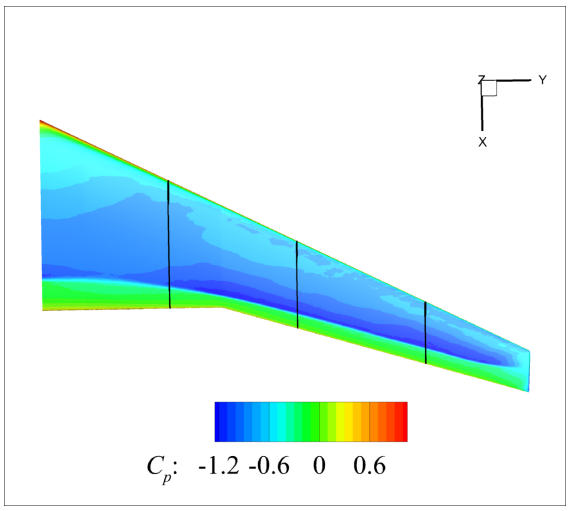

(b) Pressure coefficient field using Mesh II

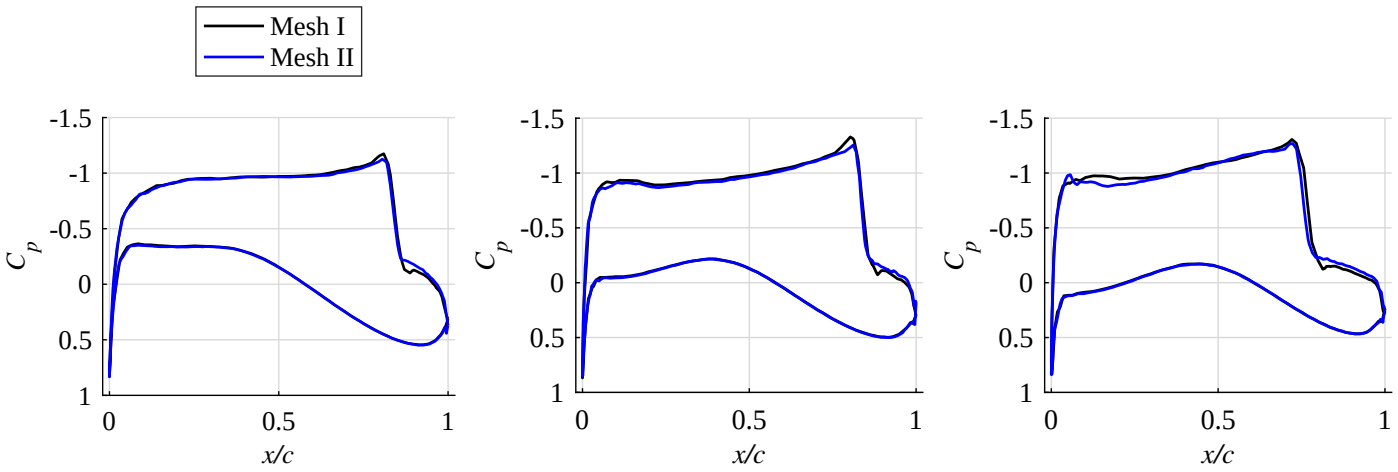

(c) $y = 4$ m (26% semi-span)

(d) $y = 8$ m (53% semi-span)

(e) $y = 12$ m (79% semi-span)

Figure 5.7: Comparison of the pressure coefficient C_p on the benchmark wing at $M_\infty = 0.8$ and $\alpha = 0^\circ$ obtained by steady Euler simulations with two levels of grid refinement. Mesh I contains 354204 tetrahedra and Mesh II contains 668181 tetrahedra.

ZTRAN and TRANSFORMER rely on a steady Euler solution computed with the commercial solver CFD++ using Mesh I. Figure 5.8 demonstrates that the solutions calculated by SU2 and CFD++ are in fair agreement. However, the discrepancy between the two solvers is larger than the difference between Mesh I and II (SU2). Discrepancies are mostly located around the shock, which may be due to the numerical parameters selected for the two different solvers.

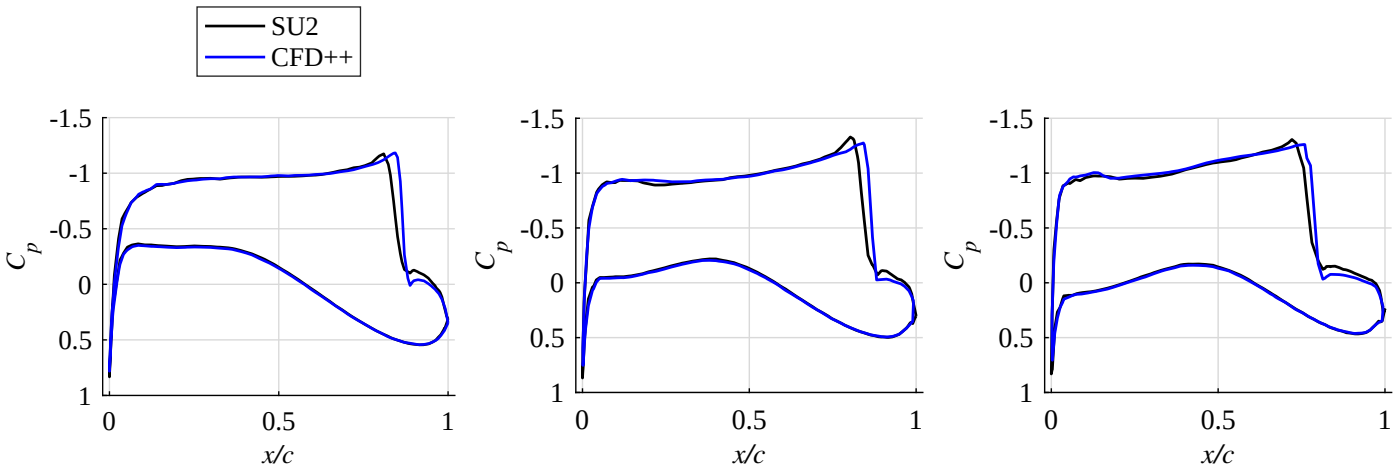

(a) $y = 4$ m (26% semi-span) (b) $y = 8$ m (53% semi-span) (c) $y = 12$ m (79% semi-span)

Figure 5.8: Comparison of the pressure coefficient C_p on the benchmark wing at $M_\infty = 0.8$ and $\alpha = 0^\circ$ obtained by steady Euler simulations computed with SU2 and CFD++ using Mesh I.

5.4 Unsteady pressure distributions

The novel methodology developed in this work requires unsteady Euler simulations to be carried out for the wing in modal motion (see Figure 4.1). A simple harmonic motion is imposed for each mode of vibration. The amplitude of the given modal displacements is set to $16\%L$, where L is the reference length (see Table 5.2), to ensure that the flow behaves linearly with respect to the motion amplitude. This linearity is demonstrated in Figure 5.9. Two nearby forcing reduced frequencies are chosen: $k = \omega L/U_\infty = 0.1$ and 0.3, with the free-stream velocity $U_\infty = 236.22$ m/s for the flow conditions given in Table 5.2. Other tests are also performed by considering two additional reduced frequencies $k = 0.5$ and 0.7 to verify the accuracy of the flutter results.

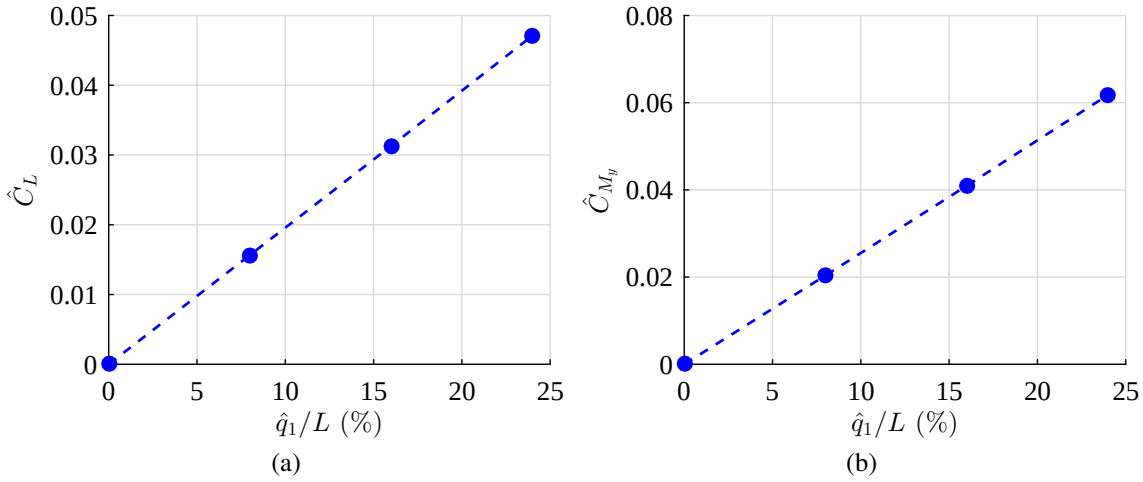

Figure 5.9: Amplitudes of the lift coefficient $\hat{C}_L$ and moment coefficient about the y axis $\hat{C}_{M_y}$ as a function of the amplitude of the bending mode $\hat{q}_1$ for the benchmark wing oscillating at the reduced frequency $k = 0.1$ obtained by unsteady Euler simulations.

The unsteady pressure distributions are compared first. The surface pressure coefficient C_p can be approximated as

$$C_p(x,y,z,t) \approx \bar{C}_p(x,y,z) + \Im\left(\hat{C}_p(x,y,z)\, \mathrm{e}^{i\omega t}\right). \tag{5.8}$$

Figure 5.10 compares the amplitude of the unsteady pressure coefficient difference between the upper and lower surfaces[2] $\Delta\hat{C}_p$ that results from imposing a harmonic deformation corresponding to mode shape 3 for the different levels of fidelity. The first difference appears at the leading edge, which corresponds here to the stagnation point, where only the unsteady Euler solution has a zero unsteady pressure difference. The unsteady panel methods cannot capture this stagnation point because the thickness and the camber line are not modeled.

The ZONA6 linear method does not predict the correct unsteady pressure distribution because the method is not able to capture the shock waves present in the transonic flow regime. On the other hand, the pressure jumps due to shock waves are captured by ZTRAN and TRANSFORMER. However, the real and imaginary parts of the unsteady pressure obtained by these two methods do not match the nonlinear unsteady Euler solution in the shock wave region. ZTRAN and TRANSFORMER are both based on a nonlinear steady flow solution for a static wing that contains static shock waves. Therefore, they do not include nonlinear unsteady pressure information and are not able to accurately calculate the dynamics of the transonic flow. The unsteady Euler model captures the non-

[2]Note that the linear methods such as ZONA6 do not take into account the thickness of the wing and compute the pressure distribution difference between the suction and pressure sides.

linear dynamics of shock waves and is therefore more realistic. ZTRAN tends to overestimate the height of the peak in the shock wave region compared to the higher fidelity Euler solution. TRANSFORMER attenuates the amplitude of these unsteady pressure peaks predicted by ZTRAN.

Significant discrepancies exist for $\Delta\hat{C}_p$ in the shock wave region depending on the location along the span and the reduced frequency as illustrated in the examples of Figures 5.10 and 5.11. Similar behaviors are observed for the other modes of vibration. Differences in the prediction of transonic flutter are therefore expected between the different fidelity levels. The aeroelastic results are discussed in the next section.

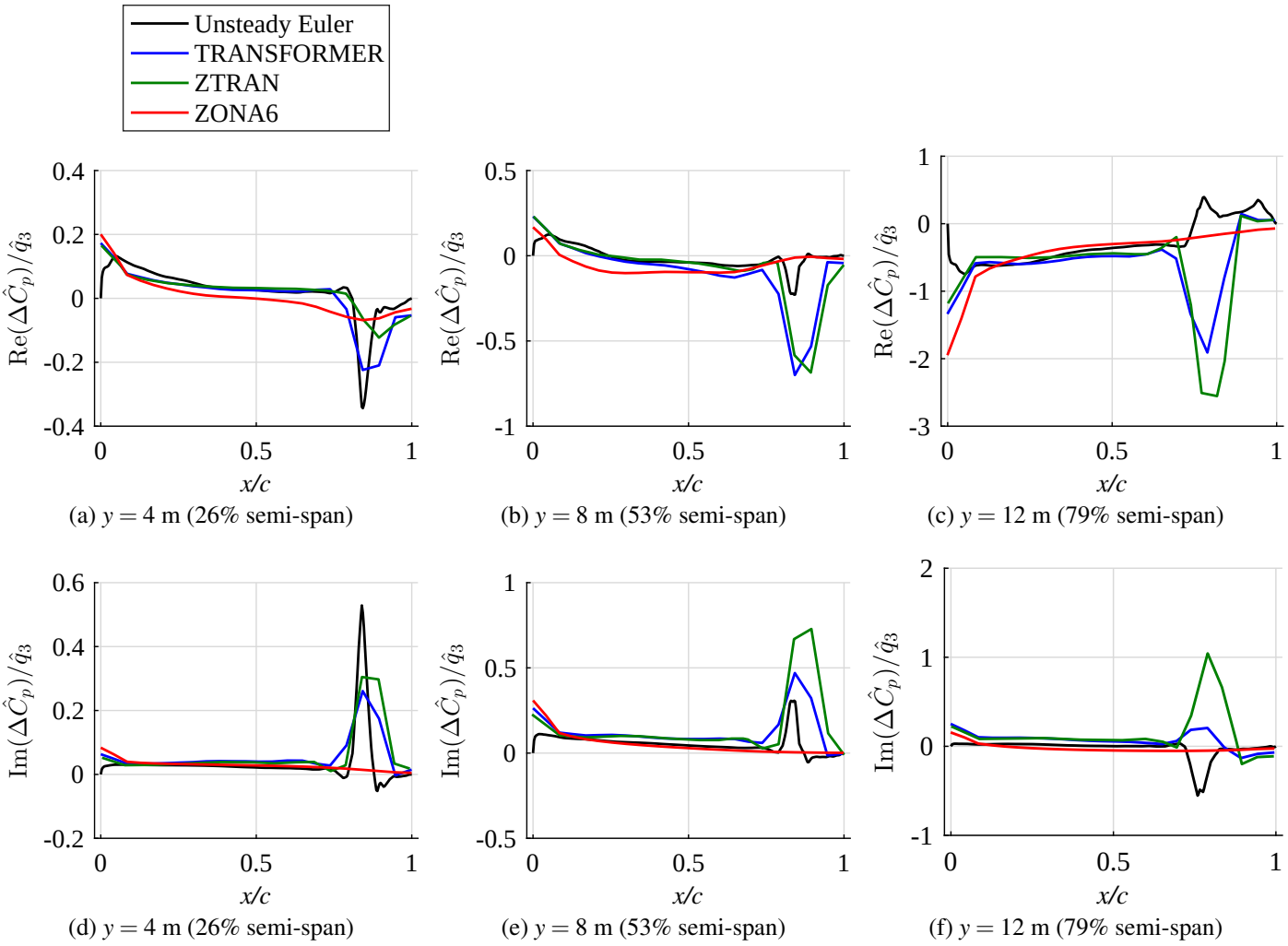

(a) $y = 4$ m (26% semi-span) (b) $y = 8$ m (53% semi-span) (c) $y = 12$ m (79% semi-span)

(d) $y = 4$ m (26% semi-span) (e) $y = 8$ m (53% semi-span) (f) $y = 12$ m (79% semi-span)

Figure 5.10: Amplitude of the unsteady pressure coefficient difference between the upper and lower surfaces $\Delta\hat{C}_p$ at three spanwise locations on the benchmark wing that results from imposing a harmonic deformation corresponding to mode shape 3 at $M_\infty = 0.8$ and $k = 0.1$. The values are normalized by the amplitude of the motion $\hat{q}_3$.

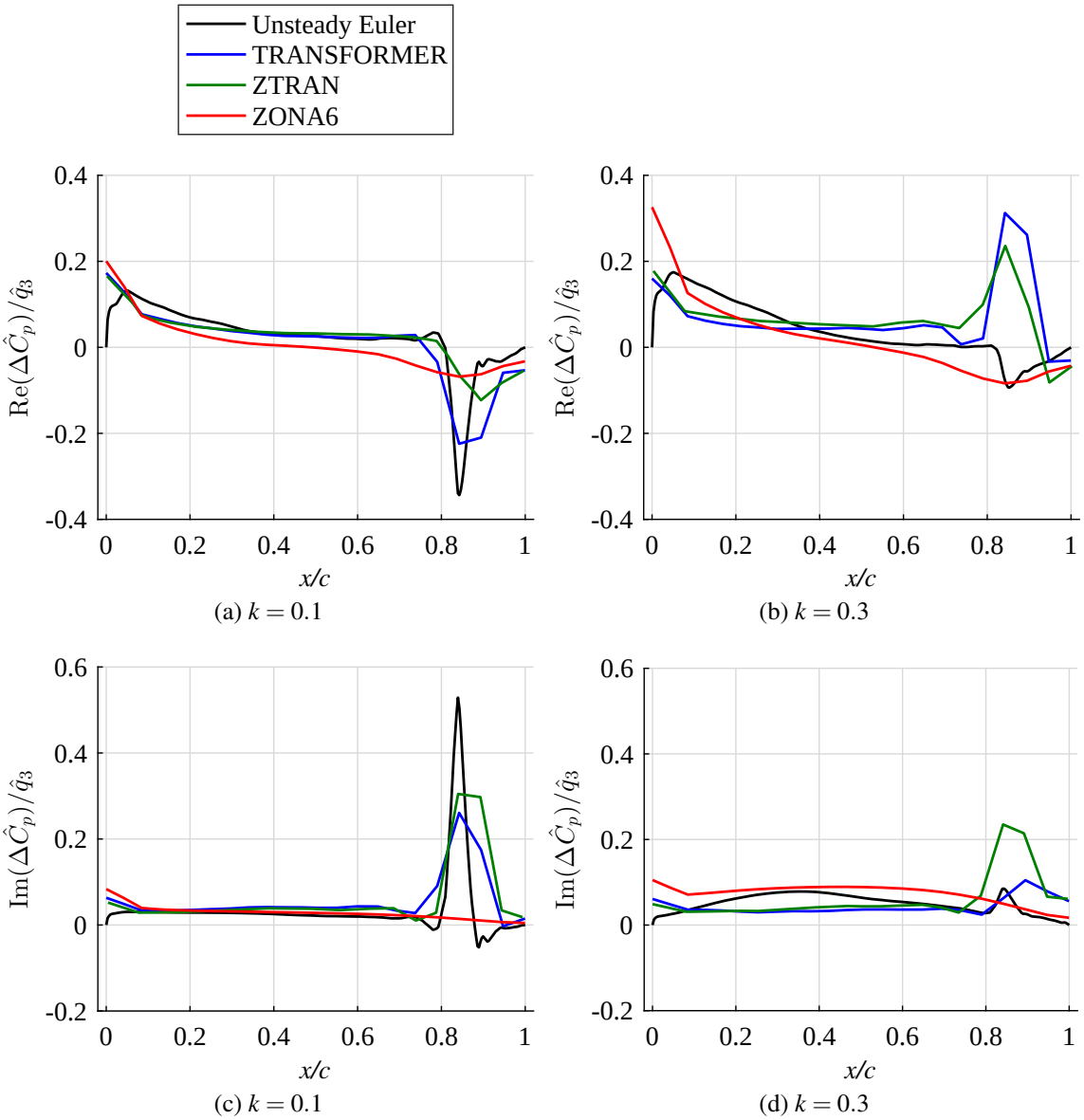

(a) $k = 0.1$ (b) $k = 0.3$

(c) $k = 0.1$ (d) $k = 0.3$

Figure 5.11: Amplitude of the unsteady pressure coefficient difference between the upper and lower surfaces $\Delta\hat{C}_p$ at $y = 4$ m (26% semi-span) on the benchmark wing that results from imposing a harmonic deformation corresponding to mode shape 3 at $M_\infty = 0.8$ and two reduced frequencies: $k = 0.1$ and 0.3. The values are normalized by the amplitude of the motion $\hat{q}_3$.

It should be noted that in these transonic conditions, the time-averaged flow around the benchmark wing with an imposed motion is different from the steady flow obtained at the mean position of the wing, as confirmed in Figure 5.12. This discrepancy affects the accuracy of the methods relying on the TLTSD approximation (ZTRAN and TRANSFORMER) and would also affect the linear frequency domain method described in Section 2.6. Indeed, these methods rely on a steady-state simulation performed at the mean position of the structure to predict the unsteady transonic flow.

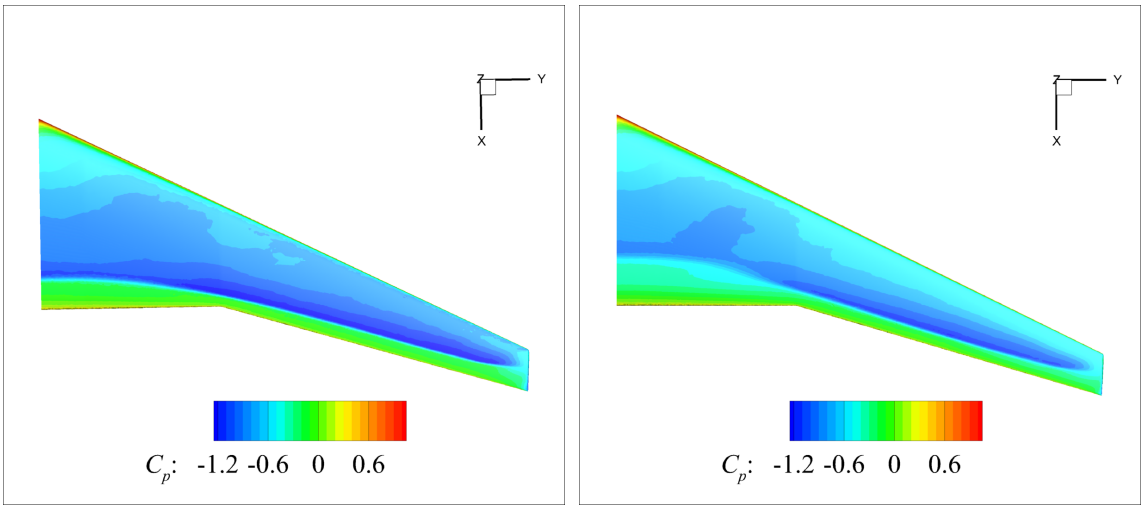

(a) (b)

Figure 5.12: Comparison between (a) the pressure coefficient on the benchmark wing at $M_\infty = 0.8$ and $\alpha = 0^\circ$ obtained by a steady Euler simulation and (b) the average of the unsteady pressure coefficient resulting from a forced torsional deformation at $k = 0.1$.

5.5 Aeroelastic stability analysis

This section investigates the impact of the discrepancies in the unsteady pressure distributions between the different levels of fidelity on the aeroelastic stability of the wing. The data of interest are the flutter onset speed and the associated flutter frequency, which can be identified by the *p-k* method as explained in Section 4.1.3. The difference between the different levels of fidelity lies in the computation of the modal aerodynamic force matrix in the frequency domain $\mathbf{Q}(ik)$.

In the aeroelastic configurations analyzed in Chapter 3, a mass ratio was imposed by the experiment and this parameter imposed a condition for the free-stream density ρ_∞. In the following aeroelastic stability analysis, the air density ρ_∞ and airspeed U_∞ vary so as to satisfy the given Mach number $M_\infty = 0.8$ in a standard atmosphere. The NASA standard atmosphere model [105] is used to specify the variation of properties. The model assumes

that the temperature and pressure depend only on the altitude h where $h = 0$ represents the sea level:

- In the troposphere ($h < 11000$ m), the temperature T decreases linearly with the altitude and the pressure p decreases exponentially:

$$T = 288.19 - 0.00649\,h, \tag{5.9}$$

$$p = 101290\left(\frac{T}{288.08}\right)^{5.256}. \tag{5.10}$$

  In these expressions, the altitude is given in meters, the temperature in Kelvin and the pressure in Pascal.

- In the lower stratosphere (11000 m $< h < 25000$ m), the temperature remains constant and the pressure decreases exponentially:

$$T = 216.69, \tag{5.11}$$

$$p = 22650\,\mathrm{e}^{(1.73-0.000157h)}. \tag{5.12}$$

Figure 5.13 shows the evolution of the temperature and pressure in the atmosphere.

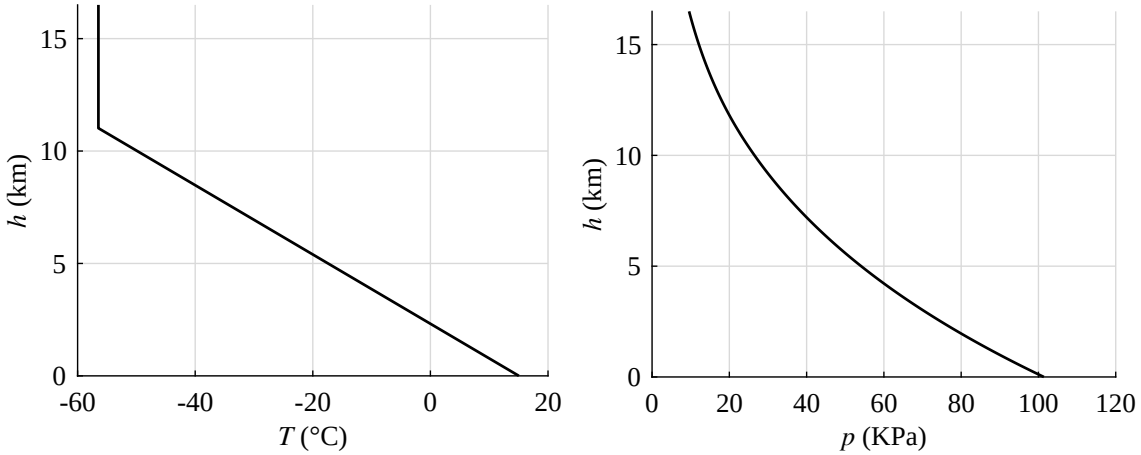

(a) Temperature (b) Pressure

Figure 5.13: Variation of the temperature T and pressure p as a function of the altitude h for a standard atmosphere model.

Assuming a standard atmosphere, there is only one degree of freedom. Varying U_∞ and using the Mach number gives the speed of sound, thus the temperature. Having the temperature leads to the altitude using the standard atmosphere model, and therefore to the pressure. Finally, the density is obtained from the perfect gas law. In the following

graphs, the results are presented in terms of equivalent airspeed defined as

$$\mathrm{EAS} = U_\infty \sqrt{\frac{\rho}{\rho_0}}, \tag{5.13}$$

with the standard sea level density $\rho_0 = 1.225\ \mathrm{kg/m^3}$. The EAS values are then expressed in knots (1 kn $\approx$ 0.5144 m/s).

Following industrial practice, the density and velocity curves are extrapolated to negative values of the altitude h resulting in large values of the equivalent airspeed. These large values of EAS do not correspond to physical flight conditions, but they are nonetheless included in the analysis so as to estimate where flutter would occur. The considered range of values for ρ_∞ and U_∞ is shown in Figure 5.14.

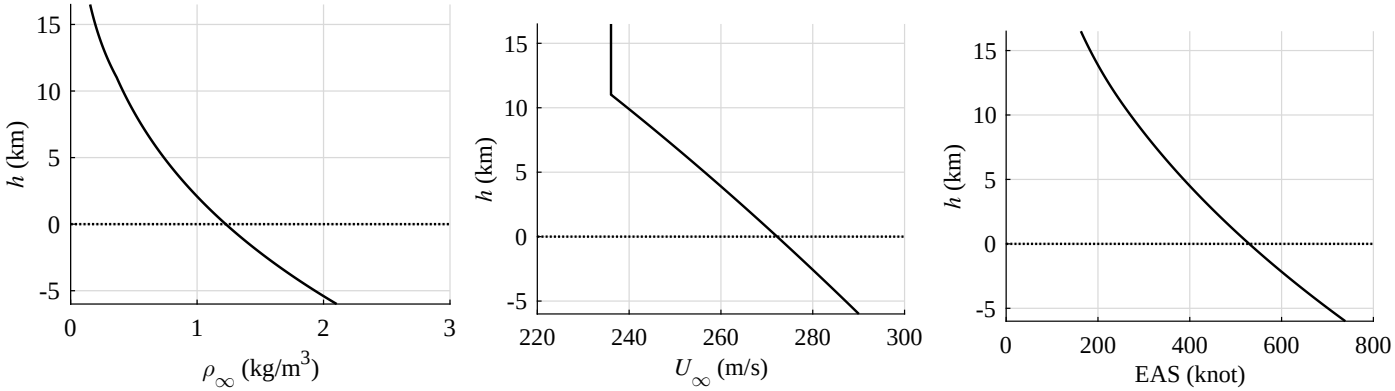

(a) Density (b) Airspeed ($M_\infty = 0.8$) (c) Equivalent airspeed ($M_\infty = 0.8$)

Figure 5.14: Variation of (a) the density ρ_∞, (b) the airspeed U_∞ and (c) the equivalent airspeed EAS as a function of the altitude h at a Mach number $M_\infty = 0.8$ for a standard atmosphere model.

Figure 5.15 presents the aeroelastic stability analysis obtained by the DMI-based aeroelastic methodology relying on different sets of reference reduced frequencies. The case based on four reference reduced frequencies ($k = 0.1, 0.3, 0.5$ and 0.7) covers a large range of reduced frequencies that includes all frequencies of the first six modes of the system. The flutter instability appears at EAS = 713 kn, where the damping coefficient of the first bending mode vanishes. The corresponding flutter reduced frequency is $k = 0.21$. Figure 5.15a also shows that the frequencies associated with the in-plane modes remain constant indicating that these modes do not interact with other modes. Therefore, the in-plane modes are not involved in the flutter mechanism and can be neglected.

Relying on two nearby forcing reduced frequencies $k = 0.1$ and 0.3 implies an extrapolation for the higher frequency modes, but the flutter mode and speed are still correctly predicted. However, the damping evolution of the higher modes is estimated with less precision due to extrapolation errors. The choice of the reference reduced frequencies

requires a compromise between accuracy and computational cost.

Figure 5.15b also points out that using our methodology based on dynamic mode interpolation between two reference reduced frequencies that are too far apart (e.g., $k = 0.1$ and 0.7) should be avoided as it affects the damping of the first modes and compromises the prediction of the flutter instability. The error is due to the fact that a linear variation of the flow dynamic modes is assumed over a wide range of k. For a reliable flutter prediction, the important thing is not to assume that the variation is linear with k over a wide k range.

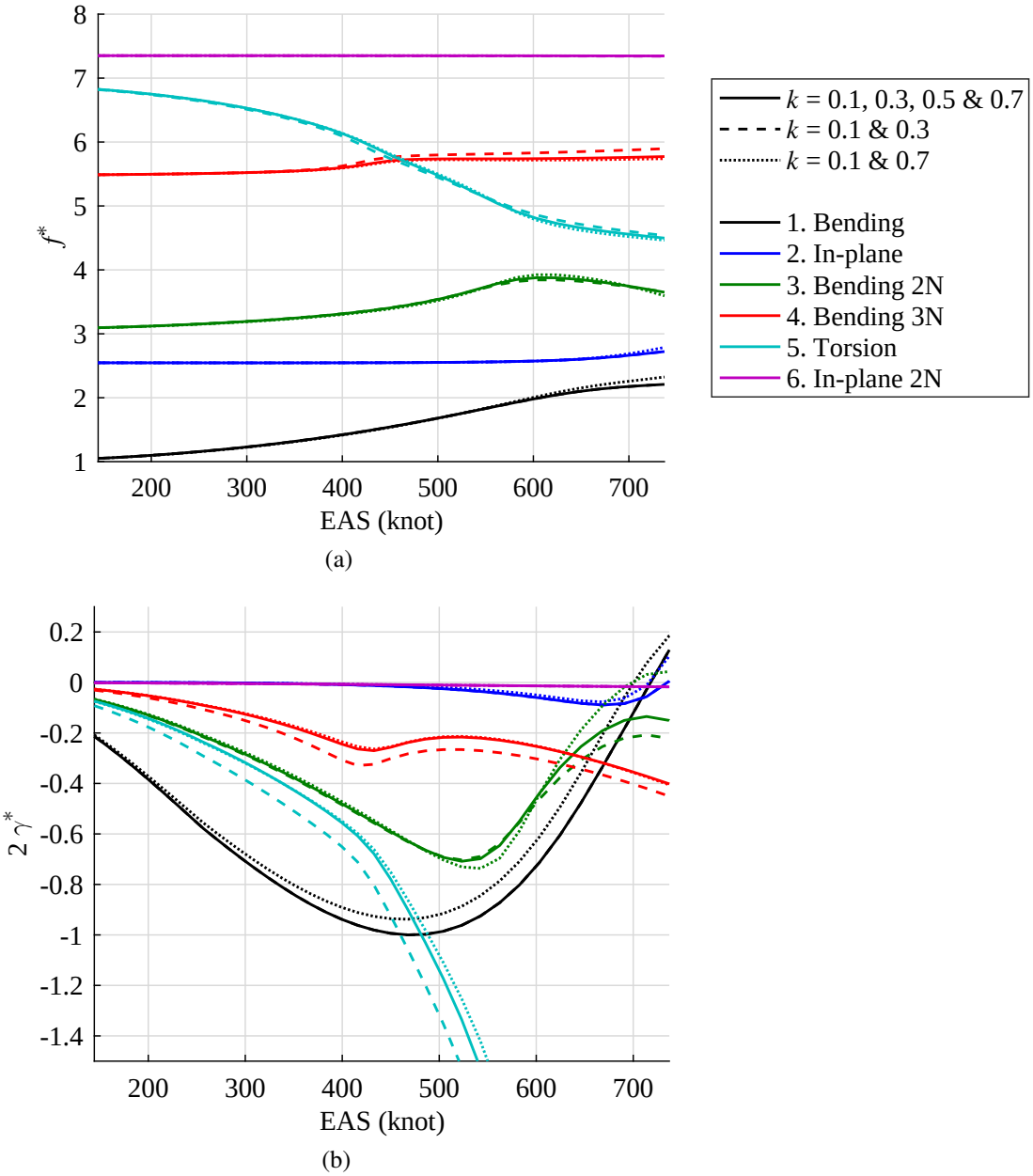

Figure 5.15: Evolution of the non-dimensional frequency f^* and the non-dimensional damping coefficient γ^* associated with each mode of vibration of the benchmark wing as a function of the equivalent airspeed for a matched-point flutter analysis at $M_\infty = 0.8$ obtained by the DMI-based aeroelastic methodology relying on different sets of reference reduced frequencies.

The four different levels of fidelity predict very different flutter behaviors as can be seen in Figure 5.16. This was expected because the unsteady pressure distributions have been shown to significantly differ. Note that for clarity, the in-plane modes, which are not involved in the flutter mechanism, are not shown in the figure. The lowest flutter

equivalent airspeed is predicted by ZTRAN at EAS = 468 knots and $k = 0.61$. The flutter mechanism corresponds to a coupling between the bending with three nodes mode and the torsion mode. The flutter mechanism obtained by ZONA6 involves the second bending mode and the torsion mode, and it appears at EAS = 583 knots and $k = 0.37$. For the DMI-based methodology, the damping associated with the first bending mode becomes zero at EAS = 713 knots and $k = 0.21$. The flutter mode predicted by TRANSFORMER is also the first bending mode, but the flutter onset appears at a higher equivalent airspeed EAS = 762 knots (extrapolated value[3]).

ZTRAN and TRANSFORMER predict very different flutter solutions, even though they rely on the same nonlinear steady flowfield computed by the solver CFD++. The unsteady panel method ZONA6 predicts a lower flutter equivalent airspeed than the DMI-based methodology and TRANSFORMER despite the fact that ZONA6 does not take into account aerodynamic nonlinearities. This result is not usual in the transonic flow regime and may be particular to this structural model.

In addition to the wide range of flutter speeds, the flutter mode predicted by the four different methods is not always the same. The DMI-based methodology provides more accurate results than the others because it computes the unsteady nonlinear dynamics of the shock waves. This is demonstrated in Section 5.5.2 where the flutter results obtained with the DMI-based methodology are validated with full FSI simulations.

[3]This result has been provided by Embraer so that we cannot compute the exact flutter speed ourselves.

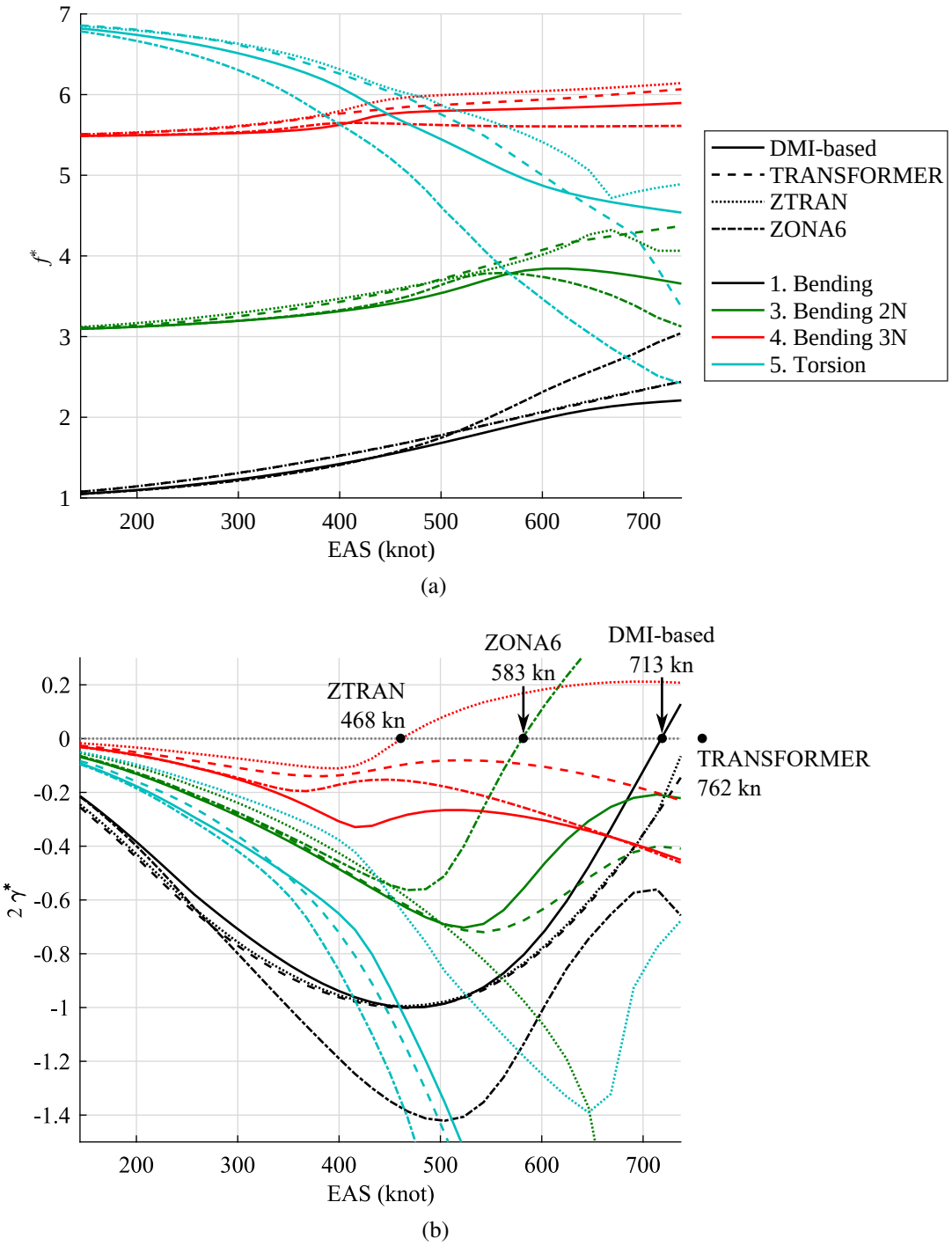

Figure 5.16: Evolution of the non-dimensional frequency f^* and the non-dimensional damping coefficient γ^* associated with each mode of vibration of the benchmark wing as a function of the equivalent airspeed for a matched-point flutter analysis at $M_\infty = 0.8$ obtained by four different levels of fidelity.

The aeroelastic stability analysis of Figure 5.16 is performed around the undeformed wing as the structural model is linearized around this undeformed shape. The following section considers the fact that the wing can deform depending on the flight condition and investigates the influence of this deformation on the flutter prediction.

5.5.1 Influence of the wing equilibrium shape

The flight condition at which flutter is predicted by the DMI-based methodology (EAS = 718 kn) is very far from the reference condition given in Table 5.2 (EAS = 251 kn) for which the wing has been designed. In addition, the benchmark wing made of composite materials is more flexible than the AGARD 445.6 wing studied in Section 4.3. This results in a large static deformation for such high equivalent airspeed. Figure 5.17 shows that the equilibrium shape of the benchmark wing at EAS = 737 kn significantly differs from the original shape of the wing[4]. Note that structural nonlinearities would occur for such large structural deflection, but the consideration of these nonlinearities goes beyond the scope of this thesis.

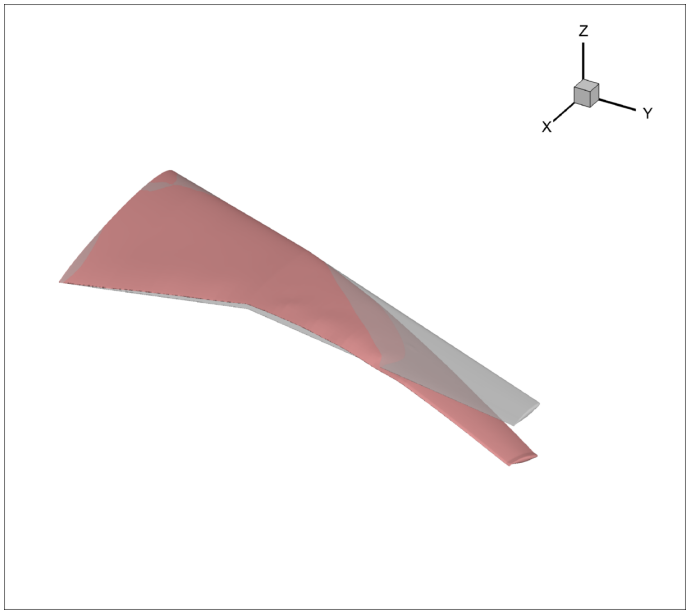

Figure 5.17: Equilibrium shape of the wing at EAS = 737 knots represented in red and undeformed shape of the wing represented in gray.

The present methodology for flutter analysis is based on nonlinear unsteady Euler simulations with imposed wing motion. Therefore, imposing small amplitude periodic deformations around the equilibrium shape of the wing at EAS = 737 kn instead of the undeformed wing modifies the location and dynamics of the shock waves and therefore

[4]The equivalent airspeed EAS = 737 kn is higher than the computed flutter equivalent airspeed, but the wing is still stable. The reason is explained in the following.

the unsteady pressure distributions. The flutter point will thus also be impacted by the static deformation of the wing. Figure 5.18 shows that considering the static deformation not only changes the flutter speed from 713 kn to 749 kn, but also the flutter mode from the first bending mode to the second bending mode.

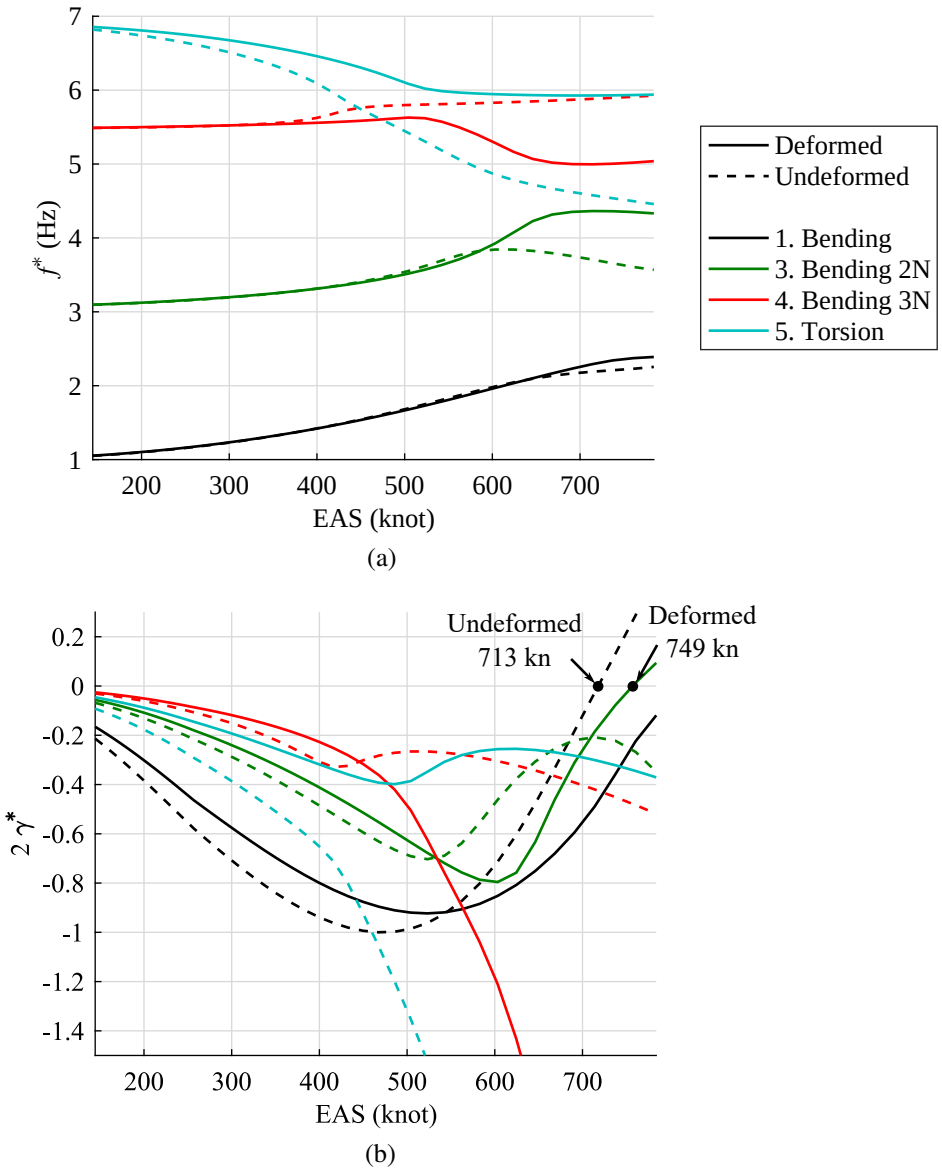

Figure 5.18: Flutter results obtained by the DMI-based methodology with the modal displacements applied to the deformed wing shape at EAS = 737 knots. The results based on the undeformed wing shape are also shown for comparison.

The DMI-based, TRANSFORMER and ZTRAN methods are all based on a nonlinear aerodynamic model and one of their limitations is that the analysis is performed around a given wing shape due to the linearization of the structural model around this shape as explained in Section 4.1. Therefore, if the predicted flutter point is far from the design

condition, the static deformation of the wing can be large and affect the flutter prediction, especially for flexible composite wings. Additional flutter calculations must thus be performed considering the deformed shape of the wing, which increases the computational cost.

In the aeroelastic analysis of Figure 5.16, all levels of fidelity are based on the original shape of the wing. The comparison is thus coherent. Since all the aeroelastic solvers provide different flutter predictions, time-accurate FSI simulations based on the unsteady Euler equations coupled with a modal structural model are performed to ensure that the DMI-based methodology actually gives accurate results. The flutter speed predicted from these time-accurate FSI simulations is the correct flutter speed for an inviscid flow model. The FSI calculations will correspond to flutter around the deformed wing and thus cannot be compared to the results based on the undeformed wing. The validation is presented in the next section.

5.5.2 Validation of the flutter predictions

The flutter results are validated by solving the FSI coupled problem. The FSI tool CUPyDO is used to couple existing independent fluid and structural solvers [95, 106]. CUPyDO features a strong coupling scheme for time-accurate FSI simulations based on a block-Gauss-Seidel (BGS) algorithm. The tool is also capable of treating non-matching meshes between the fluid and structure domains and is optimized to work in parallel using message passing interface (MPI). In the present work, the open-source code SU2 is used to solve the Euler equations for the fluid part while an in-house modal solver is used for the structure.

The modal aeroelastic equations of motion given in Equation (4.10) are rewritten as a system of first-order ordinary differential equations (ODEs) by making the substitution $\dot{\mathbf{q}}(t) = \mathbf{y}(t)$. The resulting system of first-order ODEs is

$$\begin{cases} \dot{\mathbf{q}}(t) = \mathbf{y}(t), \\ \dot{\mathbf{y}}(t) = \mathbf{M}_q^{-1} \left(-\mathbf{C}_q \mathbf{y}(t) - \mathbf{K}_\mathbf{q} \mathbf{q}(t) + \mathbf{f}_q(t) \right). \end{cases} \tag{5.14}$$

The solution of this system of equations requires initial conditions for the modal displacements and velocities, $\mathbf{q}$ and $\dot{\mathbf{q}}$. For a position of the wing at a given time instance, the CFD code SU2 computes the aerodynamic forces acting on the wing. These aerodynamic forces are transferred to the modal structural model to update the position of the wing for the next time step. The procedure is then repeated until the end of the simulation. The modal solver uses the explicit Runge-Kutta method proposed by Dormand and Prince [107] for the time integration. The idea is then to perturb the wing and simulate its response in time to see how it evolves. If the deformation tends to be damped, then the

flight condition is below the flutter point. On the other hand, if the initial perturbation of the wing increases over time, then the flutter point has been exceeded. This approach has been validated using the AGARD 445.6 wing as shown in Appendix A.

Figure 5.19 shows the evolution of the responses over time for the Embraer benchmark wing at three different equivalent airspeeds. An initial bending of amplitude $16\%L$ is imposed to start each simulation. It can be seen that the initial perturbation decays in time at EAS = 737 kn. The system is therefore stable. The response is still damped at EAS = 745 kn but the decay rate is lower than the solution at EAS = 737 kn. In the damped cases, the solution converges to the static deformed wing solution. The response is unstable at EAS = 750 kn. By refining the interval of equivalent airspeeds, we find that the flutter point predicted by the time-domain FSI simulations is at about EAS = 750 kn. Therefore, there is a discrepancy of about 1 kn between the exact flutter equivalent airspeed (EAS = 750 kn) and the solution predicted by the DMI-based aeroelastic methodology taking into account the static deformation of the wing[5] (EAS = 749 kn). This comparison validates the flutter solutions obtained with the DMI-based method.

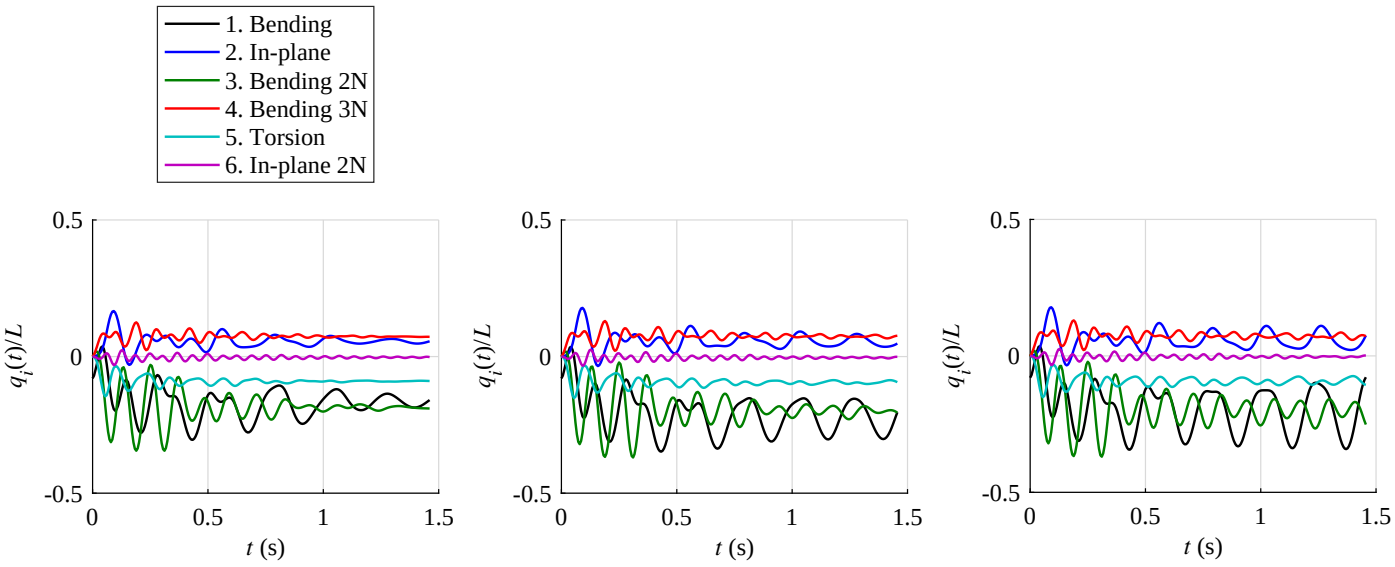

(a) Damped response at EAS = 737 kn (b) Damped response at EAS = 745 kn (c) Unstable response at EAS = 750 kn

Figure 5.19: Aeroelastic responses of the benchmark wing for three equivalent airspeeds at a free-stream Mach number $M_\infty = 0.8$ obtained by solving the modal aeroelastic equations of motion based on the Euler model. The initial conditions are $\mathbf{q}(0) = [-16\%L, 0, 0, 0, 0, 0]^\intercal$ and $\dot{\mathbf{q}}(0) = \mathbf{0}$.

[5]Note that with the DMI-based aeroelastic methodology, the flutter speed of 749 kn has been calculated from a deformed shape at 737 kn. For the highest possible accuracy, the flutter point should be evaluated from 749 kn and iterated until convergence (i.e., the airspeed of the deformed shape is equal to the flutter speed).

5.5.3 Computation time

The DMI-based aeroelastic prediction technique is more accurate than the industrial methods considered here while being computationally tractable. The computational cost depends on the number of structural modes retained in the analysis and the number of reference forcing frequencies as indicated in Table 5.3. For the flutter analysis of the benchmark wing, four structural modes (excluding the in-plane modes) and two reference frequencies were sufficient to achieve a level of precision comparable to that obtained by time-accurate FSI simulations, and the computation time is about 34 hours on 16 cores. In contrast, each time-accurate FSI simulation runs for about 1 day on 16 cores in order to determine the evolution of the system response. The required number of time-accurate simulations to accurately determine the flutter speed is not known a priori. In this case, six simulations were performed and the total FSI time is approximately six days.

Table 5.3 underlines that there is inevitably a trade-off between numerical cost and accuracy as the unsteady panel methods remain much faster than the DMI-based methodology. Note that an open-source CFD solver has been used in this work. The use of a commercial solver should reduce the CPU time of the DMI-based methodology. Moreover, a harmonic balance method could be used to obtain the reference flow fields in our methodology, which could further reduce the computational cost. In addition, the methodology is data-based so that the reference flow fields may also be generated by an unsteady full potential solver, which should reduce the computation time compared to an unsteady Euler solver while capturing the moving shock waves with better accuracy than the considered industrial methods.

Level of fidelity	**Computation time**
DMI-based	4.24 hrs (unsteady Euler) $\times$ 4 (nb of modes) $\times$ 2 (nb of frequencies) = 33.92 hrs on 16 cores
TRANSFORMER	1.53 hrs on 16 cores (steady Euler) + 3.20 hrs on 1 core
ZTRAN	1.53 hrs on 16 cores (steady Euler) + 3.14 hrs on 1 core
ZONA6	8.82 min on 1 core

Table 5.3: Computation time for the aeroelastic stability analysis. The DMI-based methodology is performed in parallel using two Intel E5-2650 processors[6] with 8 cores at 2.0 GHz.

[6]Computational resources have been provided by the Consortium des Équipements de Calcul Intensif (CÉCI), funded by the Fonds de la Recherche Scientifique de Belgique (F.R.S.-FNRS) under Grant No. 2.5020.11 and by the Walloon Region.

5.6 Concluding remarks

The aerodynamic modeling methodology based on dynamic mode interpolation can be applied to a realistic wing even if the structural model represents only the internal structure. The infinite plate spline technique can indeed be used to obtain the structural mode shapes on the CFD geometry required for the reference unsteady Euler simulations.

The unsteady pressure distributions computed by the different levels of fidelity present significant differences, especially in the shock wave region. These discrepancies in the prediction of moving shock waves have a significant impact on the predicted flutter characteristics (flutter speed, mode and frequency). The present methodology leads to accurate results because it better captures the nonlinear shock dynamics over a range of frequencies.

Time-accurate FSI simulations of the composite benchmark wing demonstrate that the static deformation of the wing can be large for a flight condition that is far from the reference condition for which the wing has been designed. The flutter speed and mechanism depend on this deformation of the wing. If the static deformation around the flutter condition is considered in the DMI-based calculations, the predicted flutter point is in agreement with that obtained by time-accurate FSI simulations, which validates our flutter results. For this system, not taking the deformed shape into account provides a conservative estimate but it is not known if this is a general phenomenon. In practice, if the predicted flutter point is far from the reference condition, additional flutter calculations must therefore be carried out taking into account the deformed shape of the wing, which increases the computational cost but provides accurate flutter solutions.

Another important challenge with flexible composite wings is that if large deformations occur, the structural characteristics of the model will change. In this work, we did not take into account this modification of the structural properties as the main goal was to validate our aerodynamic model.

Chapter 6

Conclusions

6.1 Summary

A novel unsteady aerodynamic modeling methodology has been developed for aeroelastic stability analysis of aircraft wings in transonic flow. The basis of this method is the fast computation of the flow response to relatively small amplitude periodic deformations of a wing over a range of oscillation frequencies in the transonic flow regime for an early stage in the design process. First, the most important structural modes are selected. Then, unsteady Euler or RANS simulations are carried out where the motion of the wing is imposed based on these retained structural modes for a few selected frequencies. The unsteady solutions for these given structural modes and frequencies are processed using dynamic mode decomposition (DMD) in order to extract the most dominant dynamic modes. This work has shown that the first dynamic mode, which is the one corresponding to the frequency imposed in the simulation, contributes the most to the flow dynamics and its mode shape changes progressively with frequency. The main idea of the methodology is then to estimate the flow response at any frequency by interpolating these dominant flow dynamic modes obtained at the selected frequencies.

The complete flow dynamics resulting from small amplitude simple harmonic motions can be accurately estimated over a range of frequencies by interpolating from the most dominant modes at just two nearby frequencies, provided that the frequency of interest is not too far from the reference frequencies. Furthermore, relying on the Euler and RANS levels of fidelity makes it possible to take into account moving shock waves and provides unsteady aerodynamic loads on the wing that match well with experimental measurements of high Reynolds number attached transonic flows. In practice, the flow around the wings of transport aircraft is essentially attached close to design flight conditions. Any possible separated flow region would be small in extent and would not have a significant impact on the global flow dynamics.

The proposed dynamic mode interpolation (DMI) methodology is suitable for flutter

analysis that involves small perturbations of the structure so that a linearization of the aerodynamic loads with respect to the deformation amplitude is possible. The methodology based on only two reference frequencies provides a very good estimate of the flutter boundary (flutter speed versus Mach number) for the 2D Isogai airfoil and 3D AGARD 445.6 wing models, but at a lower computational cost than the traditional time-accurate fluid-structure interaction (FSI) simulations. The methodology has been used to highlight that flow nonlinearities such as shock motion and boundary layer thickness can have a significant impact on the aeroelastic behavior:

- A sharp decrease in the flutter speed exists for certain flow conditions in the transonic flow regime. This well-known transonic dip phenomenon caused by the moving shock waves is properly captured by the proposed methodology. Linear aerodynamic approaches (e.g., DLM) commonly used in aircraft design generally overestimate the flutter speed in the transonic flow regime as they fail to capture the occurrence of shock waves.

- The methodology based on RANS modeling includes viscous effects such as the thickening of the boundary layer, shock-boundary layer interaction and flow separation. Relying on the inviscid Euler equations yields a more conservative flutter boundary in the transonic flow regime compared to viscous solutions based on the RANS equations. As the Reynolds number decreases, the thickness of the boundary layer increases and the transonic dip becomes less severe compared to the inviscid case.

- In the case of a soft flutter characterized by a gradual decrease of the critical damping of the system with airspeed, the system can become stable again beyond the flutter speed as observed in the Isogai wing section model with an inviscid flow modeling. This second stable region and the resulting multiple flutter points are directly captured by the methodology from the variation of the system damping ratios as a function of the airspeed.

The DMI-based aeroelastic methodology was then used to calculate the flutter of a realistic composite wing model. The results were compared to the predictions of different methods that are typically used in the aerospace industry based on the linearized potential equation or the time-linearized transonic small disturbance (TLTSD) equation. The study demonstrates that there is a very wide range of flutter speed predictions across different methods used in practice. Moreover, the predicted flutter mechanisms are also different. These significant discrepancies between the methods are mostly due to the difference in the prediction of the shock motion, which further demonstrates the importance of flow nonlinearities in transonic flutter analysis. The proposed methodology accurately captures

the dynamics of nonlinear shocks and leads to flutter results that are consistent with time-accurate FSI simulations.

For flutter analysis methods relying on a nonlinear aerodynamic model, the flutter speed and mechanism depend on the static (or mean) deformation of the wing, which varies with the flow condition. A limitation of the accepted industrial practice is that the analysis is performed around an assumed wing shape. Therefore, if the predicted flutter point is far from the design conditions, the static deformation of the wing can be large, especially for flexible composite wings. Additional flutter calculations must thus be performed considering the deformed shape of the wing, which increases the computational cost. A direction for future research may be to study in depth the influence of the static deformation of the wing on the aerodynamic nonlinearities in order to develop a more efficient way to consider its effects in a flutter analysis. In any case, if the flutter point is far from the design flight condition, it is not crucial to obtain it with better accuracy. The important issue is to show that the design condition is flutter-free.

The DMI-based aeroelastic methodology is accurate while being computationally tractable. The computational cost depends on the number of structural modes retained in the analysis and the number of reference forcing frequencies. For the flutter analysis of the wing structures considered in this thesis, a limited number of structural modes and frequencies were sufficient to obtain a level of precision similar to that of the time-accurate FSI simulations while being faster. In addition, the methodology does not require a coupling between a fluid solver and a solid solver because the motion is imposed in the unsteady simulations. The fully established periodic state is reached in a few oscillation cycles for the considered applications. It should also be noted that the most relevant dynamic modes can also be directly obtained from harmonic balance simulations, instead of applying DMD to unsteady simulations, which could in many cases further reduce the computational cost.

Overall, the novel methodology represents a promising approach for accurate but still fast flutter calculations, even in the transonic flow regime.

6.2 Future work

Our methodology for transonic flutter calculations does not assume anything about the origin of the input flow data and could rely, for instance, on the full potential model to provide flutter predictions at a lower cost than the higher fidelity Euler model while still capturing the moving shock waves with better accuracy than the lower fidelity transonic small disturbance (TSD) and time-linearized TSD models. The use of our methodology based on the full potential model is proposed as future work.

Other types of nonlinearities can affect the aeroelastic behavior of an aircraft wing and could be predicted using our methodology. Two potential research topics that are interesting from an aerodynamic modeling point of view are presented in the following. The last section shows some preliminary results of an approach based on few steady simulations to approximate an unsteady transonic flow.

6.2.1 Transonic buzz

The complexity of the configurations can be increased by including for example control surfaces. In that case, an important type of flutter that involves aerodynamic nonlinearities known as transonic buzz can occur. As illustrated in Figure 6.1, an oscillating control surface can induce the oscillations of a shock wave producing an oscillating pressure field which can in turn cause the oscillations of the control surface and so on. The proposed methodology could be used to take into account such interactions between control surfaces and shock waves in a flutter analysis. One of the challenges would be the generation and deformation of the grid for this type of flow problem involving several moving surfaces.

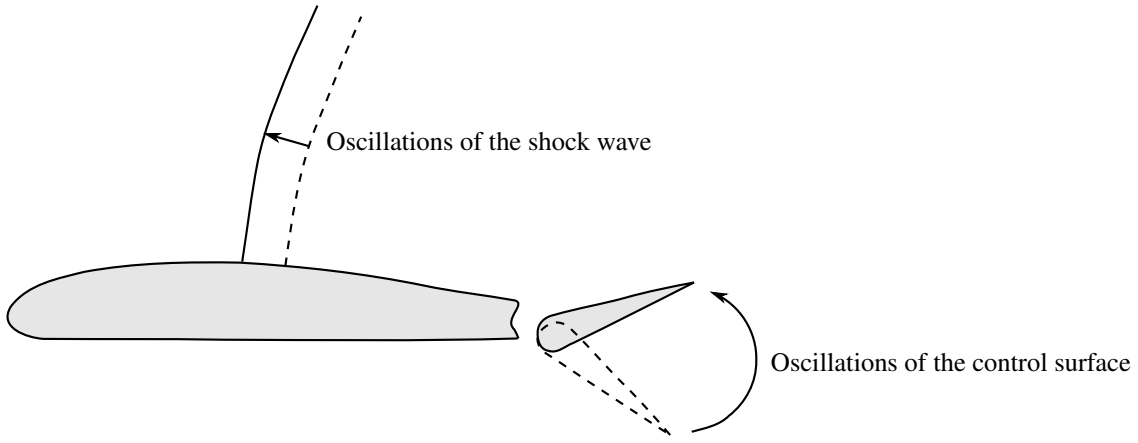

Figure 6.1: Illustration of the transonic buzz for an airfoil with a flap. (Adapted from Dowell et al. [46].)

6.2.2 Separated flows

As already mentioned, the methodology presented in this thesis assumes nothing about the origin of the input flow data and could allow the introduction of even higher fidelity CFD approaches for flutter calculations involving massively separated flows, as in the case of a wing at high angles of attack. The primary focus of this thesis was to analyze the aeroelastic stability of aircraft wings near cruise conditions. Therefore, the considered mean angles of attack were too small for massive flow separation to occur. The effect of a large mean angle of attack on the flutter boundary could be studied. For example, Figure 6.2 shows the average lift and drag coefficients of a NACA 0012 airfoil over a wide range of angles of attack. The lift coefficient increases linearly with the angle of attack until the stall where the flow separates from the upper surface of the airfoil at a high angle of attack and the lift drops significantly.

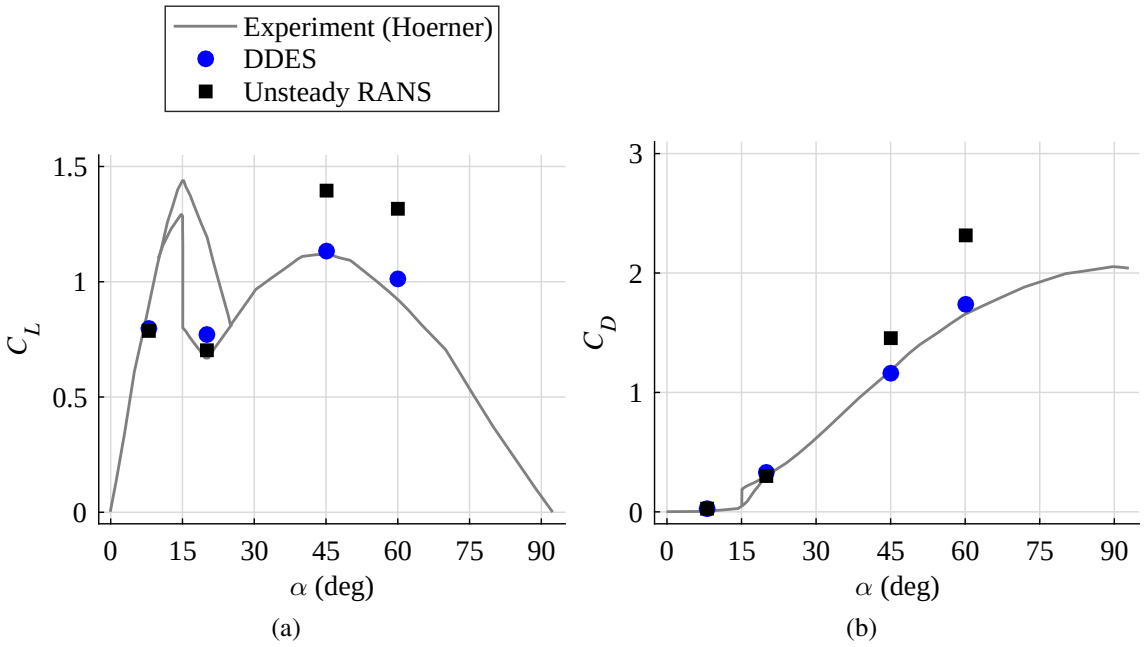

Figure 6.2: Average lift and drag coefficients of a NACA 0012 airfoil as a function of the angle of attack at a Reynolds number based on the chord length $Re = 10^5$ obtained by unsteady RANS simulations and delayed detached-eddy simulations (DDES) both based on the Spalart-Allmaras turbulence model [108, 109].

The aerodynamic modeling of massive flow separation is challenging. Unsteady RANS simulations largely suppress the three-dimensionality of massively separated flows over an airfoil at a high angle of attack as shown in Figure 6.3a. Grid refinement does not make it possible to capture smaller scales of the flow. The lift and drag predicted by the RANS model are generally overestimated beyond stall compared to experimental measurements (see Figure 6.2).

A detached-eddy simulation (DES) is a hybrid simulation strategy that combines a RANS and a large-eddy simulation (LES) model. The RANS mode of the DES approach operates in the boundary layers, where the turbulence model works satisfactorily, in order to reduce the computational cost as the use of LES to accurately capture thin boundary layers is expensive. The LES mode operates in regions where the flow is separated in order to capture the large flow scales which are configuration-dependent and anisotropic. Figure 6.3b shows that DES captures the 3D eddies of the massively separated flow. The DES aerodynamic coefficients are in good agreement with experimental measurements beyond stall.

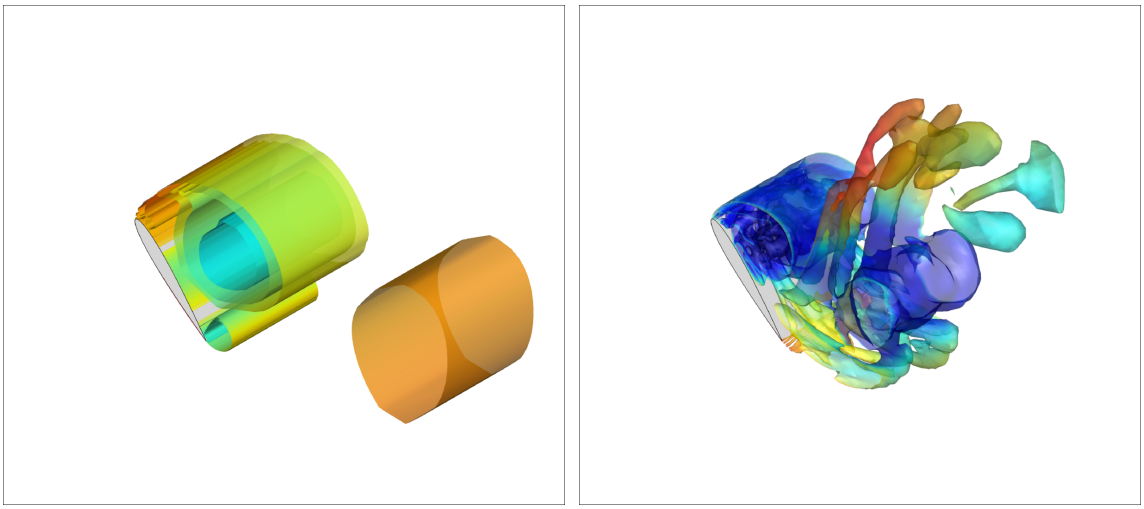

(a) (b)

Figure 6.3: Vorticity isosurfaces for the flow past a NACA 0012 airfoil at an angle of attack $\alpha = 60^\circ$ and a Reynolds number based on the chord length $Re = 10^5$ obtained by (a) an unsteady RANS simulation using the Spalart-Allmaras (S-A) turbulence model and (b) a detached-eddy simulation (DES) using the S-A turbulence model [108, 109].

The DMI method could be based on DES simulations in order to study the impact of massive flow separation on the aeroelastic behavior of a structure. This type of aerodynamic nonlinearity is of great importance for compressor, turbine and helicopter blades because they operate over a large range of angles of attack. In the case of massively separated flows, higher order flow modes may have a significant contribution to the flow dynamics. One of the challenges may therefore be to extend the flutter solution methods (e.g., the *p-k* method) to include higher order flow modes.

6.2.3 Applying a filter to steady solutions

Another potential research subject is to approximate an unsteady transonic flow by relying on few steady high-fidelity simulations in order to further reduce the computational cost associated with a transonic flutter calculation. This section focuses on using two steady Euler simulations and applying a filter to estimate the unsteady transonic flow around the pitching NACA 64A010 airfoil presented in Section 3.2. First, the approach is demonstrated on the evolution of the Mach field. Then, the shock motion is considered as a quantitative comparison to the unsteady Euler solutions for a large range of reduced frequencies.

Mach field

The first row of Figure 6.4 represents the evolution of the Mach field computed by an unsteady Euler simulation for the reference case at the reduced frequency $k = 0.202$. The shock waves are located at the edge of the supersonic regions and their position clearly varies over time.

The second row of Figure 6.4 represents snapshots at the same phases obtained by a quasi-steady approximation. In particular, two steady Euler simulations are used to determine the Mach field at the mean angle of attack $\bar{\alpha}$ and the derivative of this field with respect to the angle of attack α. In the context of this quasi-steady approximation, the evolution of the Mach field can be expressed as

$$M_{qs}(x,y,\tau) = M(x,y,\alpha=\bar{\alpha}) + \frac{\partial M(x,y,\alpha=\bar{\alpha})}{\partial \alpha}\left(\alpha(\tau)-\alpha_m\right). \tag{6.1}$$

In this case, the two steady simulations have been performed at the mean angle of attack ($\bar{\alpha} = 0^\circ$) and at the maximum pitching amplitude ($\hat{\alpha} = 1.01^\circ$). At $k\tau = 0^\circ (\alpha = 0^\circ)$, it can be seen that the lower and upper parts of the Mach field are not symmetrical for the unsteady case while the steady simulation at this angle of attack provides a symmetrical solution, which is expected from the symmetry of the airfoil. At $k\tau = 120^\circ$ ($\alpha \approx 0.87^\circ$), the quasi-steady calculation overestimates the extent of the supersonic region on the upper part and underestimates it on the lower part.

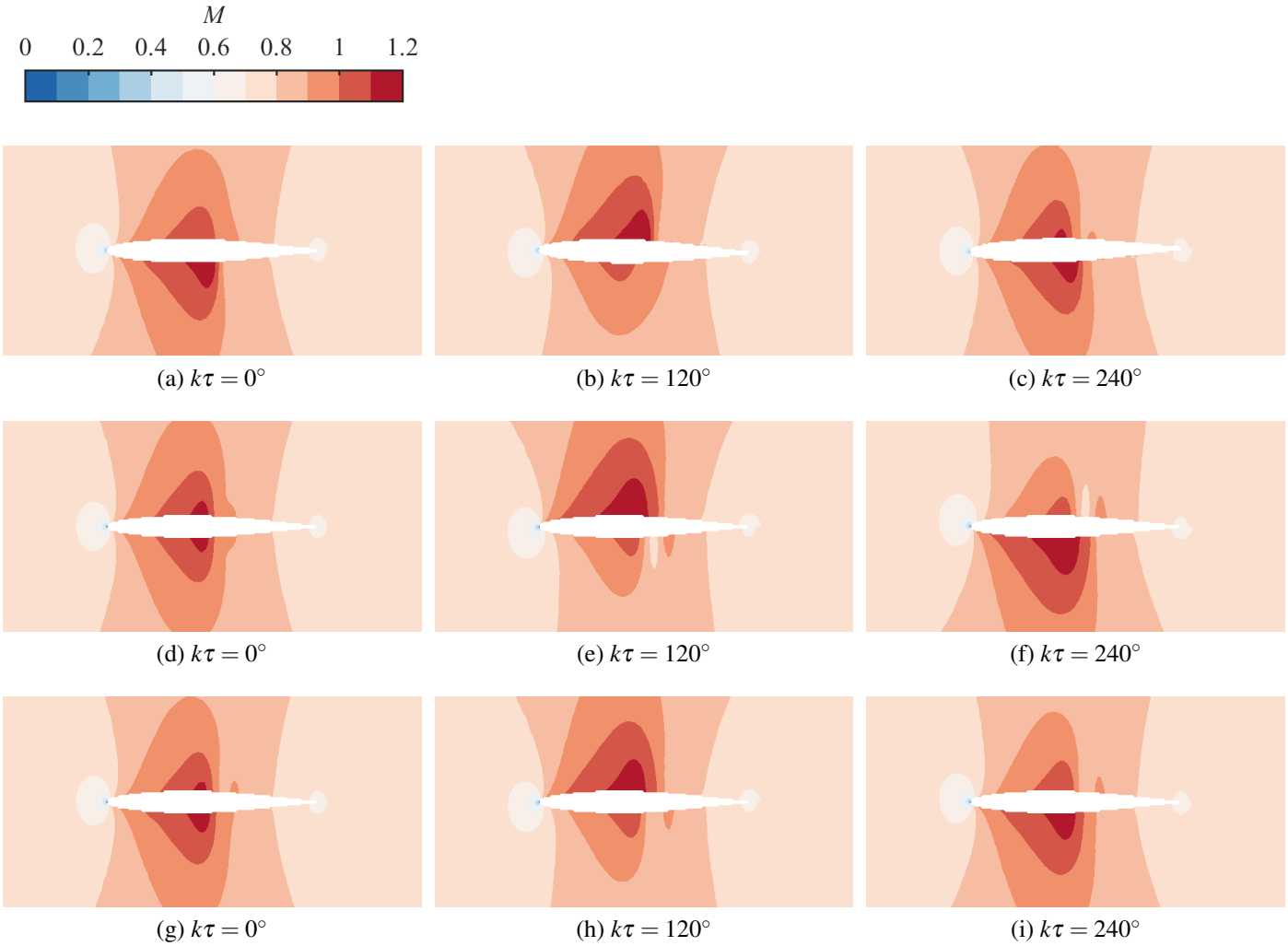

(a) $k\tau = 0°$ (b) $k\tau = 120°$ (c) $k\tau = 240°$

(d) $k\tau = 0°$ (e) $k\tau = 120°$ (f) $k\tau = 240°$

(g) $k\tau = 0°$ (h) $k\tau = 120°$ (i) $k\tau = 240°$

Figure 6.4: Contours of the Mach number M at different phases $k\tau$ of the forced oscillation cycle obtained by (a–c) an unsteady Euler simulation, (d–f) using steady Euler solutions and (g-i) applying Theodorsen's filter to steady Euler solutions for the reference pitching NACA 64A010 case at the reduced frequency $k = 0.202$ [18].

A quasi-steady approach is tempting because of its low computational cost and its independence with respect to the reduced frequency but the resulting unsteady Mach field and therefore the moving shock waves are inaccurate. More representative results can be obtained by applying an unsteady filter to Equation (6.1). A simple example is shown here using Theodorsen's function $C(k)$ [2], which can be seen as an analog filter since its amplitude decreases with k tending to 0.5 as k tends to infinity as shown in Figure 6.5. Applying Theodorsen's filter corrected for compressibility to Equation (6.1) gives

$$M_f(x,y,\tau) = M(x,y,\alpha = \bar{\alpha}) + \frac{\partial M(x,y,\alpha = \bar{\alpha})}{\partial \alpha} \Im(C(\bar{k})\hat{\alpha} e^{ik\tau}), \tag{6.2}$$

where $\bar{k} = k/\beta$ and $\beta = \sqrt{1 - M_\infty^2}$.

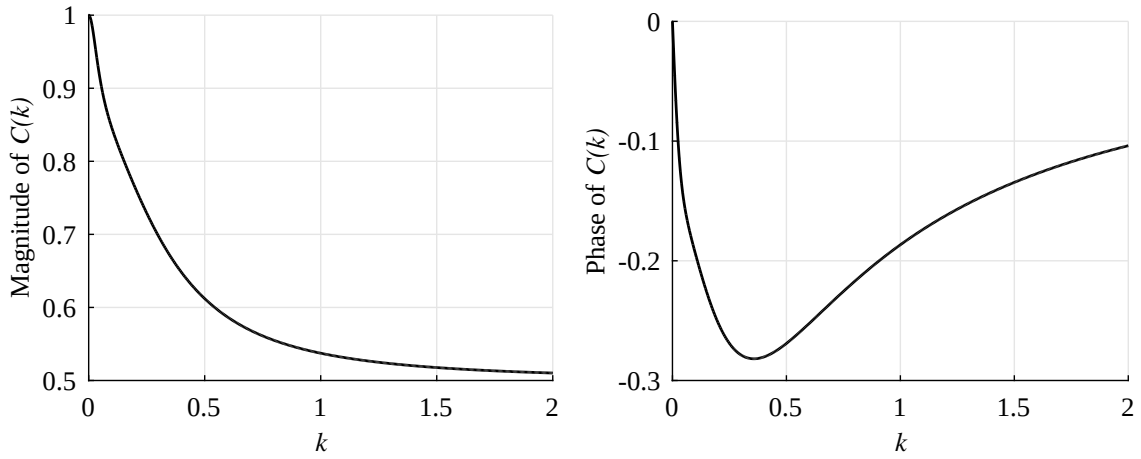

Figure 6.5: (a) Magnitude and (b) phase angle of Theodorsen's function as a function of the reduced frequency [18].

The third row of Figure 6.4 shows the results obtained by the filtered quasi-steady technique. At $k\tau = 0°$, the filter introduces an asymmetry in the Mach field compared to the steady case, which is qualitatively closer to the unsteady case. At $k\tau = 120°$, the filter reduces the supersonic region on the upper part obtained by the steady case and provides a better approximation to the unsteady case. Nonetheless, discrepancies with the unsteady Euler solution are still present.

Shock motion

The locally supersonic flow ($M > 1$) around the airfoil is decelerated to subsonic ($M < 1$) through a shock wave. The position of the shock waves can thus be directly extracted from the Mach field for an inviscid flow. Figure 6.6 repeats the analysis performed for the reference case to different values of the reduced frequency. It shows that the filtered quasi-steady approach provides acceptable results when k is below 0.4, which is promising knowing that the reduced frequency at flutter is typically of the order of 0.1 for most transonic flutter problems encountered in aircraft wings or control surfaces [6]. For higher frequencies, the shock motion computed by the unsteady Euler simulation becomes more irregular and this behavior cannot be fully recovered by applying the filter to steady simulations. When k is very large ($k = 2$), the shock motion is negligible.

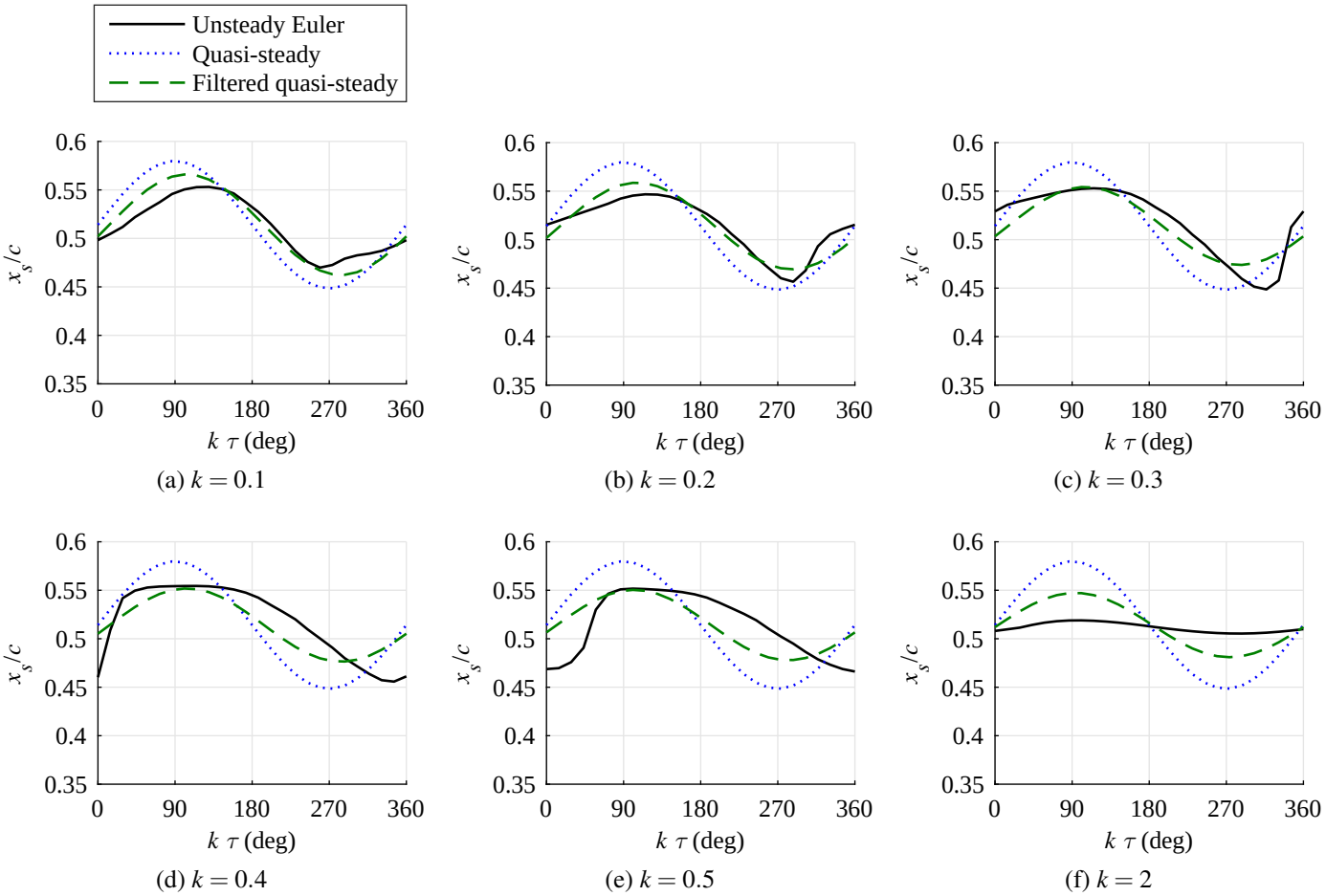

(a) $k = 0.1$ (b) $k = 0.2$ (c) $k = 0.3$

(d) $k = 0.4$ (e) $k = 0.5$ (f) $k = 2$

Figure 6.6: Comparison of the chordwise position of the shock on the upper surface x_s obtained by an unsteady Euler simulation, using steady Euler solutions and applying the Theodorsen's filter to steady Euler solutions for the pitching NACA 64A010 case at different values of the reduced frequency k.

The application of an unsteady filter to a limited number of steady Euler solutions provides a first approximation of the transonic flow around a pitching airfoil. An advantage of relying on steady simulations is their independence with respect to frequency. Nevertheless, the shock motion becomes increasingly nonlinear as the frequency of the pitching airfoil increases, and this nonlinear dynamics cannot be accurately computed by applying the Theodorsen filter. One research direction could be to develop an improved filter.

In the case of a flutter analysis of a 3D wing, one could imagine to perform a few steady Euler or RANS simulations for each structural mode shape at different deformation amplitudes. A potential approach may be to calibrate an unsteady filter using time-accurate simulations for one structural mode. The resulting filter may then be applied to the steady solutions obtained for the other structural modes in order to estimate the corresponding flow response as a function of frequency. On the other hand, instead of using

this approach as a stand-alone method, it could be combined with a linear panel method so as to extend the range of applicability of the latter to transonic flows with moving shock waves.

6.2.4 Other application

The methodology could also be applied to cases other than flutter calculations. For example, the methodology could be used in the field of flight dynamics to compute dynamic aerodynamic derivatives, which characterize the influence of the aircraft motion rates on the aerodynamic forces and moments. These dynamic derivatives affect the aerodynamic damping of the aircraft response and are essential for evaluating aircraft dynamic modes encountered in flight dynamics such as the short period oscillation and phugoid modes.

Final word

The DMI methodology represents an interesting unsteady aerodynamic model for transonic flutter calculations. It can rely on the Euler or RANS approach to achieve better accuracy than the industrial standards at a lower cost than time-accurate FSI simulations. The level of fidelity can also be adapted to the available computing power. This approach thereby opens new avenues for research.

Appendix A

Time-accurate FSI simulations of the AGARD 445.6 wing

The in-house modal solver has been validated by considering the AGARD 445.6 wing presented in Section 4.3. For example, Figure A.1 shows the results obtained by time-accurate FSI simulations at $M_\infty = 0.678$. Such simulations cannot directly give the exact flutter condition, they can only indicate that flutter occurs between two flight conditions at which the simulations have been carried out, one where the response amplitude decays and one where it diverges. Hence, the predicted flutter speed index lies between 0.41 and 0.42 at $M_\infty = 0.678$. This result is consistent with the value of the speed index found in Figure 4.20 ($U_{\text{index}} = 0.4174$). It is important to note that the AGARD wing oscillates around an equilibrium shape that is exactly the undeformed shape for any airspeed since this wing is symmetric and at zero angle of attack. The static deformation is null for this aeroelastic system.

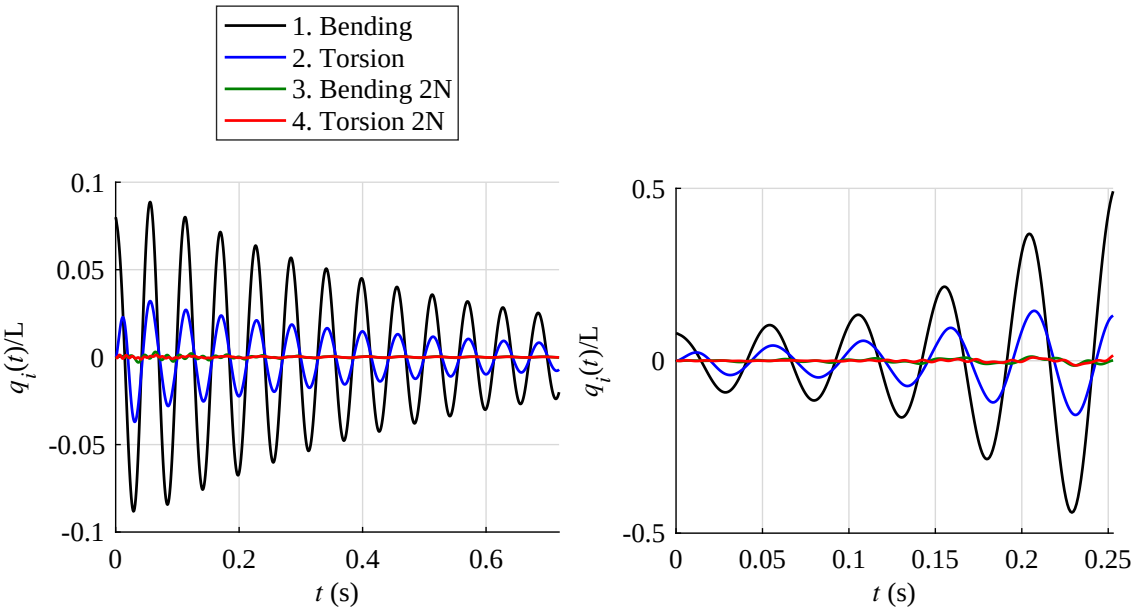

(a) $U_{\text{index}} = 0.41$ (b) $U_{\text{index}} = 0.42$

Figure A.1: Aeroelastic responses of the AGARD wing for two speed indices at a free-stream Mach number $M_\infty = 0.678$ obtained by solving the modal aeroelastic equations of motion based on the Euler model. The initial conditions are $\mathbf{q}(0) = [8\%L, 0, 0, 0, 0, 0]^\intercal$ and $\dot{\mathbf{q}}(0) = \mathbf{0}$.

Bibliography

[1] R. L. Bisplinghoff, H. Ashley, and R. L. Halfman. *Aeroelasticity*. Courier Corporation, 2013.

[2] Y. C. Fung. *An introduction to the theory of aeroelasticity*. Courier Dover Publications, 2008.

[3] J. R. Wright and J. E. Cooper. *Introduction to aircraft aeroelasticity and loads*, volume 20. John Wiley & Sons, 2008.

[4] M. P. Paidoussis. *Fluid-structure interactions: slender structures and axial flow*, volume 1. Academic press, 1998.

[5] J. D. Anderson Jr. *Fundamentals of aerodynamics*. Tata McGraw-Hill Education, 2010.

[6] O. O. Bendiksen. Review of unsteady transonic aerodynamics: theory and applications. *Progress in Aerospace Sciences*, 47(2):135–167, 2011.

[7] J. D. Anderson. *Modern compressible flow: with historical perspective*, volume 12. McGraw-Hill New York, 1990.

[8] J. D. Cole and L. P. Cook. *Transonic aerodynamics*, volume 30. Elsevier, 2012.

[9] N. F. Giannelis, G. A. Vio, and O. Levinski. A review of recent developments in the understanding of transonic shock buffet. *Progress in Aerospace Sciences*, 92:39–84, 2017.

[10] G. A. Vio, G. Dimitriadis, J. E. Cooper, K. J. Badcock, M. A. Woodgate, and A. M. Rampurawala. Aeroelastic system identification using transonic CFD data for a wing/store configuration. *Aerospace Science and Technology*, 11(2):146–154, 2007.

[11] J. P. Thomas, E. H. Dowell, and K. C. Hall. Nonlinear inviscid aerodynamic effects on transonic divergence, flutter, and limit-cycle oscillations. *AIAA journal*, 40(4):638–646, 2002.

[12] E. Albano and W. P. Rodden. A doublet-lattice method for calculating lift distributions on oscillating surfaces in subsonic flows. *AIAA Journal*, 7(2):279–285, 1969.

[13] W. P. Rodden, P. F. Taylor, and S. C. McIntosh. Further refinement of the subsonic doublet-lattice method. *Journal of Aircraft*, 35(5):720–727, 1998.

[14] C. Hirsch. *Numerical computation of internal and external flows: The fundamentals of computational fluid dynamics*. Elsevier, 2007.

[15] J. H. Ferziger and M. Perić. *Computational methods for fluid dynamics*, volume 3. Springer, 2002.

[16] J. D. Anderson and J. Wendt. *Computational fluid dynamics*, volume 206. Springer, 1995.

[17] R. G. A. Silva, O. A. F. Mello, J. L. F. Azevedo, P. Chen, and D. Liu. Investigation on transonic correction methods for unsteady aerodynamics and aeroelastic analyses. *Journal of Aircraft*, 45(6):1890–1903, 2008.

[18] H. Güner, G. Dimitriadis, and V. Terrapon. Research on fast aeroelastic modeling methods for the transonic regime. In *Proceedings of the International Forum on Aeroelasticity and Structural Dynamics, IFASD 2017*, pages Paper–IFASD, 2017.

[19] H. Güner, G. Dimitriadis, and V. Terrapon. Inviscid and viscous flow modeling for fast transonic flutter calculations. *Proceedings of the International Council of Aeronautical Sciences, ICAS 2018*, 2018.

[20] H. Güner, D. Thomas, G. Dimitriadis, and V. Terrapon. Unsteady aerodynamic modeling methodology based on dynamic mode interpolation for transonic flutter calculations. *Journal of Fluids and Structures*, 84:218–232, 2019.

[21] B. A. Nishida. *Fully simultaneous coupling of the full potential equation and the integral boundary layer equations in three dimensions*. PhD thesis, Massachusetts Institute of Technology, 1996.

[22] W. VAN DALSEM and J. STEGER. Finite-difference simulation of transonic separated flow using a full potential boundary layer interaction approach. In *16th Fluid and Plasmadynamics Conference*, page 1689, 1983.

[23] P. Chen. *ZAERO Theoretical Manual*. ZONA Technology Inc., 8.5 edition, 2008.

[24] R. Voss. Calculation of 3-d unsteady transonic potential flows by a field panel method. In *International Symposium on Aeroelasticity and Structural Dynamics, 2 nd, Aachen, West Germany*, pages 33–46, 1985.

[25] P.-C. Chen, X. Gao, and L. Tang. Overset field-panel method for unsteady transonic aerodynamic influence coefficient matrix generation. *AIAA journal*, 42(9):1775–1787, 2004.

[26] P. Chen and S. Bhasin. Zona6 versus the doublet-lattice method for unsteady aerodynamics on lifting surfaces. *Journal of Aircraft*, 49(3):966–968, 2012.

[27] M. Blair. A compilation of the mathematics leading to the doublet lattice method. Technical report, WRIGHT LAB WRIGHT-PATTERSON AFB OH, 1992.

[28] R. Palacios, H. Climent, A. Karlsson, and B. Winzell. Assessment of strategies for correcting linear unsteady aerodynamics using cfd or experimental results. In *Proceedings of the International Forum on Aeroelasticity and Structural Dynamics, IFASD 2001*, 2001.

[29] R. Silva. A study on correction methods for aeroelastic analysis in transonic flow. *Doctorate Dissertation, Aeronautics Dept., Technological Institute of Aeronautics (ITA), São José dos Campos, Brazil*, 2004.

[30] J. Brink-Spalink and J. Bruns. Correction of unsteady aerodynamic influence coefficients using experimental or cfd data. In *41st Structures, Structural Dynamics, and Materials Conference and Exhibit*, page 1489, 2000.

[31] D. Pitt and C. Goodman. Flutter calculations using doublet lattice aerodynamics modified by the full potential equations. In *28th Structures, Structural Dynamics and Materials Conference*, page 882, 1987.

[32] R. Zwaan. Verification of calculation methods for unsteady airloads in the prediction of transonic flutter. *Journal of Aircraft*, 22(10):833–839, 1985.

[33] M. Baker, K.-A. Yuan, and P. Goggin. Calculation of corrections to linear aerodynamic methods for static and dynamic analysis and design. In *39th AIAA/ASME/ASCE/AHS/ASC Structures, Structural Dynamics, and Materials Conference and Exhibit*, page 2072, 1998.

[34] I. Jadic, D. Hartley, and J. Giri. An enhanced correction factor technique for aerodynamic influence coefficient methods. In *MSC Aerospace User's Conference*. Citeseer, 1999.

[35] M. L. Baker. Cfd based corrections for linear aerodynamic methods. *AGARD Report*, 822, 1998.

[36] K. Yonemoto. Practical method for predicting transonic wing flutter phenomena. In *Congress of the International Council of the Aeronautical Sciences*, pages 724–732, 1984.

[37] K. Dau. A semi-empirical method for calculating pressures on oscillating wings in unsteady transonic flow. *Deutsche Airbus, Rept. DA-EF24-B08/92, Bremen, Germany*, 1992.

[38] H. Garner. A practical framework ior the evaluation of oscillatory aerodyna4ic loading on wings in supercritical flow. *Unsteady Airloads in Separated and Transonic Flow2*, 1977.

[39] P. Chen, D. Sarhaddi, and D. Liu. Transonic-aerodynamic-influence-coefficient approach for aeroelastic and mdo applications. *Journal of Aircraft*, 37(1):85–94, 2000.

[40] D. Liu, Y. Kao, and K. Fung. An efficient method for computing unsteady transonic aerodynamics ofswept wings with control surfaces. *Journal of Aircraft*, 25(1):25–31, 1988.

[41] E. Suciu, J. Glaser, and R. Coll. Aerodynamic derivatives factoring scheme for the msc/nastran doublet lattice program. In *MSC/NASTRAN Worlds Users' Conference*, 1990.

[42] E. H. Dowell, K. C. Hall, and M. C. Romanowski. Eigenmode analysis in unsteady aerodynamics: Reduced order models. *Applied Mechanics Reviews*, 50(6):371–386, 1997.

[43] D. J. Lucia, P. S. Beran, and W. A. Silva. Reduced-order modeling: new approaches for computational physics. *Progress in Aerospace Sciences*, 40(1-2):51–117, 2004.

[44] W. A. Silva and R. E. Bartels. Development of reduced-order models for aeroelastic analysis and flutter prediction using the CFL3Dv6.0 code. *Journal of Fluids and Structures*, 19(6):729–745, 2004.

[45] T. Kim, M. Hong, K. G. Bhatia, and G. SenGupta. Aeroelastic model reduction for affordable computational fluid dynamics-based flutter analysis. *AIAA Journal*, 43(12):2487–2495, 2005.

[46] E. H. Dowell, H. C. Curtiss, R. H. Scanlan, and F. Sisto. *A modern course in aeroelasticity*. Springer, 5 edition, 2015.

[47] Y. Liang, H. Lee, S. Lim, W. Lin, K. Lee, and C. Wu. Proper orthogonal decomposition and its applications—part i: Theory. *Journal of Sound and vibration*, 252(3):527–544, 2002.

[48] K. C. Hall, J. P. Thomas, and E. H. Dowell. Proper orthogonal decomposition technique for transonic unsteady aerodynamic flows. *AIAA Journal*, 38(10):1853–1862, 2000.

[49] J. P. Thomas, E. H. Dowell, and K. C. Hall. Three-dimensional transonic aeroelasticity using proper orthogonal decomposition-based reduced-order models. *Journal of Aircraft*, 40(3):544–551, 2003.

[50] T. Lieu and M. Lesoinne. Parameter adaptation of reduced order models for three-dimensional flutter analysis. In *42nd AIAA Aerospace Sciences Meeting and Exhibit*, page 888, 2004.

[51] J. P. Thomas, E. H. Dowell, and K. C. Hall. Static/dynamic correction approach for reduced-order modeling of unsteady aerodynamics. *Journal of Aircraft*, 43(4):865–878, 2006.

[52] D. Amsallem and C. Farhat. Interpolation method for adapting reduced-order models and application to aeroelasticity. *AIAA Journal*, 46(7):1803–1813, 2008.

[53] P. Hu, M. Bodson, and M. Brenner. Towards real-time simulation of aeroservoelastic dynamics for a flight vehicle from subsonic to hypersonic regime. In *AIAA Atmospheric Flight Mechanics Conference and Exhibit*, page 6375, 2008.

[54] W. P. Rodden and E. D. Bellinger. Aerodynamic lag functions, divergence, and the british flutter method. *Journal of Aircraft*, 19(7):596–598, 1982.

[55] F. Palacios, M. R. Colonno, A. C. Aranake, A. Campos, S. R. Copeland, T. D. Economon, A. K. Lonkar, T. W. Lukaczyk, T. W. Taylor, and J. J. Alonso. Stanford University Unstructured (SU2): An open-source integrated computational environment for multi-physics simulation and design. *AIAA Paper*, 287 (2013), 2013.

[56] F. Palacios, T. D. Economon, A. C. Aranake, S. R. Copeland, A. K. Lonkar, T. W. Lukaczyk, D. E. Manosalvas, K. R. Naik, A. S. Padrón, B. Tracey, et al. Stanford University Unstructured (SU2): Open-source analysis and design technology for turbulent flows. *AIAA Paper*, 243:13–17, 2014.

[57] T. D. Economon, F. Palacios, S. R. Copeland, T. W. Lukaczyk, and J. J. Alonso. Su2: An open-source suite for multiphysics simulation and design. *AIAA Journal*, 54(3):828–846, 2015.

[58] R. Sanchez, H. Kline, D. Thomas, A. Variyar, M. Righi, T. D. Economon, J. J. Alonso, R. Palacios, G. Dimitriadis, and V. Terrapon. Assessment of the fluid-structure interaction capabilities for aeronautical applications of the open-source solver su2. In *Proceedings of the European Congress on Computational Methods in Applied Sciences and Engineering, ECCOMAS Congress 2016*, 2016.

[59] J. Donea, A. Huerta, J.-P. Ponthot, and A. Rodriguez-Ferran. Arbitrary lagrangian-eulerian methods, volume 1 of encyclopedia of computational mechanics, chapter 14. *John Wiley & Sons Ltd*, 3:1–25, 2004.

[60] D. C. Wilcox et al. *Turbulence modeling for CFD*, volume 2. DCW industries La Canada, CA, 1998.

[61] F. M. White and I. Corfield. *Viscous fluid flow*, volume 3. McGraw-Hill New York, 2006.

[62] P. Spalart and S. Allmaras. A one-equation turbulence model for aerodynamic flows. In *30th aerospace sciences meeting and exhibit*, page 439, 1992.

[63] F. R. Menter. Two-equation eddy-viscosity turbulence models for engineering applications. *AIAA journal*, 32(8):1598–1605, 1994.

[64] P. R. Spalart and C. L. Rumsey. Effective inflow conditions for turbulence models in aerodynamic calculations. *AIAA journal*, 45(10):2544–2553, 2007.

[65] A. Jameson, W. Schmidt, and E. Turkel. Numerical solution of the euler equations by finite volume methods using runge kutta time stepping schemes. In *14th fluid and plasma dynamics conference*, page 1259, 1981.

[66] A. Jameson. Time dependent calculations using multigrid, with applications to unsteady flows past airfoils and wings. In *10th Computational Fluid Dynamics Conference*, page 1596, 1991.

[67] P. J. Schmid. Dynamic mode decomposition of numerical and experimental data. *Journal of fluid mechanics*, 656:5–28, 2010.

[68] A. Guissart, T. Andrianne, G. Dimitriadis, and V. Terrapon. Using proper orthogonal decomposition and dynamic mode decomposition methods for comparing cfd results experimental measurements. In *Proceedings of the 15th International Forum on Aeroelasticity and Structural Dynamics, IFASD 2013*, 2013.

[69] M. R. Jovanović, P. J. Schmid, and J. W. Nichols. Sparsity-promoting dynamic mode decomposition. *Physics of Fluids*, 26(2):024103, 2014.

[70] A. Ruhe. Rational krylov sequence methods for eigenvalue computation. *Linear Algebra and its Applications*, 58:391–405, 1984.

[71] J. H. Tu, C. W. Rowley, D. M. Luchtenburg, S. L. Brunton, and J. N. Kutz. On dynamic mode decomposition: theory and applications. *arXiv preprint arXiv:1312.0041*, 2013.

[72] S. Nimmagadda, T. D. Economon, J. J. Alonso, and C. R. Ilario da Silva. Robust uniform time sampling approach for the harmonic balance method. In *46th AIAA Fluid Dynamics Conference*, page 3966, 2016.

[73] A. Rubino, M. Pini, P. Colonna, T. Albring, S. Nimmagadda, T. Economon, and J. Alonso. Adjoint-based fluid dynamic design optimization in quasi-periodic unsteady flow problems using a harmonic balance method. *Journal of Computational Physics*, 372:220–235, 2018.

[74] K. C. Hall, J. P. Thomas, and W. S. Clark. Computation of unsteady nonlinear flows in cascades using a harmonic balance technique. *AIAA Journal*, 40(5):879–886, 2002.

[75] A. Da Ronch, A. J. McCracken, K. J. Badcock, M. Widhalm, and M. Campobasso. Linear frequency domain and harmonic balance predictions of dynamic derivatives. *Journal of Aircraft*, 50(3):694–707, 2013.

[76] M. Widhalm, R. P. Dwight, R. Thormann, and A. Hübner. Efficient computation of dynamic stability data with a linearized frequency domain solver. In *European Conference on Computational Fluid Dynamics*, 2010.

[77] R. Thormann and M. Widhalm. Linear-frequency-domain predictions of dynamic-response data for viscous transonic flows. *AIAA journal*, 51(11):2540–2557, 2013.

[78] R. Dwight, J. Brezillon, and D. Vollmer. Efficient algorithms for solution of the adjoint compressible navier-stokes equations with applications. In *Proceedings of the ONERA-DLR aerospace symposium (ODAS), Toulouse*. Citeseer, 2006.

[79] S. S. Davis. NACA 64A010 (NASA Ames model) oscillatory pitching. *AGARD Report*, 702 (1982), 1982.

[80] C. Geuzaine and J.-F. Remacle. Gmsh: A 3-d finite element mesh generator with built-in pre-and post-processing facilities. *International journal for numerical methods in engineering*, 79(11):1309–1331, 2009.

[81] R. Allemang and D. Brown. A correlation coefficient for modal vector analysis. In *Proceedings of the 1st International Modal Analysis Conference*, pages 110–116, 1982.

[82] Metafor. A nonlinear finite element code. University of Liège. `http://metafor.ltas.ulg.ac.be/`. Accessed May 16, 2018.

[83] W. P. Rodden and E. H. Johnson. *MSC/NASTRAN aeroelastic analysis: user's guide; Version 68*. MacNeal-Schwendler Corporation, 1994.

[84] G. Dimitriadis. *Introduction to Nonlinear Aeroelasticity*. John Wiley & Sons, 1 edition, 2017.

[85] G. Dimitriadis, N. Giannelis, and G. Vio. A modal frequency-domain generalised force matrix for the unsteady Vortex Lattice method. *Journal of Fluids and Structures*, 76:216–228, 2018.

[86] F. Tisseur and K. Meerbergen. The quadratic eigenvalue problem. *SIAM review*, 43(2):235–286, 2001.

[87] P. Chen. Damping perturbation method for flutter solution: the g-method. *AIAA journal*, 38(9):1519–1524, 2000.

[88] W. P. Rodden, R. L. Harder, and E. D. Bellinger. *Aeroelastic addition to NASTRAN*, volume 3094. National Aeronautics and Space Administration, Scientific and Technical . . . , 1979.

[89] K. Isogai. On the transonic-dip mechanism of flutter of a sweptback wing. *AIAA Journal*, 17(7):793–795, 1979.

[90] K. Isogai. Transonic dip mechanism of flutter of a sweptback wing ii. *AIAA Journal*, 19(9):1240–1242, 1981.

[91] J. Alonso and A. Jameson. Fully-implicit time-marching aeroelastic solutions. In *32nd Aerospace Sciences Meeting and Exhibit*, page 56, 1994.

[92] S. Timme and K. Badcock. Transonic aeroelastic instability searches using sampling and aerodynamic model hierarchy. *AIAA Journal*, 49(6):1191–1201, 2011.

[93] S. Yang, Z. Zhang, F. Liu, S. Luo, H.-M. Tsai, and D. Schuster. Time-domain aeroelastic simulation by a coupled euler and integral boundary-layer method. In *22nd Applied Aerodynamics Conference and Exhibit*, page 5377, 2004.

[94] E. C. Yates, N. S. Land, and J. T. Foughner. *Measured and calculated subsonic and transonic flutter characteristics of a 45 sweptback wing planform in air and in Freon-12 in the Langley transonic dynamics tunnel*. National Aeronautics and Space Administration, 1963.

[95] D. Thomas, M. L. Cerquaglia, R. Boman, T. Economon, J. Alonso, G. Dimitriadis, and V. Terrapon. Cupydo-an integrated python environment for coupled fluid-structure simulations. *Advances in Engineering Software*, 128:69–85, 2019.

[96] X. Chen, G.-C. Zha, and M.-T. Yang. Numerical simulation of 3-D wing flutter with fully coupled fluid–structural interaction. *Computers & Fluids*, 36(5):856–867, 2007.

[97] L. Elizabeth M and B. John T. Calculation of AGARD wing 445.6 flutter using Navier-Stokes aerodynamics. *NASA Langley Technical Report Server (1993)*, 1993.

[98] F. Liu, J. Cai, Y. Zhu, H. Tsai, and A. F. Wong. Calculation of wing flutter by a coupled fluid-structure method. *Journal of Aircraft*, 38(2):334–342, 2001.

[99] G. H. Silva, A. P. do Prado, P. H. Cabral, R. De Breuker, and J. K. Dillinger. Tailoring of a composite regional jet wing using the slice and swap method. *Journal of Aircraft*, 56(3):990–1004, 2018.

[100] L. Cavagna, P. Masarati, and G. Quaranta. Coupled multibody/computational fluid dynamics simulation of maneuvering flexible aircraft. *Journal of aircraft*, 48(1):92–106, 2011.

[101] S. Chakravarthy, O. Peroomian, U. Goldberg, and S. Palaniswamy. The cfd++ computational fluid dynamics software suite. In *AIAA and SAE, 1998 World Aviation Conference*, page 5564, 1998.

[102] R. L. Harder and R. N. Desmarais. Interpolation using surface splines. *Journal of aircraft*, 9(2):189–191, 1972.

[103] W. H. Press, B. P. Flannery, S. A. Teukolsky, and W. T. Vetterling. Lu decomposition and its applications. *Numerical Recipes in FORTRAN: The Art of Scientific Computing*, pages 34–42, 1992.

[104] W. H. Press, S. A. Teukolsky, W. T. Vetterling, and B. P. Flannery. *Numerical recipes in Fortran 77: the art of scientific computing*, volume 2. Cambridge university press Cambridge, 1992.

[105] F. W. Leslie and C. G. Justus. The nasa marshall space flight center earth global reference atmospheric model-2010 version. *NASA Langley Technical Report Server*, 2011.

[106] M. L. Cerquaglia, D. Thomas, R. Boman, V. Terrapon, and J.-P. Ponthot. A fully partitioned lagrangian framework for fsi problems characterized by free surfaces, large solid deformations and displacements, and strong added-mass effects. *Computer Methods in Applied Mechanics and Engineering*, 348:409–442, 2019.

[107] J. Dormand and P. Prince. Runge-kutta triples. *Computers & Mathematics with Applications*, 12(9):1007–1017, 1986.

[108] M. Shur, P. Spalart, M. Strelets, and A. Travin. Detached-eddy simulation of an airfoil at high angle of attack. In *Engineering turbulence modelling and experiments 4*, pages 669–678. Elsevier, 1999.

[109] H. Güner. Delayed detached-eddy simulations for separated flows. Master's thesis, University of Liège, 2015.